©2012

Michael D. Tomasini

ALL RIGHTS RESERVED

INTERFACIAL INTERACTIONS OF NANOPARTICLES WITH SURFACTANTS AND POLYMERS: A COMPUTATIONAL APPROACH TO TARGET BIOMEDICAL AND PHARMACEUTICAL SYTEMS

by

MICHAEL D. TOMASINI

A Dissertation submitted to the

Graduate School-New Brunswick

Rutgers, The State University of New Jersey

in partial fulfillment of the requirements

for the degree of

Doctor of Philosophy

Graduate Program in Biomedical Engineering

and

The Graduate School of Biomedical Sciences

University of Medicine and Dentistry of New Jersey

written under the direction of

M. Silvina Tomassone

and approved by

____

____

____

____

New Brunswick, New Jersey

May 2012

ABSTRACT OF THE DISSERTATION

Interfacial Interactions of Nanoparticles with Surfactants and Polymers: A Computational Approach to Target Biomedical and Pharmaceutical Systems

By Michael D. Tomasini

Dissertation Director:

Professor M. Silvina Tomassone

Nanotechnology is an emerging field with the promise for new materials and applications, particularly in the medical field for diagnosis and treatment of disease. The high surface area to volume ratio of nanoparticles gives rise to useful material properties such as enhanced solubility and dissolution for drug nanoparticles as well as superparamagnetism in the case of magnetic nanoparticles. Often, nanoparticle interactions with surfactants and polymers arise in a variety of scenarios: the production and stabilization to reduce particle agglomeration, to aid in nanoparticle delivery to specific areas of the body, increase bioavailability by avoiding body clearance mechanisms, add desired functionality, and finally the biological targets of nanoparticles are often the surfactants (lipids of the cell membrane) or polymers (proteins) of the body. Understanding the interfacial interactions of nanoparticles with polymers or surfactants is therefore crucial in proceeding ahead with nanoparticles as viable options for medical treatments. In this dissertation, a series of computational techniques are employed to elucidate the interfacial interactions at the molecular level between surfactants, polymers, and nanoparticles in three different case studies. First, Molecular Dynamics and Dissipative Particle Dynamics simulation methods are used to study the stability of a model cell membrane to an applied stress in order to mimic the interactions that occur in magnetic fluid hyperthermia, a nanoparticle-based treatment for cancerous tumors. Here, the aim is to determine if magnetic nanoparticles are capable of generating mechanical forces sufficient to rupture a cell membrane. Secondly, coarse-grained Molecular Dynamics is utilized to explore the interaction of micelle-forming amphiphilic molecules interacting with the human scavenger receptor A for use in preventing uptake of oxidized low-density lipoproteins. Finally, Monte Carlo simulations are developed to study nanocrystal nucleation from solution in the presence of polymers to determine factors that act to promote or inhibit nucleation.

Acknowledgements

I would like to thank my advisor Prof. M. Silvina Tomassone for her helpful guidance and support throughout my time as her student. Her encouragement and assistance has been vital in making me believe that I could succeed on the difficult journey from a wide-eyed, new graduate student to a bona fide scientist. Along the path she was influential in broadening the scope of my studies, allowing and assisting me in learning a wide range of computational techniques and how to apply these techniques to a investigate phenomena in a diverse array of areas. I would also like to acknowledge the members of Prof. Tomassone's group for sharing their knowledge, expertise, assistance, critiques, and time during my stay in the group: Yangyang Shen was instrumental in aiding my beginnings as a new student learning computer simulation; Frank Romanski offered invaluable assessments of my work, always grounding it with experimental backing; and Wusheng Zhu provided a great deal of assistance in performing some of the molecular dynamics simulations that contributed greatly to this thesis. Additionally, I would like to acknowledge Fernando Muzzio for his wisdom and support and Aleksey Vishnyakov for his help in teaching me Monte Carlo and Dissipative Particle Dynamics Simulation without which this thesis would seem rather scant. Finally, I would like to thank a number of fellow graduate students who, be it through friendship, helpful discourse, or imparting experience have greatly impacted my experience here at Rutgers: Omar Haq, John Landers, Erhan Bilal, Eric Jayjock, Kurt Smith, and Jen Winkler.

Dedication

I dedicate this thesis to my parents Stephen and Deborah and by brother Richard for their love and support while I endeavored to earn my degree so far away from home. I would also like to dedicate this thesis to my girlfriend Kathleen with whom I was able to share the blessings and hardships of life as a graduate student.

Table of Contents

Abstract of the Dissertation ii

Acknowledgements iv

Dedication v

Table of Contents vi

List of Tables xi

List of Figures xii

Chapter 1 Introduction 1

1.1 Motivation 1

1.2 The Role of Polymer and Surfactant in Biomedical and Pharmaceutical Nanotechnology 3

1.2.1 Surfactants and Polymers in the Production and Stabilization of Nanoparticles 3

1.2.2 Surfactants and Polymers in Nanoparticle Functionality and Biocompatibility 7

1.2.3 Nanoparticle Interaction with Biological Molecules 9

1.3 Computational Nanotechnology 10

1.4 Dissertation Objectives and Organization 11

1.5 Methodology: Molecular Simulation Techniques 13

1.5.1 Molecular Dynamics Simulation 16

1.5.2 Monte Carlo Simulation 18

1.5.3 Coarse-Graining 20

Chapter 2 Energetics of Cell Membrane Rupture by Magnetic Nanoparticles in Magnetic Fluid Hyperthermia 21

2.1 Cancer Nanotechnology 22

2.2 Magnetic Fluid Hyperthermia 23

2.2.1 A Lipid Bilayer under Stress as a Model for Magnetic Fluid Hyperthermia 25

2.3 Molecular Dynamics Simulations of a Lipid Bilayer under Stress 27

2.3.1 Bilayer Rupture by Incremental Tension 30

2.3.2 Bilayer Rupture by Incremental Shearing 35

2.3.4 Comparison with Experimental Results 40

2.3.5 Energetics of Membrane Rupture 41

2.4 Poly(ethylene oxide) – Poly(ethyl ethylene) Block Copolymers for the Enhancement of Cell Membrane Rupture Under Stress 43

2.4.1 The Dissipative Particle Dynamics (DPD) Simulation Technique 45

2.4.2 System Parameterization 49

2.4.3 Simulation Details 51

2.4.4 System Validation 55

2.5 Effect of Polymer Concentration on Bilayer Rupture 59

2.5.1 Effect of Polymer Length on Bilayer Rupture 61

2.5.2 Effect of Polymer Hydrophilic to Hydrophobic Ratio 63

2.5.3 Effect of Polymer Block Structure on Bilayer Rupture 65

2.5.4 Energetics of Membrane Rupture and Comparison with Experiment 66

2.6 Conclusions of Simulation Studies of a Lipid Bilayer under Stress 68

Chapter 3 Engineered Macromolecules as Inhibitors to Oxidized Low Density Lipoprotein by Macrophage Scavenger Receptors: Simulation of Structure – Function Relationships...**71**

3.1 Pathology of Atherosclerosis 71

3.1.1 Structure of Scavenger Receptor A 72

3.1.2 Nanolipoblockers as Inhibitors of Oxidized Low Density Lipoprotein Uptake 73

3.2 Coarse-Grained Simulation of Nanolipoblocker Aggregates with Scavenger Receptor A... 74

3.2.1 System Details.. 74

3.3 Formation of Nanolipoblockers into Micelles 80

3.3.1 Interaction of Nanolipoblockers with Scavenger Receptor A................................. 84

3.3.2 Molecular Contacts between Nanolipoblockers and Scavenger Receptor A.......... 86

3.3.3 Interaction of Nanolipoblockers with the Binding Pocket of Scavenger Receptor A…………….. 91

3.3.4 Discussion of Contact Results.. 93

3.4 Conclusions of Coarse-Grained Simulation of Nanolipoblocker Interaction with Scavenger Receptor A.. 96

Chapter 4 Molecular Simulation of Nucleation of Pharmaceuticals in the Presence of Polymeric Additives ... 98

4.1 General Nucleation Theory ... 98

4.1.2 Nucleation from Solution in the Presence of Polymers ... 102

4.2 Simulation of Drug Nucleation in the Presence of Polymers – The Gauge-Cell Monte Carlo Technique ... 104

4.2.1 Generation of the Isotherm ... 106

4.2.2 Calculation of the Nucleation Barrier ... 107

4.3.1 Simulation Parameters ... 109

4.3.2 Computation of the Chemical Potential and Supersaturation ... 110

4.3.3 Model Systems for the Promotion and Inhibition of Drug Nucleation ... 112

4.3.3.1 Model System 1: Promotion ... 113

4.3.3.2 Model System 2: Inhibition ... 116

4.3.4 Nucleation of Felodipine in the Presence of PVP or HPMC ... 119

4.3.4.1 Molecular Dynamics Simulations for Parameter Estimation ... 121

4.3.4.2 Nucleation of Felodipine in the Presence of PVP ... 122

4.3.4.3 Nucleation of Felodipine in the Presence of HPMC ... 125

4.4 Conclusions of Pharmaceutical Nucleation in the Presence of Polymer ... 128

Chapter 5 Conclusions and Future Work ... 130

5.1 Energetics of Cell Membrane Rupture by Magnetic Nanoparticles in Magnetic Fluid Hyperthermia 131

5.2 Engineered Macromolecules as Inhibitors to Oxidized Low Density Lipoprotein by Macrophage Scavenger Receptors: Simulation of Structure – Function Relationships ……… 133

5.3 Pharmaceutical Nucleation in the Presence of Polymeric Additives 134

References **135**

Curriculum Vitae **146**

List of Tables

Table 1: Bead – Bead interactions for the DPD polymer – bilayer system 49

Table 2: Bonded interactions for the DPD polymer – bilayer system 51

Table 3: Bond angle interactions for the DPD polymer – bilayer system 51

Table 4: NLB Cluster analysis. 82

Table 5: Number of SR-A CG beads with persistent contacts.. 91

Table 6: Bead interaction parameters for nucleation model system 1 113

Table 7: Bead interaction parameters for nucleation model system 2 116

Table 8: Binding energy simulation results for felodipine – PVP – water. 123

Table 9: LJ coefficients for felodipine – PVP – water gauge-cell MC......................... 123

Table 10: Binding energy simulation results for felodipine – HPMC – water 126

Table 11: LJ coefficients for felodipine – HPMC – water gauge-cell MC................... 127

List of Figures

Figure 1: Schematic representation of the spring and parachute effect 6

Figure 2: Schematic drawing of a liposome 8

Figure 3: Schematic highlighting the various computational methods for simulating different length and time scales 15

Figure 4: DPPC lipid bilayer following energy minimization and equilibration 29

Figure 5: Running average of the surface tension following each bilayer stretch.......... 31

Figure 6: Surface tension vs. stretch area for a bilayer stretched in its principal directions.. 32

Figure 7: Snapshot of pore formation in the bilayer during incremental strain............. 33

Figure 8: Diffusion coefficient perpendicular to the bilayer surface as a function of normalized bilayer area for a bilayer under tension... 34

Figure 9: Surface tension as a function of time for each shear increment..................... 36

Figure 10: Surface tension vs. area for a bilayer subjected to incremental shearing...... 37

Figure 11: Snapshot of pore formation in the bilayer during incremental shearing....... 38

Figure 12: Diffusion coefficient perpendicular to the bilayer surface as a function of normalized bilayer area for a bilayer under shear... 39

Figure 13: Schematic showing the coarse-graining scheme of the lipid-polymer-water system 48

Figure 14: Schematic representation of the bilayer system 52

Figure 15: Surface tension of the bilayer versus area fit 54

Figure 16: Lipid head density across the bilayer 56

Figure 17: Distribution of PEO beads from the bilayer surface 58

Figure 18: Snapshots of membrane rupture with 20.6 wt.% polymer 60

Figure 19: The response of polymer concentration on bilayer rupture.......................... 60

Figure 20: The response of polymer length on bilayer rupture 62

Figure 21: The response polymer hydrophobic content on bilayer rupture................... 63

Figure 22: Rupture hydrophilic – hydrophobic comparison.. 64

Figure 23: Snapshot of the polymer system with 35% hydrophilic ratio 65

Figure 24: The response of polymer block structure on bilayer rupture 66

Figure 25: Rupture energies for the different bilayer-polymer systems........................ 68

Figure 26: Amino acid sequence of the collagen-like domain of SR-A 75

Figure 27: Chemical structure and corresponding CG representation of the four different NLBs simulated. 77

Figure 28: Snapshot of 1CP simulation following energy minimization and equilibration 80

Figure 29: Snapshot of the self-assembly process of 1CM NLB into micelles............. 82

Figure 30: Snapshot of PEG-COOH showing that it does not form micelles 83

Figure 31: Evolution of the cluster distribution for 1CM micelles............................... 83

Figure 32: Interaction following 800 ns of simulation of SR-A with each type of NLB 85

Figure 33: The number of contacts that NLBs form with SR-A 88

Figure 34: Contact map of interactions between NLBs and SR-A................................ 90

Figure 35: Average number of contacts within 0.8 nm and 2.0 nm 93

Figure 36: Free energy of cluster formation as a function of cluster size 100

Figure 37: Nucleation barrier in transitioning from molecules dispersed in solution to molecules in a crystalline lattice. 101

Figure 38: Schematic of the gauge-cell MC technique 105

Figure 39: Isotherm resulting for a series of gauge-cell MC simulations 107

Figure 40: Sample isotherm from a gauge-cell MC simulation and the method used to calculate the nucleation barrier 109

Figure 41: Simulation with a large drug crystal in solution with free drug 111

Figure 42: Simulation results for model system 1 115

Figure 43: Snapshots corresponding to model system 1 115

Figure 44: Simulation results for model system 2 118

Figure 45: Snapshots corresponding to mode system 2 118

Figure 46: MD simulations used to calculate the binary binding energies 120

Figure 47: Results of atomistic MD data for two sample component combinations.... 122

Figure 48: Simulation results of nucleation in a felodipine-PVP-water system 124

Figure 49: Snapshots of the felodipine – PVP – water system 125

Figure 50: Computed isotherm of the felodipine-HPMC-water system 128

Chapter 1 Introduction

1.1 Motivation

Nanotechnology can be defined as the formation or manipulation of molecules or particles having one dimension less than 100 nm (1); (2) but is often extended to include particles up to 500 nm in size when referencing nanoparticles (3); (4). At this length scale the physical phenomena of materials can differ greatly from their characteristics at the macroscopic level. As the size of a particle is decreased the percentage of atoms on the surface of the particle becomes significant. The surface area to volume ratio increases dramatically, increasing the surface energy of the particle. This can have pronounced effects on material properties such as solubility -normally insoluble materials become soluble at the nanoscale (5)- conductivity -high thermal conductivity of carbon nanotubes (6)- optical properties -particle size based fluorescence of quantum dots (7)- and magnetic properties -superparamagnetism of iron oxide nanoparticles (8)- to name a few. These emergent properties can be exploited biomedically to enhance diagnosis and treatment of disease. For example, quantum dots are often used as fluorescent labels of biological materials (9), and iron oxide nanoparticles are commonly used for contrast enhancement in MRI imaging (10). Carbon nanotubes have been investigated as substrates for neural tissue (11), and formulation of drugs into nanoparticles can result in higher efficacy at lower dosages (12) particularly beneficial with highly toxic drugs (13). These valuable properties of nanotechnology however, are accompanied by the added difficulty of nanoparticle production and stabilization stemming from the increased surface energy. As nanoparticles decrease in size there is a tendency for the particles to agglomerate, negating the benefits of fabricating the particles in the nano-sized regime.

In a pharmaceutical setting, to deal with this problem one often uses polymeric or surfactant additives to aid in stabilizing the high-energy surfaces of the nanoparticles to prevent agglomeration and add functionality (14); (15); (16). Surface stabilization arises through interfacial interactions either sterically when the additive surrounds the particle surface, or by imparting a layer of electrochemical stability to control surface charge and enhance electrostatic repulsion between particles. Having a comprehensive understanding of these interfacial interactions is paramount to fabricating multitude nanoparticles for the controlled treatment of disease.

Just as interfacial interactions between polymeric and surfactant additives are central in the production and stabilization of nanoparticles, they are also highly relevant in the biological interactions that occur between nanoparticles and the body. When administered, nanoparticles can interact with specific proteins (biological polymers) or lipids (biological surfactants) of cells in the body. The majority of these biointerfacial interactions occur on the nanoscale, and the specific molecular level interactions dictate biological response. Difficulty can arise when attempting to elucidate these interfacial interactions due to the small length and short time scales that are involved. Optical microscopy cannot easily resolve the level of detail of specific molecular interactions, and electron microscopy must be performed in a static, time-independent manner. As such, this is an area where computational modeling can be of great use. The length and time scales of nanotechnology are often such that they can be addressed through current capabilities of computer simulation. Additionally, the predictive nature of computational nanotechnology allows for characterization of an extensive array of systems more rapidly and cost-effectively than experimental techniques (17). It is for this reason that computer modeling has become a powerful tool for the prediction and understanding of interfacial interactions between nanoparticles, polymers, and surfactants (18); (19). The work of this thesis aims to explore interfacial interactions of nanoparticles with polymers and surfactants using molecular computation with the goal of uncovering the specific molecular interactions that underpin observed phenomena in three case studies of biomedical and pharmaceutical systems.

1.2 The Role of Polymer and Surfactant in Biomedical and Pharmaceutical Nanotechnology

Interfacial interactions of surfactants and polymers with nanoparticles permeate all areas of nanotechnology. For the purpose of this thesis, the processes that accompany a nanotechnology treatment can be broken down into three phases: nanoparticle production and stabilization, nanoparticle functionality and biocompatibility, and nanoparticle interactions with biological targets within the body. In each case, the underlying molecular interactions govern the resultant macroscopic phenomena. The roles played by surfactants and polymers will be expounded upon in each case.

1.2.1 Surfactants and Polymers in the Production and Stabilization of Nanoparticles

In recent years, many new drug candidates to target specific diseases have been discovered, but their success as viable treatments have been rather limited, largely due to their poor water-solubility (20). A technique that has been shown to increase solubility and bioavailability is to formulate drug candidates as nanoparticles because the high surface energy enhances drug solubility and dissolution (21); (22). The increased surface energy of nanoparticles however makes them highly prone to aggregation, hindering the benefits from nano-sizing the pharmaceutical. For this reason, the production of nanoparticles is generally accompanied by stabilizing agents in the form of polymers or surfactants. One method for the production of nanoparticles, termed the 'bottom-up' approach (23), involves crystallization of the drug particles from solution. In order to achieve a reliable concentration and uniform particle size for delivery it is important to have a good understanding and control over the crystallization process, an area with significant ambiguities (24). Polymers and surfactants can influence whether particle crystallization occurs and the rate by which it proceeds by influencing the nucleation process. Additives that strongly interact with a drug molecule in solution have been shown to delay the onset of crystallization, forming a transient supersaturated solution which can increase the driving force for drug uptake in the body (25); (26). Nanoparticles can be formulated as a metastable amorphous crystal in which there is an absence of long-range order that is normally present in crystals. These amorphous nanoparticles have a higher energy compared to more stable crystalline forms and therefore exhibit enhanced dissolution (27). When dissolved in solution, amorphous nanoparticles show a sharp increase in solution concentration enhancing bioavailability. However, this supersaturated solution is only transient and the particles can quickly precipitate out into more stable crystalline forms. To combat this, polymeric precipitation inhibitors can be added to the formulation to keep the drug in solution, termed the 'spring and parachute' effect. Figure 1 displays drug concentration as a function of time for different drug formulations. A macroscopic crystal in solution begins to dissolve until the equilibrium saturation concentration (C_{sat}) is reached (dashed line). An amorphous nanoparticle (dotted line) shows a transient spike in the concentration which quickly decays to C_{sat}. The solid line is an amorphous formulation in the presence of a polymeric precipitation inhibitor which slows precipitation of the drug from solution and prolongs the supersaturated state. Increased concentration of drug in solution increases the driving force for absorption and increases bioavailability. A caveat of this method is that it is not well understood how polymeric precipitation inhibitors interact with the drug to prevent crystallization from solution, making the selection of polymers for optimal precipitation inhibition for a given drug largely a trial-and-error endeavor.

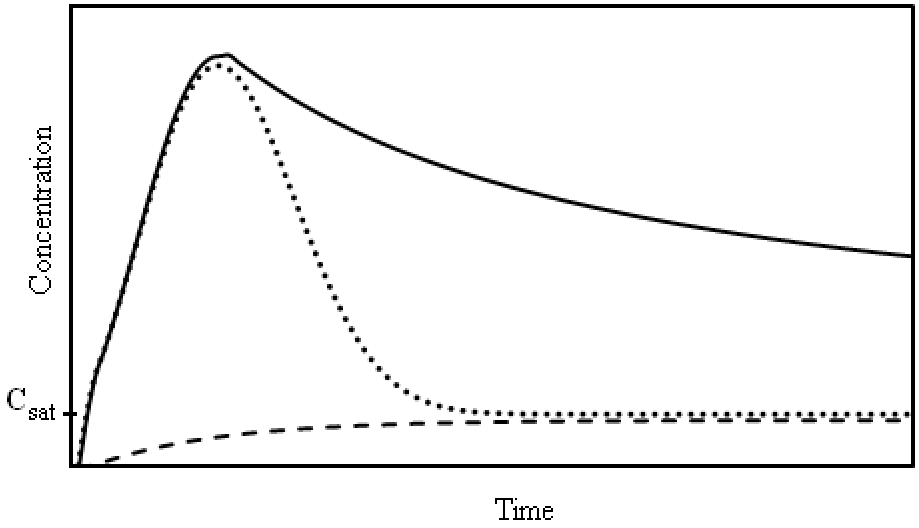

Figure 1: Schematic representation of the spring and parachute effect. The dashed line represents dissolution of a crystalline drug. The dotted line is the dissolution profile of an amorphous drug (spring). The solid line is the dissolution profile of an amorphous compound in the presence of a precipitation inhibitor (spring and parachute). C_{sat} is the saturated equilibrium solution concentration of the drug.

Conversely, polymers and surfactants are also able to provide a surface to aid heterogeneous nucleation (28); (29) or decrease the interfacial tension of growing drug clusters, facilitating precipitation from solution. Surfactants and polymers can furthermore play a role in the growth phase of crystallization, stabilizing free crystal surfaces preventing the growth of nanoparticles (30); (31), and providing control over the resultant nanoparticle crystal structure and size (32). For example, surfactants may preferentially adhere to a particular surface of a growing crystal, quenching the growth of that surface (33). This is useful for designing particles with specific crystal morphology such as plates or needles. A drawback of using polymers and surfactants to control nanoparticle nucleation and growth is that it is not known a priori what specific interfacial interactions the additive will have with the forming nanoparticle, making predicting the outcome difficult and the selection of optimal additives largely *ad hoc*.

1.2.2 Surfactants and Polymers in Nanoparticle Functionality and Biocompatibility

Nanoparticles for directed biomedical applications within the body are often associated with polymers or surfactants to enhance biocompatibility, aid in delivery, or perform a specific function. Circulating nanoparticles are subject to the reticuloendothelial system (RES) which acts to tag foreign particles for immediate phagocytosis by macrophages. As such, nanoparticle surfaces are frequently conjugated with polymers to imbue a stealth property to the particles and prevent opsonization. The biocompatible polymer polyethylene glycol (PEG) is most commonly used for this purpose because it is highly hydrophilic and has a significant amount of chain flexibility which prevents the attachment of serum proteins which has been shown to increase the circulation time (34).

In addition to conferring enhanced biocompatibility, surfactants and polymers are associated with nanoparticles to enhance targeting and delivery. A number of possible drug candidates fail because though effective, they cannot be successfully delivered to their desired target. A compound that is too hydrophobic does not show enough absorption for oral delivery and one that is too hydrophilic cannot cross the lipid membrane of cells. Lipinski et al. (35) developed a general rule of thumb, the Rule of

Five, which posits that an active compound is likely to have poor absorption or permeability if it either: has more than five hydrogen bond donors, more than ten hydrogen bond acceptors, a molecular weight greater than 500, or a logP (octanol-water partition coefficient) greater than 5. These criteria exclude many possible drug candidates and are an area where nanotechnology can be of use. Liposomes are surfactant-based, nano-sized carrier vesicles consisting of an aqueous core surrounded by one or more lipid bilayers. Figure 2 shows a simple schematic of a liposome; hydrophobic drugs can be loaded into the aqueous interior while lipophilic drugs are contained within the bilayer. Liposomes can be surface functionalized (with PEG for example) to increase absorption within the body and liposomes can also fuse with cell membranes to deliver the interior contents. Liposomes have currently found use in delivering therapeutics such as vaccines (36) and the cancer drug doxorubicin (37).

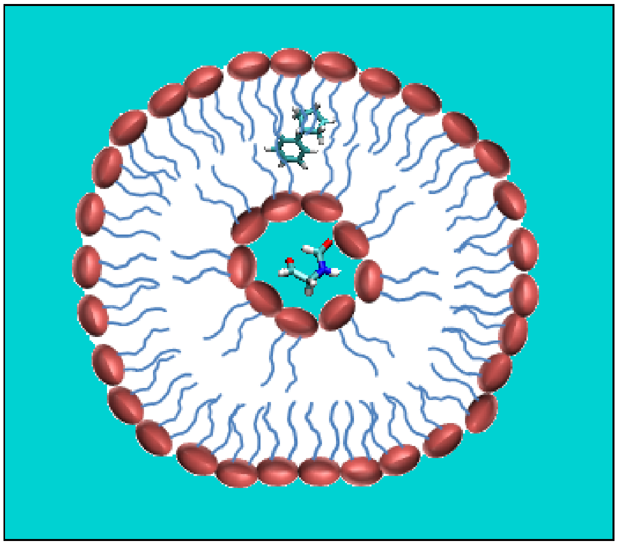

Figure 2: Schematic drawing of a liposome. The aqueous interior can be loaded with hydrophilic drugs while the lipophilic drugs can be loaded within the lipid tail region.

Finally, nanoparticles which generate their activity upon receiving a specific stimulus (activated nanoparticles) are being developed for various applications. Nanoparticle carriers can be formulated to respond to, for example, changes in pH. At the neutral pH of the body a drug can be contained within a specific carrier (liposome, polymer matrix, etc.). When the carrier enters the cell, it is diverted to the endosome which has an acidic pH around 6. The acidic pH induces a conformational change in the carrier complex, releasing the drug (38). Another type of activated nanoparticle is one that is able to respond to a magnetic field. Magnetic nanoparticles can be directed to specific sites within the body by placing a static magnet in the desired location (39). Similarly, magnetic nanoparticles small enough exhibit superparamagnetism can respond to an externally applied, oscillating magnetic field and dissipate heat; useful in thermotherapy of tumors (40).

1.2.3 Nanoparticle Interaction with Biological Molecules

Nanoparticle interfacial interactions with polymers and surfactants occur when the particle reaches its targeted destination. Many drug targets are proteins in the body (41). Proteins are biological polymers made up of amino acids monomers and have a specific three-dimensional structure. The knowledge of how a nanoparticle therapeutic interacts with a protein is paramount in determining the efficacy of the nanoparticle treatment. To enhance delivery and interaction with a specific cell type, nanoparticles can be conjugated with targeting ligands (42). In general, diseased cells (i.e. cancer cells) present specific surface markers (receptor proteins) such as human epidermal growth factor receptor 2 (HER2) in the case of certain breast cancer cells (43) and luteinizing hormone-releasing hormone (LHRH) receptors expressed on the surface of prostate cancer cells (44) that are down-regulated or absent in healthy cells. Another point of interaction between a nanoparticle therapeutic and cells is with the lipids that comprise the cell membrane. Lipids are surfactant-like amphiphilic molecules that form a barrier between the inside and outside of a cell and can be targets for therapy. Facilitating the interaction of nanoparticles with membrane lipids could have great effects on drug delivery such as liposomes fusing with cell membranes to release encapsulated drug, stimulating nanoparticle internalization (endocytosis) into the cell (45), inducing particle adherence to the cell membrane (46), or causing disruption of the cell membrane, altering electrochemical gradients between the interior and exterior of the cell (47). Like protein receptors over-expressed on the surface of cancer cells, the cell membranes of cancer cells too can show different lipid compositions to that of healthy cells which can be exploited for targeting purposes. As such, knowledge of the specific interactions of nanoparticles and the proteins and lipids in the body would prove very useful in a variety of areas of drug delivery.

1.3 Computational Nanotechnology

The interaction of polymers and surfactants with nanoparticles (and nanoparticle targets) occurs on very small scales and is an area where computation have proved very useful. For example, simulation has been used to determine where a ligand binds to a protein with the aim of designing drugs which work as antagonists (48). G-Protein Coupled Receptors (GPCR) are a class of membrane receptors involved in signal transduction pathways and account for approximately 40% of all prescription drug targets (49). These proteins however, are very difficult to crystallize and thus only a few 3D structures are known. Computer simulation and homology modeling have been very influential in predicting GPCR 3D structure and ligand interactions for rational drug design (50); (51). Molecular simulation has also been useful in determining the binding energy of nanoparticles to cell surfaces (52), analyzing how nanoparticles may penetrate cell membranes (53) and in screening large libraries of drug molecules to aid in drug design and discovery (17). Finally, simulation has been used to elucidate which surfactants and polymers have the most favorable interaction energies with crystal surfaces to determine which would be the best in quenching crystal growth (33). The interaction of polymers and surfactants with nanoparticles (and nanoparticle targets) is at the forefront of this work. Specifically, this thesis will explore the interaction of nanoparticles and nanoparticle polymeric coatings with lipid bilayers (surfactants), the interaction of engineered micellular nanoparticles with receptor proteins, and the interaction of polymers with nanoparticles crystallizing from solution.

1.4 Dissertation Objectives and Organization

In the preceding, the current background, theory, and motives behind computational simulation of interfacial interactions of polymers and surfactants with nanoparticles are addressed in a generalized fashion. Of note are the insights to be gained from computationally simulating and observing the specific molecular interactions that occur in nanoparticle systems which are not easily accessed experimentally. The remainder of this thesis will be devoted to three case studies in which polymer-surfactant-nanoparticle interfacial interactions play a significant role and the resulting insights gained from their simulation. The following are the systems to be computationally studied, the aims of study, the corresponding chapters, and the intended goals to be addressed:

Aim I: **To use molecular simulation methods to study the stability of a model cell membrane (lipid bilayer) under an applied stress in the presence and absence of polymer in order to mimic the interactions that occur in magnetic fluid hyperthermia, a treatment for cancerous tumors involving magnetic nanoparticles in an externally applied, oscillating magnetic field. This is done both on an atomistic level in the absence of polymer, and on a larger, coarse-grained level in the presence of a representative magnetic nanoparticle coating, the copolymer poly(ethylene oxide) – poly(ethyl ethylene). Specifically, the focus is on calculating the energy necessary to rupture a lipid bilayer to determine if a magnetic nanoparticle, in a given magnetic field, could transmit stresses to the cell membrane sufficient to induce rupture. Additionally, the effects of polymer properties on mechanical rupture of a cell membrane under stress are explored**; this will be presented in Chapter II.

Aim II: **Coarse-grained Molecular Dynamics are applied to study the interaction of engineered, micelle-forming, amphiphilic macromolecules interacting with the human scavenger receptor A for use in the prevention of oxidized low-density lipoproteins uptake as a means to prevent and treat atherosclerosis. The focus is on the structural and electrostatic properties of the macromolecules (charge and**

charge location) to determine the optimal interaction with Scavenger Receptor A and to establish if micellization is a necessary property for successful blocking to occur; this will be presented in Chapter III.

Aim III: **To develop a simulation platform using Monte Carlo and Molecular Dynamics simulations to study pharmaceutical nanocrystal nucleation of drug molecules from solution in the presence of polymers. The structural and energetic properties of polymer-drug systems are investigated with the goal of determining factors that act to increase or decrease the energetic barrier to drug nucleation with application to the nucleation rate**; this will be presented in Chapter IV.

Chapter V describes the conclusions as well as the recommendations for future work based on the additional open questions discovered through the course of this investigation. In summary, it is believed that this work will provide increased understanding surrounding the molecular mechanisms underlying the three cases under study, allowing for optimization of the processes in order to develop more effective materials and treatments for biomedical and pharmaceutical applications.

1.5 Methodology: Molecular Simulation Techniques

The work of this thesis revolves around molecular simulation techniques and their applications to solve specific problems in the area of biomedical and pharmaceutical nanotechnology. The remainder of this chapter will focus on a general background of molecular simulation and the specific techniques that will be employed in subsequent chapters.

Molecular simulation is a general term referring to computational modeling of molecular thermodynamics. Dependent on the question, there are a variety of methodologies for studying the interactions of atoms, molecules, or assemblies of molecules in static or dynamic, equilibrium or non-equilibrium settings. The first molecular simulations of liquids were carried out following World War II on the MANIAC computer at Los Alamos (54). They used the Monte Carlo (MC) simulation technique which generates a series of random molecular configurations based on an inter-atomic potential. Through the language of statistical mechanics, the probabilities of observing different configurations can be related to thermodynamic observables (internal energy, temperature, pressure, free energy, etc.). Later in 1959, Alder and Wainwright developed the Molecular Dynamics (MD) simulation method which solves Newton's classical equations of motion to study dynamical behavior of atomic systems (55). Since this time there have been significant advances in both computational power and computer algorithms allowing for the simulation of larger and larger systems. MD has found particular use in the study of the protein folding problem (56) where the aim is to use molecular simulation to predict the 3D-folded structure of a protein based solely upon its atomic sequence. Using current hardware and techniques, small proteins are able to be simulated for upwards of 1 ms (57); (58) through most simulations are commonly on the order of tens to hundreds of nanoseconds (59); (60) for atomistic simulations and hundreds of nanoseconds to microseconds for lower-resolution models (61); (62).

Similarly, MC has seen a boom in the available methodologies and applications such as Widom insertion (63), Grand-Canonical MC (64), Gibbs Ensemble MC (65), and Gauge-cell MC (66) for the study of a variety of different systems. Figure 3 shows a schematic of the length and time scales accessible to various computational simulation techniques. The boxed region is the area pertinent to nanoparticle interfacial interactions: less than one nanometer to hundreds of nanometers and picoseconds to microseconds. Below are described in further detail MD simulation, MC simulation, and a computational technique to decrease the number of degrees of freedom in a simulation termed coarse-graining (CG).

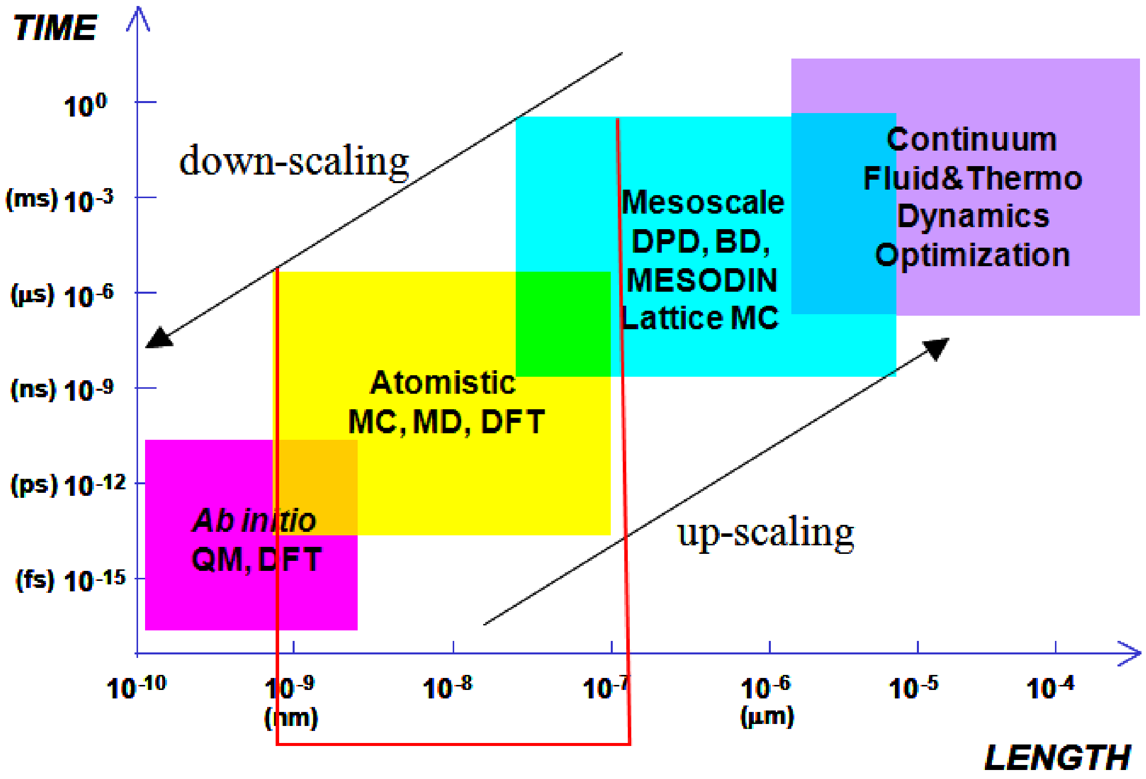
TIME
10^0
(ms) 10^{-3}
(µs) 10^{-6}
(ns) 10^{-9}
(ps) 10^{-12}
(fs) 10^{-15}
down-scaling
Continuum
Fluid&Thermo
Dynamics
Optimization
Mesoscale
DPD, BD,
MESODIN
Lattice MC
Atomistic
MC, MD, DFT
Ab initio
QM, DFT
up-scaling
10^{-10}
10^{-9}
(nm)
10^{-8}
10^{-7}
10^{-6}
(µm)
10^{-5}
10^{-4}
LENGTH

Figure 3: Schematic highlighting the various computational methods for simulating different length and time scales. Figure courtesy of A. Neimark.

1.5.1 Molecular Dynamics Simulation

MD is a computer simulation technique used to study the evolution of a collection of atoms or molecules in time. The interaction between atoms in the system is specified by providing a potential function (V) which incorporates both the bonded interactions (bond stretching, angle bending, tortional terms) and the non-bonded interactions (van der Waals and electrostatic interactions) of the system of interest. The combination of the bonded and non-bonded interactions for the components of the system is referred to as the force-field. At the outset of the simulation, a system is composed of N atoms are placed in a simulation cell of volume V. All atoms are given initial positions (r_i) and velocities (v_i), and Newtonian mechanics is used to determine the positions and velocities of the particles at subsequent times by integrating their equations of motion according to the equation:

$$\sum F_i = m_i \boldsymbol{a}_i = -\nabla V \tag{1}$$

where F_i is the sum of forces acting on particle i, m_i is the mass of particle i, a_i is the acceleration of particle i, and V is the potential function. The result is a trajectory in 6N-dimesnional space (3N positions and 3N momenta) which represent the states accessible to the system in a given ensemble. From the trajectory, one can observe specific molecular interactions and calculate thermodynamic, structural, or transport properties of the system of interest by taking the time-average of those quantities throughout the simulation. The ergodic hypothesis states that in the limit of long times, the time-average of a quantity is equal to the ensemble-average (67), meaning that the results from MD and MC simulation should coincide. MD may be run in any number of ensembles (the variables kept constrained), but the most common are the canonical ensemble (N,V,T):

number of particles, volume, and temperature are fixed, and the isothermal-isobaric ensemble (N,P,T): number of particles, pressure, and temperature are fixed.

The general flow of an MD simulation proceeds as follows: One creates a topology in which the potential function is specified, containing all of the bonded and non-bonded interactions between atoms in the system. Next, an initial set of coordinates and velocities for each particle in the system are given. This is followed by energy minimization which attempts to relieve bad contacts -steric clashes- and find a minimum on the potential energy surface for which to begin simulation. The simulation proceeds by determining the forces acting on each particle of the system arising from the potential function. Using Eqn. 1, the positions and velocities of each particle are evolved in time. This is followed by the application of a constraint algorithm particular to the ensemble. For ensembles in which the temperature is kept as a fixed quantity, a thermostatting algorithm scales the velocities of each particle such that the average temperature approaches a desired target. A similar algorithm is applied when the pressure is to be kept fixed. A barostat algorithm adjusts the volume of the simulation cell such that the average pressure in the system approaches a target quantity.

The benefit of atomistic MD is that one is able to explore nanoscale system properties and the exact interactions between system components on a molecular level. This includes, for example, the surface tension of a lipid (surfactant) system, formation of pores in a bilayer system, and the interaction of polymers and surfactants with the surface of a drug crystal. Though MD can be useful to study specific molecular interactions, it is computationally expensive for large systems and long time scales. Therefore, other techniques are necessary for the study of larger systems with phenomena that operate at on longer time scales. In this work, we use atomistic MD simulation to explore rupture of a lipid bilayer under stress.

1.5.2 Monte Carlo Simulation

MC simulation is a technique similar to MD but rather than evolving a system through time by solving dynamical equations, trial moves are made to generate random system configurations. The theory behind MC simulation begins with Eqn. 2 for the partition function (Q) of a given system in the canonical ensemble (68):

$$Q_{NVT} = \frac{1}{N!}\frac{1}{h^{3N}}\int d\boldsymbol{r}d\boldsymbol{p}\, exp(-H(\boldsymbol{r},\boldsymbol{p})/k_B T) \tag{2}$$

where N is the number of atoms in the system, *h* is Planck's constant, ***r*** and ***p*** are the atomic positions and momenta respectively, H is the Hamiltonian describing the energy of the system, k_B is Boltzmann's constant, and T is the temperature. The system Hamiltonian (H) can be separated into the sum of the kinetic and potential energy functions. If it is assumed that the potential energy is a function of position only (not a function of momentum) then the integral over the momenta in Eqn. 2 can be carried out analytically to yield Eqn. 3:

$$Q_{NVT} = \frac{1}{N!}\left(\frac{2\pi mkT}{h^2}\right)^{3N/2} \int d\boldsymbol{r}\, exp(-V(\boldsymbol{r})/kT) \tag{3}$$

This integral can be evaluated through standard numerical techniques, but this proves to be very inefficient as the integral vanishes for the majority of points in the phase space (there exist many configurations in which the Boltzmann factor, $exp(-V/k_BT)$, is vanishingly small). The integration of Eqn. 3 is generally done using importance sampling in which one attempts to evaluate the integral only at points in which it is non-zero. This is known as Metropolis sampling (54). As in MD simulation, one begins from an energy minimized configuration of a stable system. From this initial configuration, trial moves are made in which the system is perturbed by a small amount (i.e. particle displacement, particle insertion or removal, system volume change, etc.). The system energies are calculated for the initial (old) and perturbed (new) states and the probability that the perturbed state is an acceptable configuration is determined by a normally distributed random number based on Boltzmann weighting.

$$accept(old \rightarrow new) = \begin{cases} exp\left(-\beta(\Delta V_{old\rightarrow new})\right) & if\ E_{new} > \ E_{old} \\ 1 & if\ E_{new} < E_{old} \end{cases} \quad (4)$$

Many configurations are sampled until proper equilibrium criteria are reached, upon which thermodynamic properties are calculated according to statistical mechanical definitions as:

$$\langle A \rangle = \frac{\sum_i A \exp{(-\beta E_i)}}{\sum_j -\beta E_j} \quad (5)$$

where A is the observable to be calculated, E_i is the energy of state (configuration) *i*, $\beta = 1/k_BT$, and bracket parentheses indicate an average. As stated above, unlike MD, MC simulations have no unit of time. This has the benefit that there need not be a direct physical transition between the old state and the new state; the only constraint is that there is a proper distribution at equilibrium. In this thesis, MC simulation is used to study nucleation of drug molecules in the presence of polymeric additives.

1.5.3 Coarse-Graining

Coarse-graining (CG) involves the reduction of the molecular degrees of freedom in order to reduce computational cost and is applicable to both MC and MD simulation. This is done by combining several atoms or molecules into large, pseudo-atoms or 'beads'. In doing so, the number of interacting particles in the system can be reduced significantly, lowering the total number of calculations that need to be performed. In addition CG creates a smoother potential energy surface allowing for longer time-steps and different algorithms for calculating the bonded and non-bonded system interactions. For example, one such CG simulation technique is Dissipative Particle Dynamics (DPD) (69). Here, several atoms (~4) are lumped together into beads representing a specific fluid volume. Rather than interact through hard-core repulsive interactions as in MD, the beads interact through a soft-core repulsive potential. This allows for much larger time steps than traditional MD. Another CG scheme more closely related to MD is the MARTINI force field (70). In this force field, 4 heavy atoms (i.e. not hydrogen) are lumped together, but the standard MD algorithm remains unchanged. This allows for increased system sizes and simulations for longer times. In this work, we use coarse-grained techniques to study the interaction of polymers with a lipid bilayer under stress as well as the interaction of engineered micelle-forming macromolecules with human scavenger receptor A.

Chapter 2 Energetics of Cell Membrane Rupture by Magnetic Nanoparticles in Magnetic Fluid Hyperthermia

The treatment of cancer generally involves administration of chemotherapeutic drugs which are highly toxic for not just cancerous cells, but other cells in the body as well. The result is that the treatment is exceedingly strenuous on the patient such that, at a certain point, the costs of treatment can outweigh the benefit. As a consequence, there is always a drive to develop new, highly effective cancer treatments with minimal side-effects. One particular method termed magnetic fluid hyperthermia (MFH) involves the use of magnetic nanoparticles in an oscillating magnetic field for the thermal destruction of tumors. This is a relatively new procedure and requires further optimization until successful application in a clinical setting can be realized as treatments require excessively strong magnetic fields. In this chapter we use molecular simulation methods to study the stability of a model cell membrane (lipid bilayer) under an applied stress in the presence and absence of polymer in order to mimic the nano-scale interactions that occur in MFH. This is done to determine if in addition to the thermal component, there also exists a mechanical component to damaging cells. The simulations are performed on an atomistic level in the absence of polymer, and on a larger CG level in the presence of a representative magnetic nanoparticle coating, the copolymer poly(ethylene oxide) – poly(ethyl ethylene). Specifically, the focus is on calculating the energy necessary to rupture a lipid bilayer (in the presence and absence of polymer) to determine if a magnetic nanoparticle in a given magnetic field, could transmit stresses to the cell membrane sufficient to induce rupture.

2.1 Cancer Nanotechnology

Cancer is a broad classification for a variety of diseases that are defined by uncontrolled cell growth and proliferation. It is the leading cause of death in developed countries and the second leading cause of death in developing countries (World Health Organization, 2004). One significant hurdle to the successful treatment of cancer is delivery of a sufficient amount of therapeutic drug with little or no side effects. Nanotechnology is particularly suited to overcome some of the traditional barriers to cancer treatment stemming from its ability to selectively manipulate therapeutics on the molecular level to provide for their targeted delivery while also surmounting biological barriers (71). In recent years, there has been a great deal of success in the use of nanotechnology for the treatment of cancer, too widespread to enumerate here. For further detail the reader is referred to a review by Ferrari (72) and the references therein.

One promising method for the treatment of cancer is using what are termed 'activated' nanoparticles. In this sense, activated refers to the ability of the therapeutic to respond to a stimulus either within the biological environment or one that is externally applied. One example of this is pH sensitive nanogels. It has been shown that the tumor microenvironment is more acidic than normal tissues (73) and this can be exploited in the delivery of cancer therapeutics. Nanogels can be fabricated to carry a cancer drug contained within its matrix at normal pH. When the nanogel reaches the acidic environment of a tumor, the nanogel can be made to shrink or swell, releasing the cancer drug. A second example of activated nanoparticles are those which respond to a magnetic field. Cancer cells have been shown to be more sensitive to heat damage (hyperthermia) than healthy cells, and thus magnetic nanoparticles that dissipate heat in response to an externally applied magnetic field could be an effective treatment for cancer. In this chapter, we will simulate the energy required to rupture a model cell membrane to determine if in addition to thermal effects, it is possible that local stresses generated by the nanoparticles could further damage cancer cells.

2.2 Magnetic Fluid Hyperthermia

Current treatments for cancer are either highly invasive, such as surgery, or very taxing on the patient, as in radiation and chemotherapy. Additionally, established treatments for many types of cancer have very low success rates. These limitations stimulate the development of alternative treatments such as nanotechnology and nanoparticles for use in early stage detection and treatment of cancer (72). One promising alternative to standard practices is MFH, in which magnetic nanoparticles are delivered to a cancer tumor and a high frequency oscillating magnetic field is applied. When subjected to an oscillating magnetic field the nanoparticle non-equilibrium response is energy dissipation through either Néel relaxation (relaxation of the magnetic dipole within the crystal lattice) or Brownian relaxation (physical rotation of the particle to align with the field) producing a localized rise in temperature. Because cancer cells are more susceptible to heat damage than healthy cells (74), the treatment has been shown to result in tumor suppression (75). Hyperthermic conditions have also been shown to increase the sensitivity of cells to radiation and chemotherapy making MFH ideal for combination therapy (76); (77). Currently, the major hurdle associated with MFH is obtaining an adequate distribution of heat confined solely to the tumor mass. Studies have shown that substantial peripheral heating can occur resulting in excessive patient pain and damage to surrounding healthy tissue (78); (79). As a result, there is interest in reducing the amplitude and frequency of the applied magnetic field while still maintaining efficacy in tumor suppression. One possible method to satisfy this restraint is to enhance tumor cell destruction by mechanical means. Although energy dissipation is widely accepted as the dominant mechanism leading to cell death it is possible that shear due to rotation of nanoparticles near the cell membrane may transmit forces sufficient to rupture the membrane, especially for larger nanoparticles with magnetic dipoles that are locked into their nanoparticle crystal structure (i.e., magnetically blocked nanoparticles). In support of this, there are reports in the literature which indicate that a rise in temperature is not required to induce cell death. In a study conducted by Halbreich et al. (80) magnetic nanoparticles in an oscillating magnetic field were used to damage mouse liver cells *in vivo*. Cell death was found to occur in the absence of any observable temperature increase, suggesting the possibility that other mechanisms besides hyperthermia were involved. In a recent study, Nappini et al. (81) examined cobalt ferrite nanoparticles coated with oleic acid contained in phosphatidylcholine (PC) liposomes. When subjected to an alternating magnetic field, the magnetoliposomes caused a temperature increase to 40°C and induced instability of the of the surrounding PC bilayer. When compared to magnetoliposomes that were thermally heated to 40°C without the application of a magnetic field, the instability effect was lost leading the authors to conclude that temperature only weakly influences PC bilayer stability, and instability is more likely resultant from nanoparticle response to the applied field.

In MFH, the nanoparticles used are typically on the order of 10-50 nm in diameter and the magnetic fields oscillate at ~100 kHz (82); (83); (84). The small scale interaction of magnetic nanoparticles with a cell membrane makes MFH difficult to study in real time. In the majority of studies, the general mechanism to assess the result of MFH on cells is to compare electron micrographs of MFH treated and untreated (or heat treated) cells. Many studies are able to assess the heat generated during MFH treatment in real time (80); (85), but there are not adequate methods to assess the specific interaction of magnetic nanoparticles with a cell membrane to determine if mechanical mechanisms play a role in cell destruction. As such, computer simulation can aid in understanding some of the molecular mechanisms present in MFH.

2.2.1 A Lipid Bilayer under Stress as a Model for Magnetic Fluid Hyperthermia

As a first approximation, it is possible to model the cell membrane as a lipid bilayer in water. This system has been previously studied using MD simulations, and researchers have been able to reproduce experimental results for many equilibrium thermodynamic properties such as density, area and volume per lipid, bilayer repeat distance etc. (See (86) and (87) for reviews). MD has also been used to study pore formation and stability of lipid bilayers subject to stress (88); (89). Tieleman et al. induced pore formation using an applied mechanical stress (90). They found that when tension was applied in the form of a lateral pressure greater than -200 bar, a pore would form in the bilayer. This pore grew rapidly in size until the bilayer became destabilized. Leontiadou et al. performed a similar study (91). They began with a bilayer containing a pre-existing pore and subjected the bilayer to tension in the form of a lateral pressure finding that at varying levels of stress, up to a surface tension of 38 mN m^{-1}, the pores were stable at a particular size which was correlated to the applied stress. If the applied stress was greater than 38 mN m^{-1}, the pores would grow indefinitely, resulting in bilayer rupture with the speed of rupture dependent on the magnitude of the applied stress. Additionally, in comparison to a bilayer without a preformed pore, Leontiadou et al. (91) found results consistent with Tieleman et al. in that a very high stress of approximately 90 mN m^{-1} (-200 bar lateral pressure) is required to form an unstable pore. This led to the conclusion that pore formation and expansion, and hence bilayer strength, is dependent on the loading rate of the stress. This is consistent with the theory of Evans and Heinrich who hypothesized that at low loading rates, pore expansion becomes rate-limiting whereas at high loading rates pore formation is rate limiting (92). Groot and Rabone took a more in-depth look at rupture of a lipid bilayer (93). Using DPD (69) they looked at bilayer rupture in the presence of surfactants. To do so, they subjected the bilayer to normal strain increments while monitoring the surface tension of the bilayer. When the surface tension reached a peak and subsequently sharply decreased, this was taken as signifying rupture of the bilayer. Their simulations showed that a lipid bilayer could withstand a surface tension of 67 mN m^{-1} prior to rupture.

Similar systems have also been studied experimentally. The most common procedure for examining properties such as area expansion, area compressibility modulus, and rupture tension is through a micropipette aspiration technique (94); (95); (96); (97); (98). Here, a small portion of a vesicle is sucked through the tip of a micropipette under a defined pressure drop, and the vesicle deformation and rupture tension can be measured using a high-speed camera. Generally, lipid vesicles rupture following an area expansion of ~5% and an external tension on the order of

10-30 mN m^{-1}. Even very tough bilayers made from high molecular weight diblock co-polymers cannot sustain more than 20% area expansion prior to rupture (99). However, values for rupture tension and area expansion are both dependent on the loading rate (96).

None of the aforementioned studies focused on rupture of lipid bilayers under shear, which is what may occur in MFH. The existing literature pertaining to simulations of lipid bilayers under shear is sparse. Blood et al. simulated the response of a solvent shear flow producing a force on the bilayer of 2.9x10^{-3} pN finding that the flow increased the order of the lipids in the bilayer (100). Shkulipa et al. (101) used Lees-Edwards sliding boundary conditions (67) to obtain the surface shear viscosity and intermolecular friction of amphiphilic bilayers containing lipids of varying tail lengths. To the best of our knowledge, simulations of lipid bilayer rupture under shear stress are non-existent. In addition, given that intermolecular interactions of a bilayer under tension are different from those occurring under shear; it is not a straightforward expectation that a bilayer would have the same strength for rupture in these two cases. Here we employ MD simulation of a lipid bilayer under both tension and shear stress to explore the rupture phenomena and correlate the forces necessary to rupture a lipid bilayer with the forces a rotating nanoparticle could generate in MFH.

2.3 Molecular Dynamics Simulations of a Lipid Bilayer under Stress

The cell membrane in our simulations was modeled as a lipid bilayer, taken from the website of Dr. P. Tieleman (www.moose.bio.ucalgary.ca), consisting of 128 dipalmitoylphosphatidylcholine (DPPC) lipids (64 lipids per leaflet) and 3655 SPC water molecules yielding a fully solvated bilayer. All simulations began by performing an energy minimization on the bilayer, followed by a 5 ns equilibration period in an NPT ensemble (Berendsen temperature coupling at 310°K and isotropic Berendsen pressure coupling at 1 bar (107)). Figure 4 shows the lipid bilayer following energy minimization and equilibration with a resulting simulation cell size of L_x x L_y x L_z = $(6.4\text{ nm})^3$, the initial configuration for all rupture runs.

All MD simulations were performed with the software package GROMACS v. 3.3.3 (102). The force-field used was developed by Berger et al. (103) and is based on the united-atom version of the Optimized Potential for Liquid Simulations (OPLS) force-field (104). In this approach, all the CH_x groups (with x = 1, 2, or 3) are modeled as single units, while other heavy atoms are modeled as exact atoms. For water, the Simple Point Charge (SPC) model of Berendsen et al. (105) was used. Consistent with the force-field, we used a cut-off for Lennard-Jones interactions of 1.4 nm and electrostatics were treated using a 1.0 nm cut-off and the Particle Mesh Ewald (PME) algorithm (106) for long-range interactions.

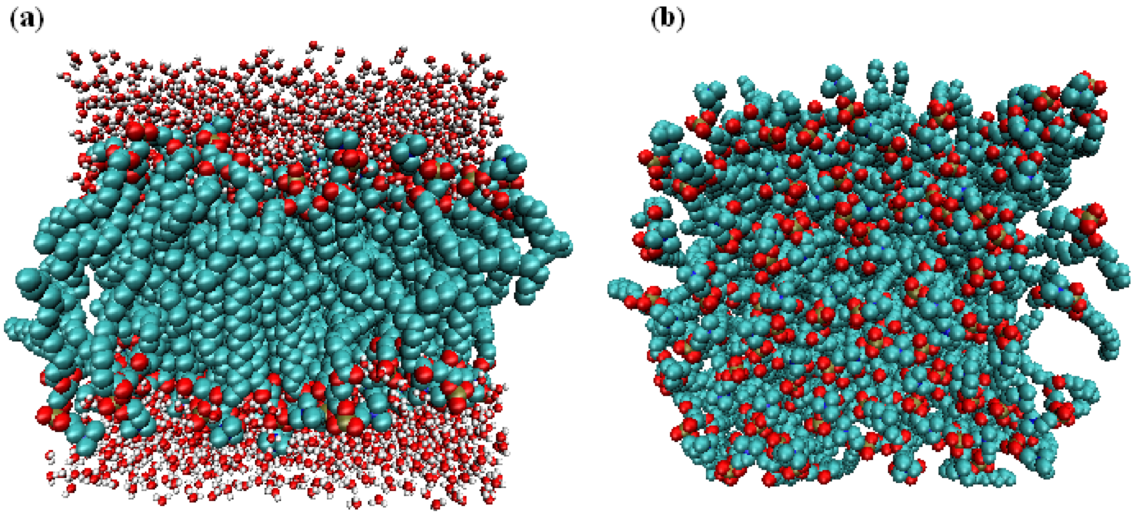

Figure 4: DPPC lipid bilayer following energy minimization and 5 ns of equilibration time. **(a)** Side-view of the bilayer. **(b)** Top-down view of the bilayer with water molecules omitted for clarity.

Assessment of bilayer rupture was performed in three ways. First we performed direct examination of the simulation snapshots for a qualitative view of the rupture. Secondly, we computed variations in the surface tension as a function of bilayer area. Finally, we monitored the diffusion coefficient of water molecules through the bilayer.

The surface tension of a bilayer with a surface normal in the *z*-direction can be found from the pressure tensor *P* through the relation (108):

$$\gamma = \int_{Z_1}^{Z_2} \left[P_N(Z) - P_T(Z) \right] dZ \tag{6}$$

with γ being the surface tension, P_N the pressure normal to the bilayer and P_T the tangential pressure. In an MD simulation, this equation becomes (109):

$$\gamma = L_Z \left[P_Z - \left(P_X + P_Y \right) / 2 \right] \tag{7}$$

where L_Z is the size of the simulation cell in the *z*-direction and P_i is the pressure in the $i = x$, y, and *z*-directions respectively. We computed the surface tension as a function of bilayer area, noting that a sharp decrease in surface tension indicates the lipid bilayer had ruptured.

To determine the diffusion coefficient we calculated the mean-squared-displacement (MSD) of the water molecules in the z-direction during each relaxation period. Least squares fits were used to fit the MSD to a straight line, and the Einstein relation can then be used to calculate the diffusion coefficient *D*:

$$D = \frac{1}{2nt}\left\langle \left(r_i(t) - r_i(0)\right)^2 \right\rangle \tag{8}$$

where *n* is the number of dimensions, *t* is time, and r_i is the position of molecule *i*.

2.3.1 Bilayer Rupture by Incremental Tension

Following equilibration, incremental stretches were performed on the bilayer. The *x*- and *y*-coordinates of all atoms were incremented by a stretch-factor of λ while the *z*-coordinates were divided by a stretch-factor of λ^2. This transformation conserved the total volume of the bilayer. A stretch was applied instantaneously and followed by an NP_NAT relaxation period which kept the area of the bilayer fixed and a constant normal pressure of 1 bar. Performing the simulation in this manner allowed the bilayer to respond to the applied stress and maintain quasi-equilibrium. We analyzed three different values of λ: $\lambda = 1.03$, 1.04, and $\lambda = 1.05$. For every value of λ, each stretch was followed by a 3 ns relaxation period and an average measure of the surface tension of the bilayer was calculated over this relaxation period to obtain an estimate of the surface tension associated with that particular value of the bilayer area.

Figure 5 presents the response of the lipid bilayer surface tension to the imposed strain as a function of time for the case λ = 1.03. The value plotted is the running average of the surface tension over each strain increment. The instantaneous surface tension directly following each stretch was quite large; hence the axes of Fig. 5 have been truncated in order to show the physically relevant region in which the bilayer surface tension had reached its equilibrium value after each stretch. The equilibrium value is used in Fig. 6 which shows the surface tension of the bilayer as a function of the normalized area of the bilayer.

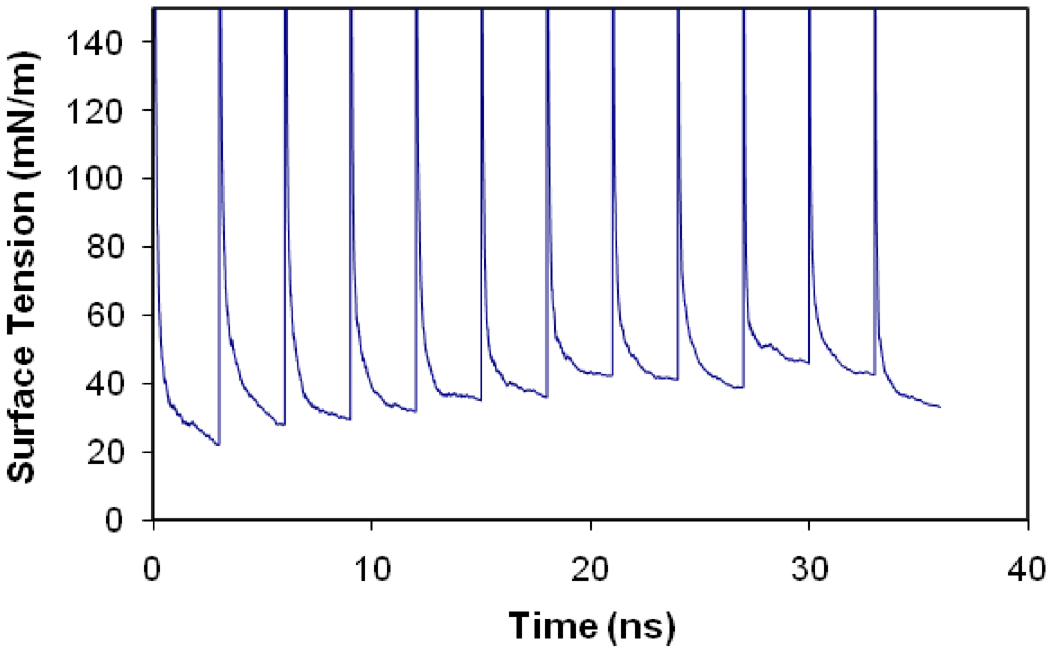

Figure 5: Running average of the surface tension following each bilayer stretch for λ = 1.03, corresponding to an area increase of 6%.

Figure 6 shows the change in surface tension of the bilayer with respect to the area of the membrane for each magnitude of strain examined. The abscissa is normalized to the area of an equilibrated bilayer, taken as the result of the equilibration run. As the area of the bilayer increased, the surface tension also increased up to a peak value. Further stretching of the bilayer beyond the peak value resulted in a decrease in surface tension. Interestingly, the bilayer ruptured at roughly the same tension independent of the magnitude of the strain. For each strain value the bilayer could be stretched to approximately double its initial area, with a corresponding surface tension of approximately 90 mN m^{-1}.

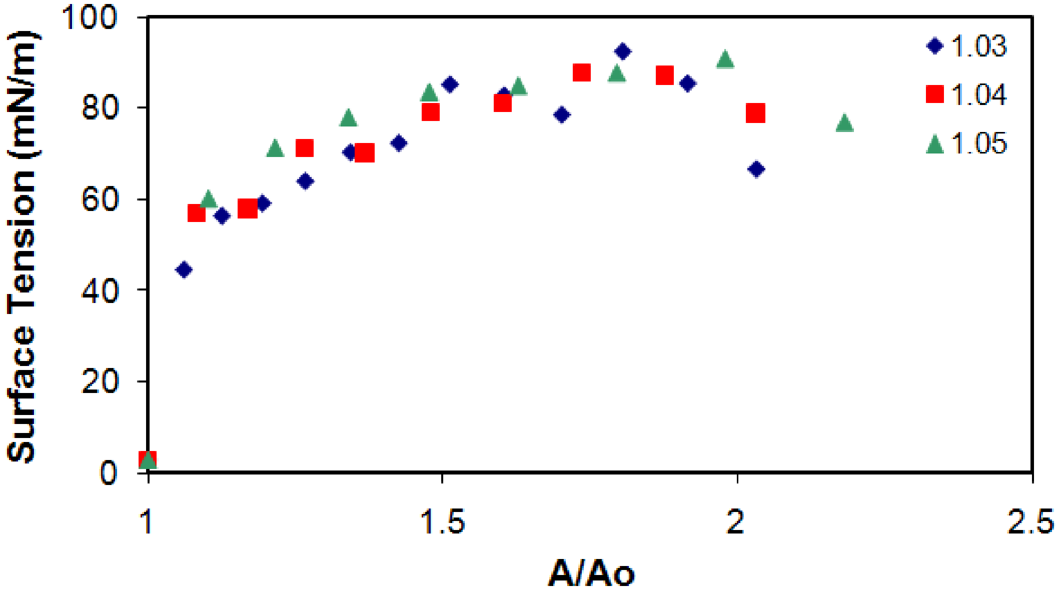

Figure 6: Surface tension vs. area for a DPPC bilayer stretched in its principal directions for stretch values of λ = 1.03, 1.04, and 1.05.

Figure 7 shows typical snapshots of the evolution of bilayer structure during a simulation. For the first several increments, stretching the bilayer did not seem to induce any noticeable pore formation. With subsequent stretches, small pores in the bilayer began to develop. These pores were transient and resealed within tens to hundreds of picoseconds. Eventually, the pores in the bilayer became very large, as indicated in Fig. 7c. Pores of this size were stable throughout the entire relaxation period of 3 ns and were observed under conditions that led to bilayer rupture.

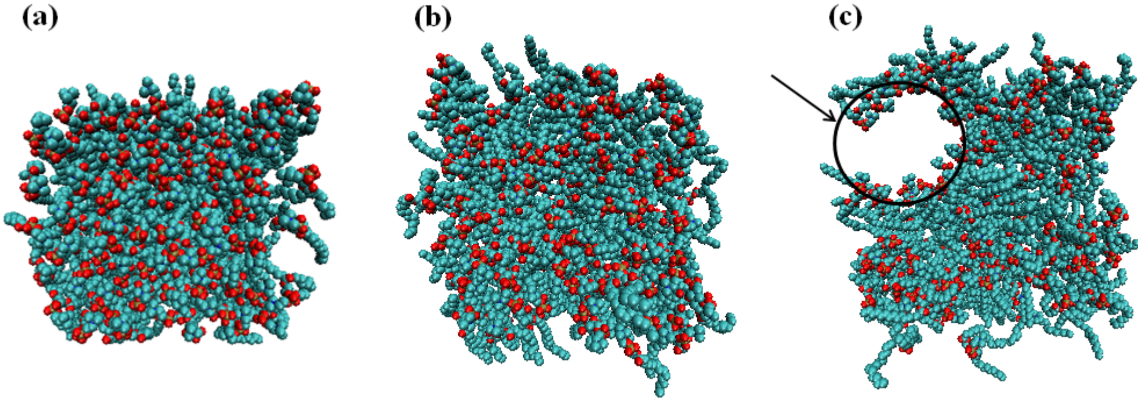

Figure 7: Representative snapshot of pore formation in the bilayer during incremental strain with λ = 1.04. **(a)** Initial configuration of the bilayer, **(b)** following 5 stretches (15 ns), and **(c)** following 9 stretches (27 ns).

Figure 8 shows the transverse diffusion coefficient of water molecules as a function of bilayer area. When stretched to double the initial area the diffusion coefficient perpendicular to the bilayer increased by roughly an order of magnitude, indicating water molecules flowing through the pores in the bilayer and thus, rupture. Initially, the diffusion of water perpendicular to the bilayer was small, ~$3\text{x}10^{-7}$ cm^2 s^{-1}, compared to the diffusion coefficient of bulk SPC water, $2.3\text{x}10^{-5}$ cm^2 s^{-1} (105). The small but noticeable downward trend present in the figure is a simulation artifact resulting from periodic boundary conditions and the progressive shrinking of the water layer as the bilayer area expanded.

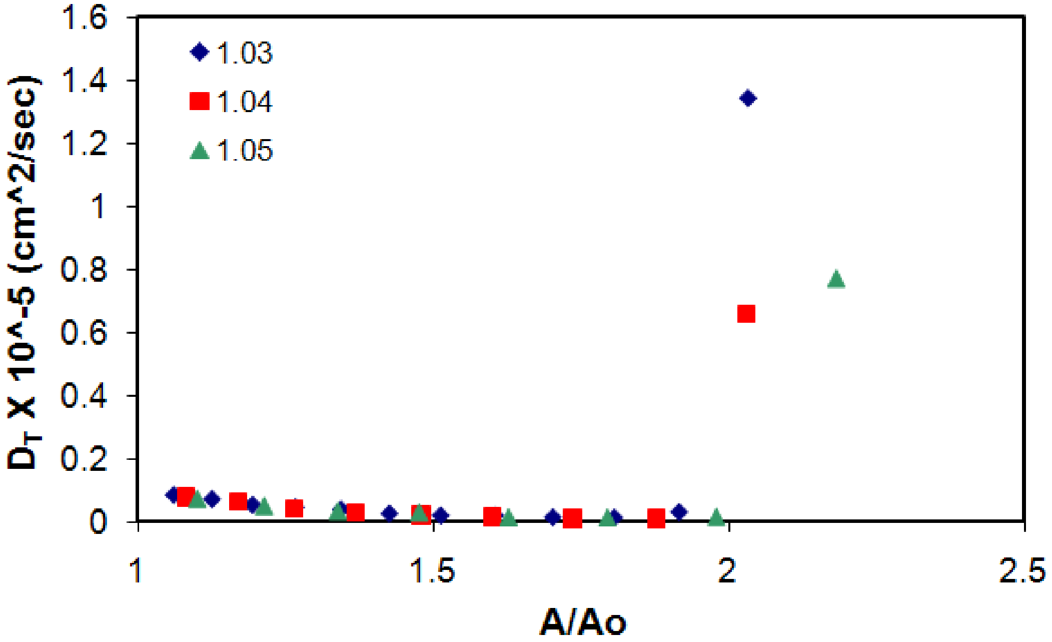

Figure 8: Diffusion coefficient perpendicular to the bilayer surface as a function of normalized bilayer area.

Our results are consistent with those found in (93) in that the bilayer could be stretched to double its initial area before stable pores began to develop. This was not entirely unexpected because even though different approaches were used, the volumes of each lipid molecule are roughly the same. Stretching the bilayer caused an increase in the average distance between lipid molecules, leading to an increase in the potential energy of the system. Eventually, the increase in intermolecular lipid distance became large enough that it was energetically favorable to form a stable pore. The value for the bilayer in our system to rupture was slightly higher than the one found in (93), largely due to the fact that we are working with different lipids. In addition, the authors in (93) used DPD simulation while our simulations were done with MD. Systems studied with MD are generally smaller and inherently more stable and will therefore require larger forces for rupture.

2.3.2 Bilayer Rupture by Incremental Shearing

The rotation of a nanoparticle responding to a magnetic field interacting in a cellular environment would likely result in a shear stress imparted on the cell surface. In our simulations, an acceleration was applied in the *x*-direction over the whole simulation box with the form:

$$a_x = A * \cos(2\pi * z / L_z - \pi / 2) \tag{9}$$

where A is the amplitude of the acceleration, z is the z-coordinate of a particular atom, and L_z is the height of the simulation box in the z-direction. In this way, shear acceleration was applied at the bilayer surface and smoothly shifted to zero at the center, as one moves away from the surface. The acceleration was applied for 10 ps in an NPT ensemble followed by a 3 ns relaxation period in an NP_NAT ensemble with the same parameters as described above. The chosen value A = 0.40 nm ps^{-2} for the amplitude of the acceleration in each increment of shear yielded a similar area increase as obtained in each increment of the tension simulations described above. We have looked at rupture of a lipid bilayer under strain to determine the maximum surface tension it can withstand in order to obtain an estimate of the energy that a rotating nanoparticle would need to produce to rupture a cell. However, a nanoparticle rotating in a cellular milieu would likely induce a shear force, rather than a tension on the lipid bilayer. Thus, it is of interest to study the response of a lipid bilayer to a shear stress.

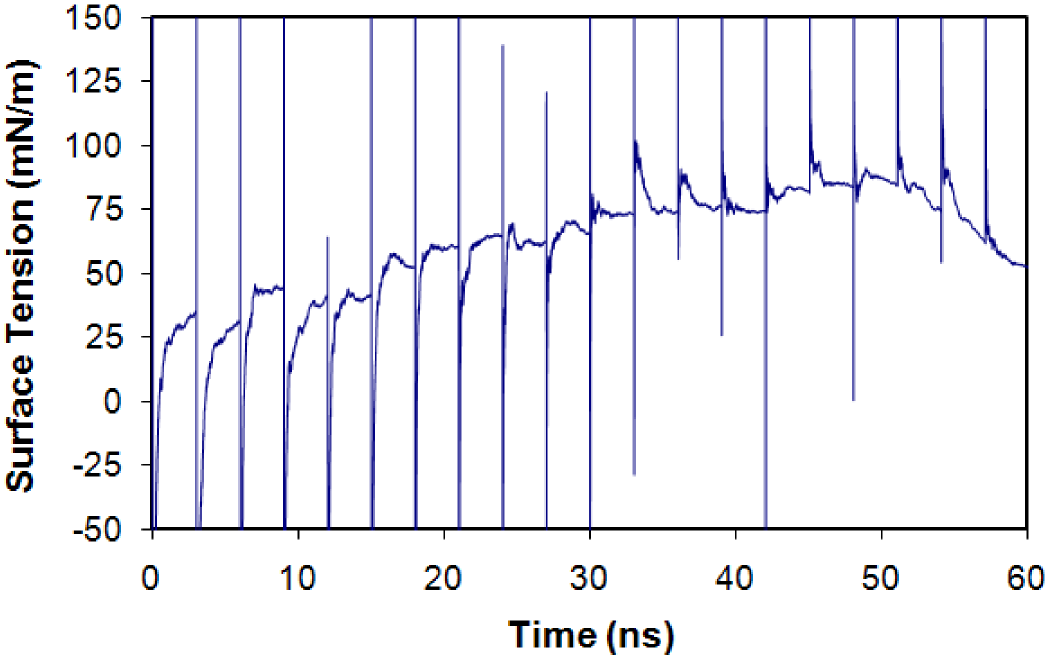

Figure 9: Running average of the surface tension as a function of time for each shear increment.

Figure 9 shows the running averages of the surface tension for each shear-relax iteration. In total, 20 shear-relax iterations were performed. The plot shows an oscillation in the surface tension during the shearing phase followed by a relaxation period of 3 ns where the surface tension decays. The equilibrium value of the surface tension was taken as the final average value during the relaxation period prior to a subsequent shear increment. Thus, each of these averages corresponds to a point value in surface tension in Fig. 10. Initial trials were run with different values of the relaxation time, and it was determined that 3 ns was sufficient for the surface tension to decay to a constant value following a particular shear increment.

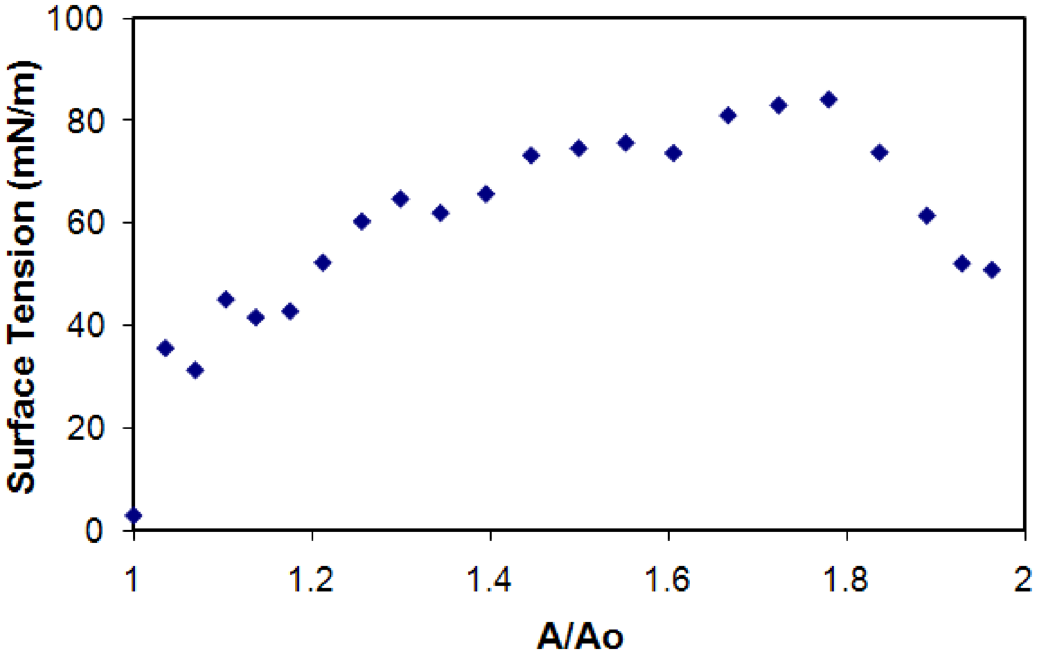

Figure 10: Surface tension vs. area for a DPPC bilayer subjected to incremental shearing.

Figure 10 shows a plot of the surface tension of the bilayer versus its area. As can be seen, the surface tension increased with increasing area until approximately 84 mN m^{-1} whereupon it began to sharply decrease down to 52 mN m^{-1}. This decrease is indicative of bilayer rupture. At this point a large number of water molecules were able to flow through the pores in the bilayer neutralizing the tension that was imparted by the shearing. The surface tension did decrease to its initial value at the start of the simulation due to the structure that is still present in the bilayer.

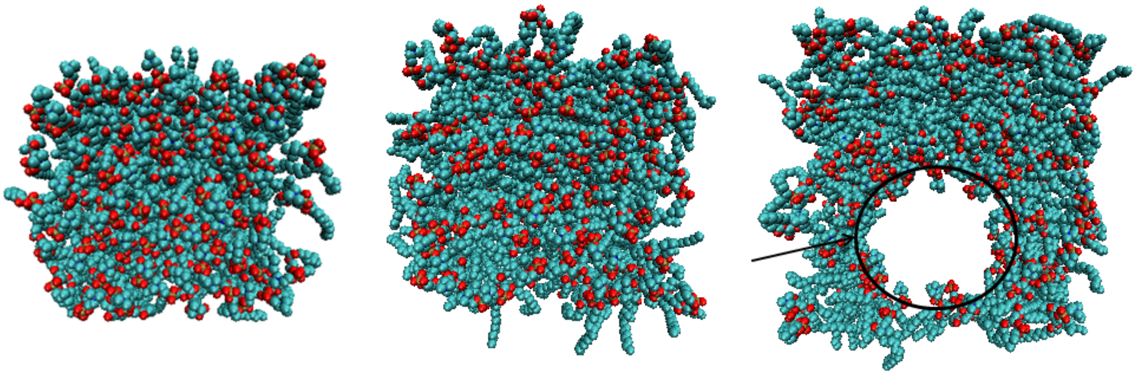

Figure 11: Representative snapshot of pore formation in the bilayer during incremental shearing. **(a)** Initial configuration of the bilayer following equilibration. **(b)** The bilayer following 10 shear increments (30.1 ns). **(c)** The bilayer following 20 shear increments (60.2 ns). The surface tension at this point is 52 mN m^{-1}.

Figure 11 shows the evolution in structure of the bilayer during the shearing simulations. Figure 11a shows the initial configuration of the bilayer prior to any external stimulus. Figure 11b shows the bilayer following 10 shear-increments. Evident in the snapshots is that the bilayer is still much intact, although at times there did appear small transient pores starting to develop during the 3 ns relaxation period. Figure 11c shows the bilayer following 20 shear-increments, with a large pore that is stable over the entire 3 ns relaxation period. This provides visual confirmation that bilayer rupture had in fact occurred. The transverse water diffusion coefficient is plotted in Fig. 12, obtaining similar results to the strain simulations.

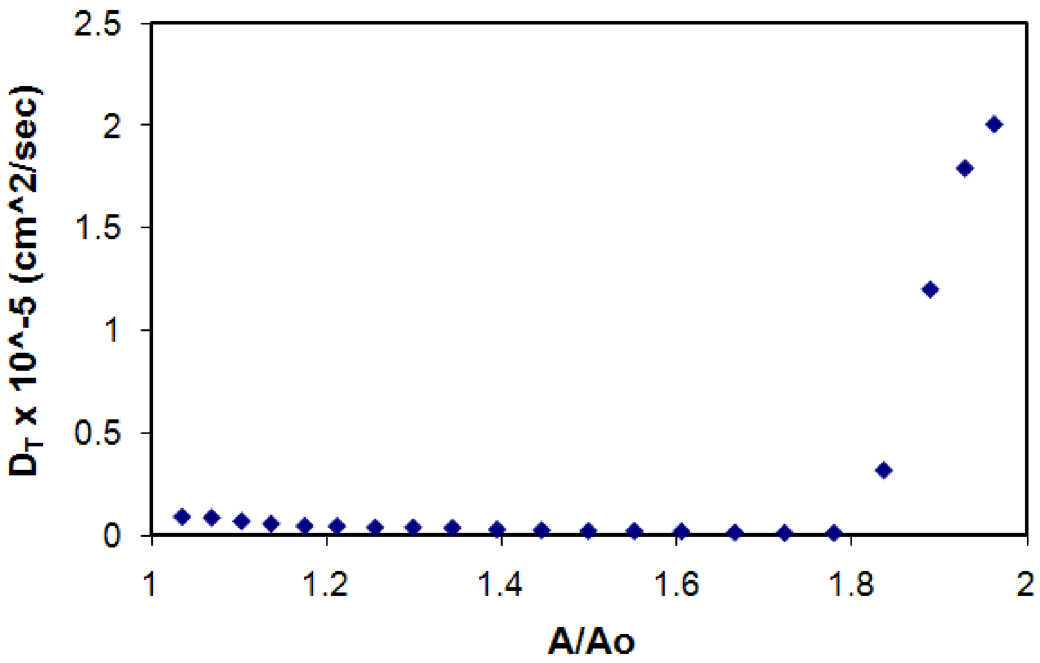

Figure 12: Diffusion coefficient perpendicular to the bilayer surface as a function of normalized bilayer area for the case of a bilayer under shear.

We found that we can produce bilayer rupture through incremental shearing as evidenced by the surface tension and water diffusion measurements. In comparing our shearing simulations to the incremental stretching simulations, it is seen that the two different methods of producing rupture do not behave in the same way. The strain and shearing simulations showed bilayer rupture at slightly similar values of the surface tension, 84 mN m^{-1} and 90 mN m^{-1} respectively, however the bilayer under shear ruptured at approximately 1.8 times its initial area; lower than that for the strain simulation. This suggests that a shear stress is more injurious to a lipid bilayer than in-plane stretching i.e. lipid bilayers rupturing under shear sooner than in tension indicates that the rotating magnetic nanoparticles will require less energy to produce cell membrane rupture.

2.3.4 Comparison with Experimental Results

The small system size and fast loading rate present in our simulations have a large influence on the system. In our simulations we are examining a very small portion of a lipid bilayer, not an entire vesicle or cell. In a laboratory setting, the area expansion and rupture tension are generally measured using a micropipette aspiration technique (94); (95); (96); (97); (98). In these studies the area expansion is rarely greater than 5%. However, this value is relative to the entire vesicle rather than the small portion in contact with the micropipette and is dependent on loading rate (97). Additionally, the micropipette aspiration studies (94); (95); (96); (97); (98) report the surface tension at which rupture occurs on the order of 5-10 times lower than the value reported here. This is also is a result of the applied loading rate in our system which is 7-9 orders of magnitude higher than in experiments. In fact, using the theory of Evans et al. (96) for the dependence of rupture tension on loading rate, we can estimate a theoretical rupture tension for our applied loading rate (1.4 mN m^{-1} ns^{-1}). For the high-loading rate regimen, Evans et al. derive the relation:

$$\sigma / \sigma_{\delta} \approx \ln\left(\Re_{\sigma} / \nu_{0\delta}\sigma_{\delta}\right) \qquad (10)$$

where σ is the tension at rupture, σ_δ is a tension scale for defect formation, $\Re_{\sigma}$ is the loading rate, and $\nu_{0\delta}$ is the frequency for spontaneous nucleation of defects. Using the values of Evans et al. for DOPC (similar to DPPC) where σ_δ = 4.0 mN m^{-1} and $\nu_{0\delta}$ = $0.22s^{-1}$ and a loading rate of 1.4 mN m^{-1} ns^{-1}, the calculated rupture tension is 85 mN m^{-1}, consistent with the 84 mN m^{-1} determined from our simulations. Thus, although in a laboratory setting the area expansion and rupture tension are lower than reported here, these values are highly dependent on the loading rate and the portion of the bilayer being examined. Our results are consistent with experiments, confirming that the value for the surface tension obtained in our simulations is close to 85 mN m^{-1} for a 1.4 mN m^{-1} ns^{-1} loading rate.

2.3.5 Energetics of Membrane Rupture

Using the results of our simulations, we can estimate the energy required to produce rupture in a lipid bilayer. The surface tension, γ, is defined as the amount of energy needed to increase the area of a surface by a value δA. Thus, multiplying the surface tension at which rupture occured by the normalized bilayer area increase results in the energy needed for rupture. In our shearing simulations, $\delta\gamma = 81.2$mN m^{-1} and $\delta A = 32.2$ nm^2 yielding an energy for rupture of 6.3x10^{-2} J m^{-2}. In our simulations, this energy can be thought of as an upper bound. Our system consisted of a bilayer film in a simulation cell with cross-sectional area of ~40 nm^2. As such it was unable to undergo thermal fluctuations and undulations with wavelength larger than the length of the simulation cell. A much larger 3D bilayer on the other hand undergoes periodic long wavelength undulations and fluctuations which could enhance the formation of pore-nucleation sites (110). In our stretching simulations with $\lambda = 1.04$, the energy for rupture was calculated as 7.8x10^{-2} J m^{-2}. We have performed additional simulations with a bilayer half the size (64 lipids) and confirmed that the force increases with decreasing bilayer size (data not shown). Our simulations on the smaller bilayer resulted in an energy for rupture of 1.1x10^{-1} J m^{-2}. This is in accordance with the findings of Marrink and Mark (111) who found that as a result of the size-dependence of the area compressibility modulus, the surface tension of stressed bilayers decreases with increasing system size.

Our calculated value of the energy needed to rupture a lipid bilayer under shear can be compared to the energy imparted on a rotating nanoparticle due to an applied oscillating field. From this comparison, an estimate of the size of magnetic nanoparticles needed to induce membrane rupture could be obtained. When a magnetic nanoparticle with rigidly locked dipole is placed in a magnetic field, it will experience a torque which tends to align the magnetic dipole with the applied field. A torque acting through a rotational distance results in an energy, the magnetostatic energy, given by:

$$E = \mu_0 MVH \tag{11}$$

where μ_0 is the permeability of free space, equal to $4\pi\text{x}10^{-7}$ Wb A^{-1} m^{-1}, M is the domain magnetization, V is the volume, and H is the applied magnetic field. Magnetic nanoparticles commonly used in MFH are generally composed of a magnetite core. Magnetite has a domain magnetization of 430 kA m^{-1} (112). Johannsen et al. 2005 (113) worked with nanoparticles composed of magnetite with an average particle core of 15 nm. The particles were coated with "an aminosilan-type shell". The authors used variable field strengths of 0-18 kA m^{-1}, with the most common field being 12.6 kA m^{-1}. Using Eqn. 11 and our value of the energy, at 18 kA m^{-1} we obtain a particle diameter sufficient to produce mechanical rupture of approximately 80 nm and at 12.6 kA m^{-1} of 90 nm, 5 to 6 times larger than was used in (113). These estimates indicate that it is unlikely that cell death observed in (113) was augmented by mechanical rupture. Still, our estimates indicate that nanoparticles smaller than 100 nm, a widely accepted upper limit for biomedical applications of nanoparticles could induce rupture. Additionally, our simulations present an upper bound on the force of rupture. Considering that the force for rupture is size-dependent, it is beneficial to study the response of a larger bilayer (on the order of 10-20 nm, consistent with the size of nanoparticles used in MFH). Additionally, nanoparticles are often coated with polymers or surfactants for targeting or stability purposes. As such, we performed further simulations of a larger bilayer in response to stress in the presence of a model polymer.

2.4 Poly(ethylene oxide) – Poly(ethyl ethylene) Block Copolymers for the Enhancement of Cell Membrane Rupture Under Stress

Above, we examined the energy necessary to rupture a lipid bilayer under longitudinal tension and shear stress. Here we focus on the influence of molecules used to coat magnetic nanoparticles and their interaction with a lipid bilayer under stress. The particles used in MFH can be made of a variety of materials but are most frequently composed of iron oxide. The particles are generally coated with a bio-active molecule to improve bioavailability, reduce toxicity, prevent agglomeration, target specific cells, etc (114); (115); (116). Typically the coating molecules are polymers such as dextran (117); (118) and PEG (119) which act to increase the circulation time of the magnetic nanoparticles in the system and provide for favorable particle-cell interactions. For our studies, we have selected a model block copolymer poly(ethylene oxide) – poly(ethyl ethylene) (PEO – PEE) of varying length, structure, and concentration and explored its interaction with a lipid bilayer under stress.

We determined a lipid bilayer could withstand approximately 90 mN m^{-1} prior to rupture which could then be compared to the energy of a magnetic nanoparticle rotating in a magnetic field. This analysis yielded magnetic nanoparticles with an 80 nm magnetic core sufficient to induce rupture. These simulations focused solely on the core of the magnetic nanoparticles and did not include any interaction between the molecules coating the magnetic nanoparticles surface. Groot and Rabone (93) focused on the rupture of bilayers under stress but they did not study the effect of polymers. There exist studies on the interaction between lipid bilayers and long-chain polymers (120) and polymer-grafted lipids (121) but none of that work focuses on the response to an externally applied stress. To the best of our knowledge, a systematic study on the effect of polymer properties on a bilayer under stress has not been performed.

Magnetic nanoparticles along with their surface coatings can be on the order of tens of nanometers in size. To study their interaction with lipid bilayers, we thus need a computational method that allows for large system sizes and long time scales. DPD is a mesoscale simulation technique in which several heavy atoms are lumped together to form a single DPD bead. Beads interact with each other through soft potentials allowing for much larger time steps than traditional MD. DPD has been successfully used to study structural properties of lipid bilayers (93); (122); (123) as well as polymer phase separation and polymersome formation (124); (125). Yang and Ma (126) used DPD to study the influence of size and shape of magnetic nanoparticles on penetration through a lipid bilayer. The nature of the DPD technique thus allows computational feasibility for the system sizes and times scales necessary to probe bilayer-polymer interaction under stress. In these simulations we aim to model the interaction of a polymer-coated magnetic nanoparticle exerting a force on a cell membrane resulting from an applied magnetic field. We approximate this by exploring the interaction of a specific polymer with a lipid bilayer under tension. We measured the surface tension and area extension at which bilayer ruptured occurs and calculated the resulting energy needed to rupture the bilayer-polymer composite system.

2.4.1 The Dissipative Particle Dynamics (DPD) Simulation Technique

DPD is a simulation technique introduced by Hoogerbrugge and Koelman (69) and later refined by Español and Warren (127) that allows for the large length and time scales associated with our system. It is a CG technique in which atoms are grouped together into beads of equal diameter. Generally three to four heavy atoms comprise one bead, representative of a specific fluid volume. The particles interact through soft potentials permitting significantly greater time steps than traditional MD simulation. The potential function in DPD consists of bonded interactions (bond stretching and angle bending) between linked atoms of the same molecule and non-bonded interactions between all beads of the system meant to mimic electrostatic and dispersion forces. The non-bonded interaction force between particles is taken as a sum of three terms, a conservative force (F_C), a random force (F_R), and a dissipative force (F_D):

$$\vec{F} = \vec{F}_{ij}^{C} + \vec{F}_{ij}^{R} + \vec{F}_{ij}^{D} \qquad (12)$$

The conservative force has the form shown in Eqn. 13 where $r_{ij} = \|r_{ij}\|$, the distance between beads i and j and R_c the maximum distance between beads for which the non-bonded interactions are calculated. The conservative force is a repulsive force scaled by the mutual repulsive parameter a_{ij} which determines the maximum repulsion at $r_{ij} = 0$. It has been shown that a_{ij} is related to the Flory-Huggins parameter χ through the relation:

$$\chi = (0.231 \pm 0.001)\Delta a_{ij} \tag{13}$$

for the case in which $\rho = 3$ heavy atoms per bead (93), where $\Delta a_{ij} = a_{ij} - a_{ii}$ is the excess *i-j* repulsion over the *i-i* repulsion.

$$\begin{aligned} \vec{F}_{ij}^{C} &= a_{ij}\frac{r_{ij} - R_C}{R_C}\frac{\vec{r}_{ij}}{r_{ij}} \quad && if \quad r_{ij} < R_C \\ \vec{F}_{ij}^{C} &= 0 && if \quad r_{ij} \geq R_C \end{aligned} \tag{14}$$

The random is defined as:

$$\vec{F}_{ij}^{R} = \sigma\,\omega^{R}\theta_{ij}(t)\hat{r}_{ij} \tag{15}$$

where θ_{ij} is a random variable with Gaussian statistics, ω^R is a weighting function, and σ is the strength of the random force for which, following Groot and Warren (128) we chose $\sigma = 3$ to achieve proper temperature control. The dissipative force is a drag force that is related to the relative velocities (v_{ij}) between two beads:

$$\vec{F}_{ij}^{D} = -\gamma\,\omega^{D}\left(\vec{r}_{ij} \cdot \vec{v}_{ij}\right)\hat{r}_{ij}$$

(16)

where ω^D is a weighting function and γ is the magnitude of the drag coefficient. Español and Warren (127) showed that the dissipative force and the random force are related through the fluctuation-dissipation theorem, which states that $\sigma^2 = 2\gamma k_B T$ and $\omega^D = [\omega^R]^2$. This has been shown to result in a thermostat that conserves angular momentum and thus produces correct hydrodynamic behavior at long length and time scales. As per the original paper of Hoogerbrugge and Koelman (69), we chose the weighting function $\omega^R = 2(1 - r_{ij}/R_c)$ for $r_{ij} < R_C$ and 0 for $r_{ij} \geq R_C$. A bead of density = 3 (3 heavy atoms per bead) results in a value of R_C = 0.64633 nm. In addition to the non-bonded potential, we also included harmonic bond stretching and angle bending potentials given in Eqn. 17 and Eqn. 18 respectively:

$$U_{bond} = \frac{1}{2} k_b \left(r_{ij} - r_0 \right)^2 \tag{17}$$

$$U_{angle} = \frac{1}{2} k_\theta \left(\theta_{ijk} - \theta_0 \right)^2 \tag{18}$$

where the k_b and k_θ are the force constants of the harmonic potentials for the corresponding bond and angle terms. r_{ij} and r_0 are the computed and equilibrium distance between beads *i* and *j* with the equivalent holding for bead triplets *i*, *j*, *k* of the angle potential in Eqn. 18.

Our system was composed of water, a bilayer of DPPC lipids, and PEO-PEE block copolymers, all of which are coarse-grained into DPD beads. The nomenclature for the bead types are as follows (See Fig. 13). Bead 1 corresponds to the lipid head beads. Bead 2 represents the ethylene glycol linkage of the DPPC lipids, and bead 3 represents the hydrocarbon lipid tail. Bead 4 represents three water molecules while beads 5 and 6 correspond to the PEO and PEE portions of the polymer respectively. In our simulations we used a bilayer comprised of 1155 lipids and polymers of varying length, concentration, and block structure. The system prior to perturbation consisted of a 19.2 nm x 19.2 nm bilayer with the size varying slightly depending on the amount and nature of polymer present in the system.

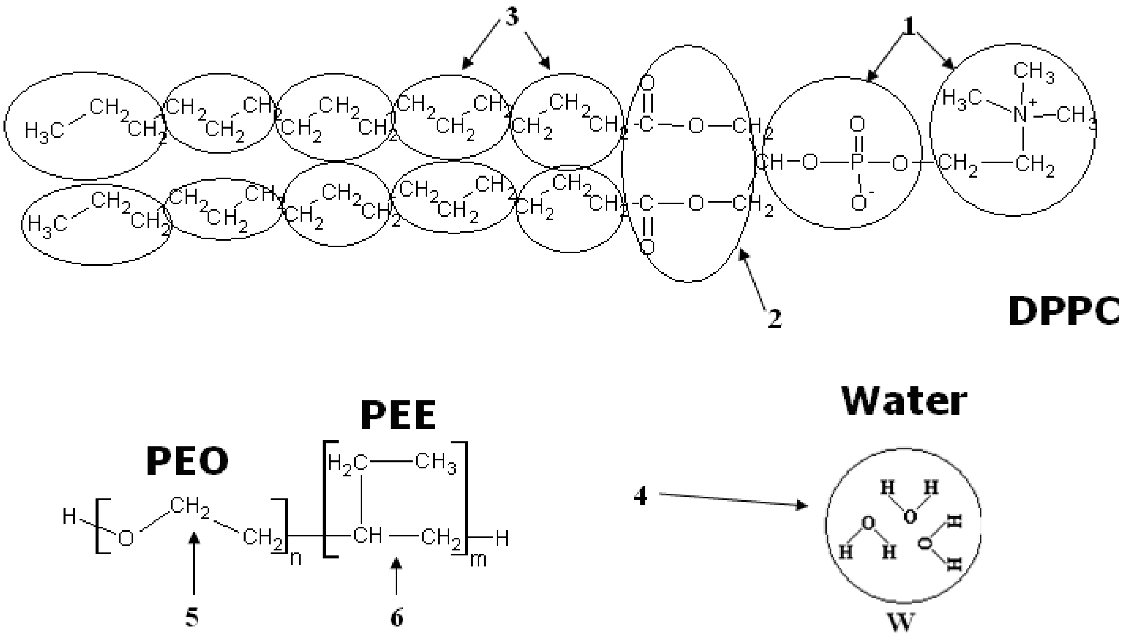

Figure 13: Schematic showing the CG scheme of the lipid-polymer-water system. Bead type 1 includes the charged lipid head beads. Bead type 2 represents the ethylene glycol linkage of the DPPC lipids, and bead type 3 corresponds to the hydrocarbon lipid tail. Bead type 4 represents three water molecules while bead types 5 and 6 correspond to the PEO and PEE portions of the polymer respectively.

Table 1: Bead – Bead interactions for the polymer-bilayer-water system (a_{ij} in Eqn. 14). Parameters are taken from (a) Groot and Rabone (93) and (b) Ortiz et al. (125) and calculated from (c) Tian and Munk (129).

a_{ij}	**1**	**2**	**3**	**4**	**5**	**6**
1	86.7[a]	79.3[a]	104.0[a]	75.8[a]	79.3[a]	104.0
2		78.0[a]	86.7[a]	79.3[a]	78.0[a]	86.7[a]
3			78.0[a]	104.0[a]	86.7[a]	80.4[c]
4				78.0[a]	79.3[b]	100.0[b]
5					78.0[b]	86.7[b]
6						78.0[b]

2.4.2 System Parameterization

In DPD the main tunable parameter governing the interactions in the system is the maximum repulsion (a_{ij}) of the conservative force, which must be determined for each pair of interacting beads. Groot and Rabone (93) and Sugii et al. (130) successfully used parameters for a DPPC lipid bilayer, and Ortiz et al. (125) derived parameters for PEO-PEE block copolymer using a density mapping of one PEO bead corresponding to 1.392 monomers of PEO and one bead of PEE corresponding to 0.774 monomers of PEE. We have used these parameters in our system, and they are displayed in Table 1. The parameters corresponding to the interaction between the polymer beads and the lipid beads were derived in the following manner: the structure of the glycerol linkage portion of the lipids is chemically similar to poly(ethylene oxide). As prior mappings (93) have considered the glycerol linkage (bead 2) equivalent to 1.5 ethylene oxide groups and in our polymer mapping scheme bead 5 consists of 1.4 monomers of PEO, these groups should be very similar. Therefore, we have taken the interactions of bead 5 with the other beads in the system equivalent to those of bead 2. Some initial tests were done with small variations of this parameter, and no significant changes were found in system properties as revealed by the polymer and the solvent radial distribution functions. The interaction between beads 3 and 6 was taken from the experimental χ-parameter for the mixing of propane and PEE of Tian and Munk (129). Their experimental data corresponds to mixing temperatures higher than our target temperature and thus the data was extrapolated to 300 K using a linear fit. The interaction of bead 6 (PEE) with bead 1 (DPPC lipid head groups) was taken as the most repulsive in the system due to the fact that bead 1 represents a highly polar, charged group and bead 6 represents hydrophobic PEE, (the interaction of lipid hydrocarbon tails with water; bead 3 – bead 4). Table 1 gives the bead-bead interaction parameters (a_{ij}) from Eqn. 13 for the entire system, where i and j are the types of interacting beads. The nomenclature for the beads are as stated in Section 2.4.1 with the lipids represented by beads type 1, 2 and 3, water is represented by bead type 4, and polymer is comprised of beads type 5 and type 6 (Fig. 13). All bond and angle interactions were described using the parameters of Kranenburg et al. (122) for the lipids and Ortiz et al. (125) for the polymers. Tables 2 and 3 display the bond and angle parameters respectively.

Table 2: Bonded interactions for a harmonic bonded potential of Eqn. 17. Interaction terms are described in the text. Parameters are taken from (a) Kranenberg et al. (122) and (b) Ortiz et al. (125).

Interaction	K_b (k_BT / Rc^2)	r_0 (Rc)
1 – 1	100.0^a	0.70^a
1 – 2	100.0^a	0.70^a
2 – 3	100.0^a	0.70^a
3 – 3	100.0^a	0.70^a
5 – 5	1107.51^b	0.5573^b
5 – 6	566.84^b	0.6469^b
6 – 6	160.93^b	0.5998^b

Table 3: Bond angle interactions for a harmonic angle potential of Eqn. 18. Interaction terms are described in the text. Parameters are taken from (a) Kranenberg et al. (122) and (b) Ortiz et al. (125).

Interaction	K_θ (k_BT / rad^2)	θ_0 (Deg)
3 – 2 – 3	100.0^a	90.0^a
3 – 3 – 3	100.0^a	180.0^a
5 – 5 – 5	4.03^b	122.1^b
5 – 5 – 6	4.96^b	145.5^b
5 – 6 – 6	13.48^b	97.8^b
6 – 6 – 6	10.19^b	102.2^b

2.4.3 Simulation Details

The validity of our DPD code was confirmed by reproducing data from both Groot and Rabone (93) on lipids in water and Ortiz et al. (125) on polymersomes of PEO-PEE in water. To determine the adequacy of the lipid-polymer parameterization, simulations were performed on the interaction of PEO-PEE polymer with a DPPC bilayer and results were compared with those of Srinivas and Klein (120), who studied this interaction using a CG MD model on a bilayer of 184 lipids and varying concentrations of polymer, in the absence of stress. The parameters were tested to elucidate the influence of polymer concentration on the lipid head density as well as the distribution of PEO from the bilayer surface.

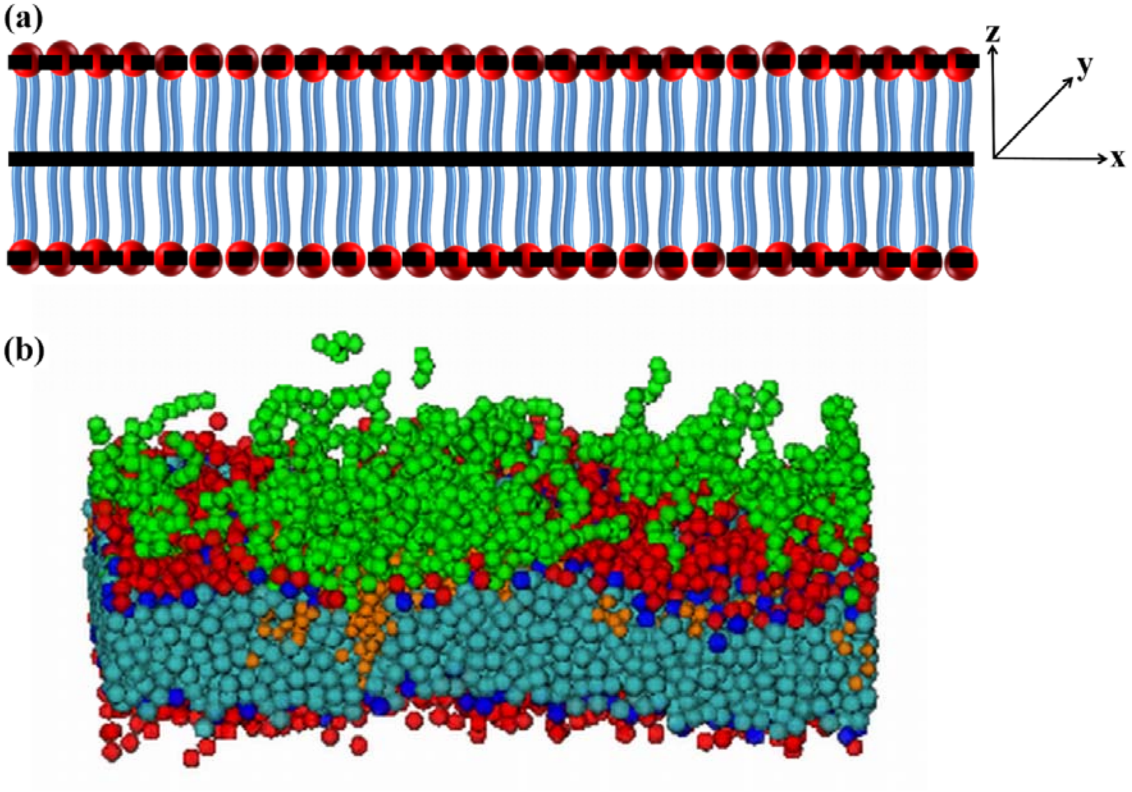

Figure 14: **(a)** Schematic representation of the bilayer system. The dashed lines correspond to the two bilayer surfaces and the solid line corresponds to the bilayer center. **(b)** Initial configuration prior to rupture simulations showing polymer insertion into the bilayer. Bead 1 = red, Bead 2 = dark blue, Bead 3 = cyan, Bead 5 = green, Bead 6 = orange, water beads (Bead 4) are omitted for clarity (description of bead numbering is given in the text).

Initial configurations for the system containing bilayer, polymer, and water were obtained in the following manner: lipid molecules were placed in a large water box and simulated until bilayer self-assembly was observed. With a stable bilayer-water system, polymer was added to one face of the bilayer and allowed to equilibrate until the hydrophobic (PEE) portions of the polymers inserted themselves into the hydrophobic core of the bilayer. A snapshot of the equilibrated system is shown in Fig. 14. To determine the amount of stress required to rupture a bilayer in the presence of polymer it was necessary to begin our simulations in a stress-free state, which was established by computing the area corresponding to the state of zero surface tension. This was calculated by performing simulations for each system at five different bilayer areas while measuring the surface tension, γ, according to Eqn. 7. The results from the simulations to obtain a stress-free state are shown in Fig. 15. A linear fit was applied to the surface tension vs. area data where the intersection of the fit line with the x-axis corresponds to the zero surface tension state.

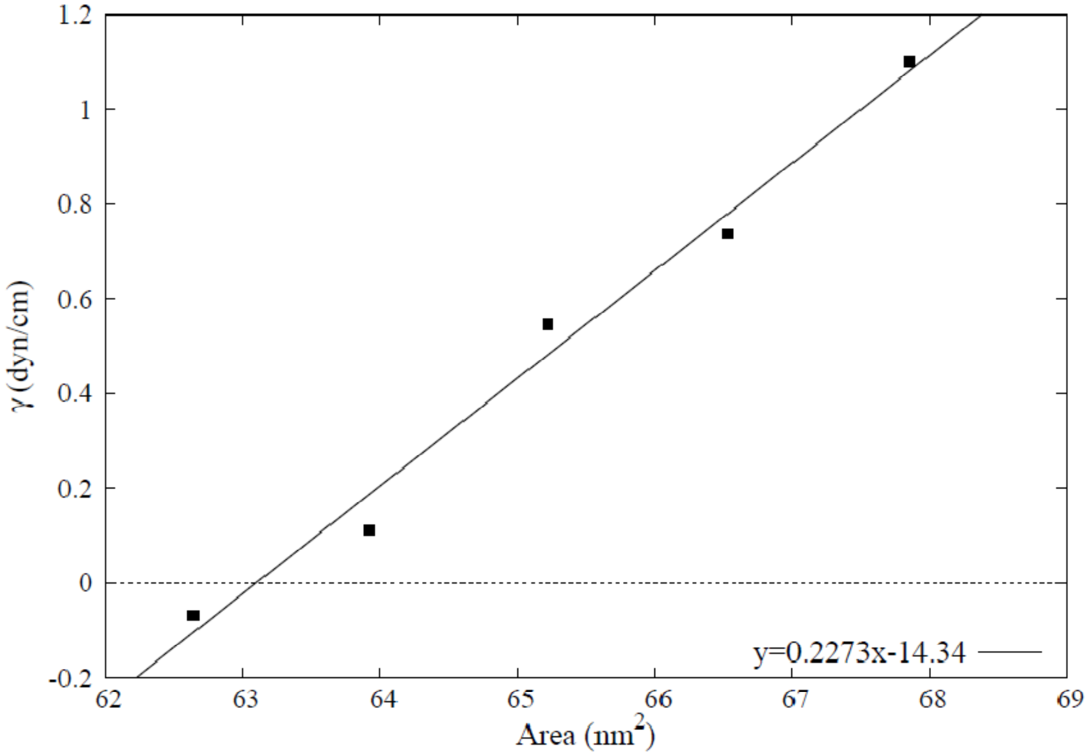

Figure 15: Surface tension of the bilayer versus area. For each case, 5 simulations at different bilayer areas were performed and the surface tension as a function of area was fit to the data by linear regression. The fit was used to interpolate the area of the bilayer corresponding to a tensionless state. The equation of best fit is given on the graph, $R^2 = 0.985$.

Rupture simulations were performed by applying an incremental tension to the system similar to those described above. The x- and y-coordinates of all beads were multiplied by a stretch-factor of λ while the z-coordinates were divided by a stretch-factor of λ^2. A stretch was applied instantaneously followed by an NVT relaxation period for 50,000 steps. We considered two different values of the stretch factor: λ = 1.03 and λ = 1.04. During the relaxation period we obtained an average measure of the surface tension calculated from the final 25,000 steps of relaxation. Each transformation was performed several times until a sharp drop in the surface tension was observed indicating rupture of the bilayer.

Because the unit of time in CG DPD simulations can be somewhat ambiguous, we performed water diffusion measurements to determine the equivalent length of the time step. Three separate trials of a system containing only water beads were run for 50,000 steps and we calculated the water MSD according to Eqn. 8. Relating the long-time MSD to the experimental diffusion coefficient of water, we found one DPD time step equal to 1.49 ps, or each stretch-relaxation iteration equaling 74.5 ns.

2.4.4 System Validation

We validated the interaction parameters in our DPD system by replicating results of Srinivas and Klein (120) for the interaction of PEO_{19}-PEE_9 polymers with a dimyristoylphosphatidylcholine (DMPC) bilayer in the absence of stress. The initial setup of our system consisted of a bilayer comprised of 184 DPPC lipids (7.8 nm x 7.8 nm) to which polymer was added to one face in varying concentrations from 0 wt.% to 33 wt.%. In accordance with the CG mapping scheme described in section 2.4.1, the PEO_{19}-PEE_9 polymers of Srinivas and Klein (120) correspond to PEO_{14}-PEE_{12} in our system. The results of our DPD simulation are given in Figs. 16 and 17.

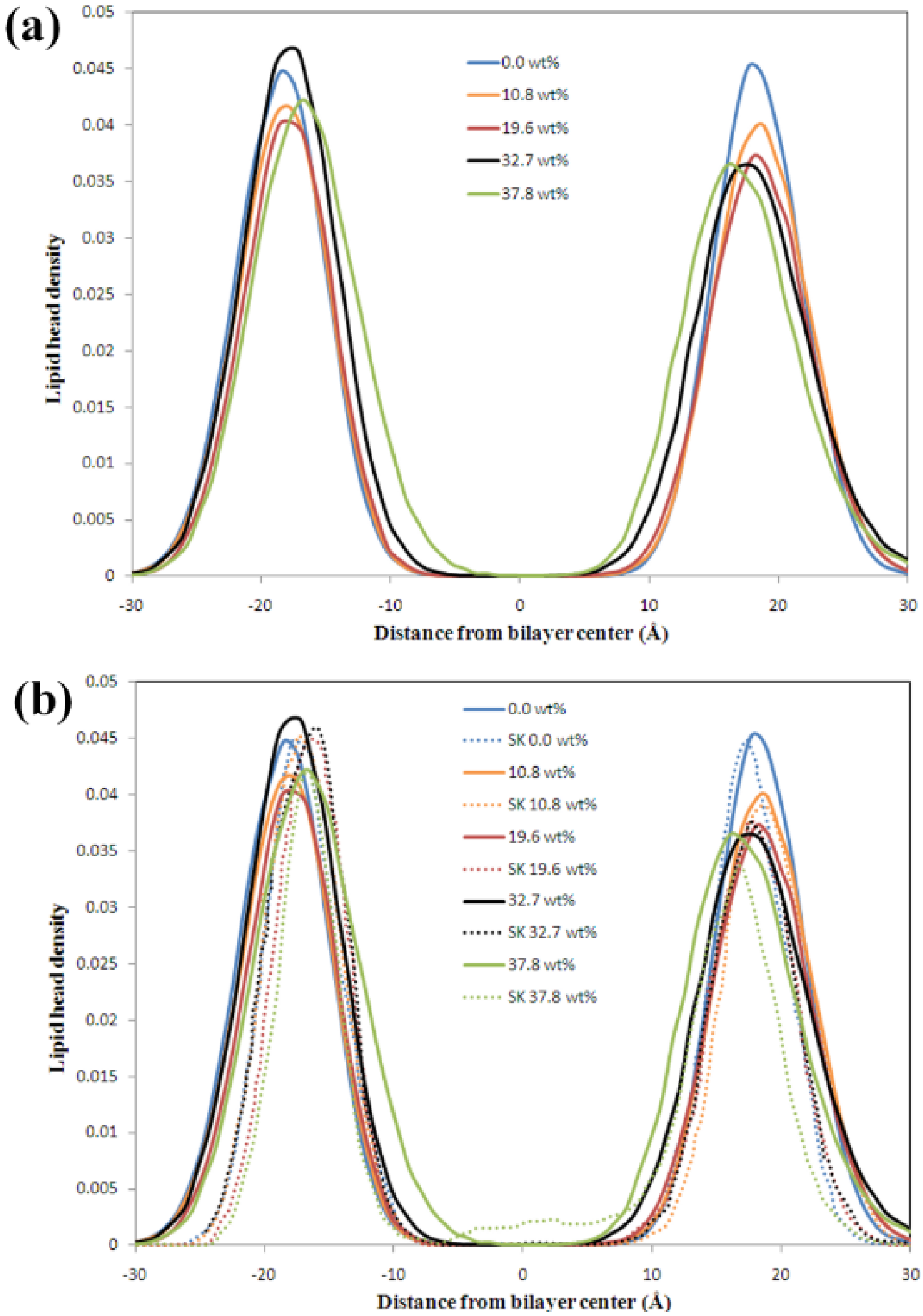

Figure 16: (a) Lipid head density across the bilayer. The negative distances from the bilayer center indicate the bilayer leaflet in the absence of polymer whereas positive distances correspond to varying wt.% of polymer associating with the bilayer. **(b)** The results of this work (solid lines) with the number density (y-axis) scaled to match that of (120) (dashed lines). No scaling was applied to the x-axis.

Figure 16 shows the lipid head density of both bilayer faces, one face with and the other without polymer, as a function of polymer concentration (solvent excluded in the concentration calculation). Polymer acted to decrease the lipid head density in the monolayer subjected to polymer (positive distances from the bilayer center) compared to the face without polymer (negative distances from bilayer center). We found this to be in qualitative agreement with Srinivas and Klein (120); however there were quantitative differences between the two studies, which are a consequence of using a different computational model (DPD compared to CG MD) and lipids with different length tails (14 for DPPC vs. 12 for DMPC). The results of this work, with the number density (y-axis) scaled to match that of Srinivas and Klein (120) is shown in Fig. 16b. No scaling was applied to the x-axis. Figure 17 is the density distribution of the hydrophilic (PEO beads) away from the surface of the bilayer (+z-direction). Similarly to Fig. 16, we found good agreement with the results of Srinivas and Klein (120), with a scaled comparison given in Fig. 17b. Increasing polymer concentration yielded an increase in the distance of PEO from the bilayer surface. The spreading of PEO with increasing concentration was consistent with de Gennes (131) which showed the transition from a mushroom (hemispherical) conformation to a brush (extended) conformation as the polymer concentration was increased. Quantitative differences between our results and those of Srinivas and Klein (120) were due to the aforementioned reasons from Fig. 16.

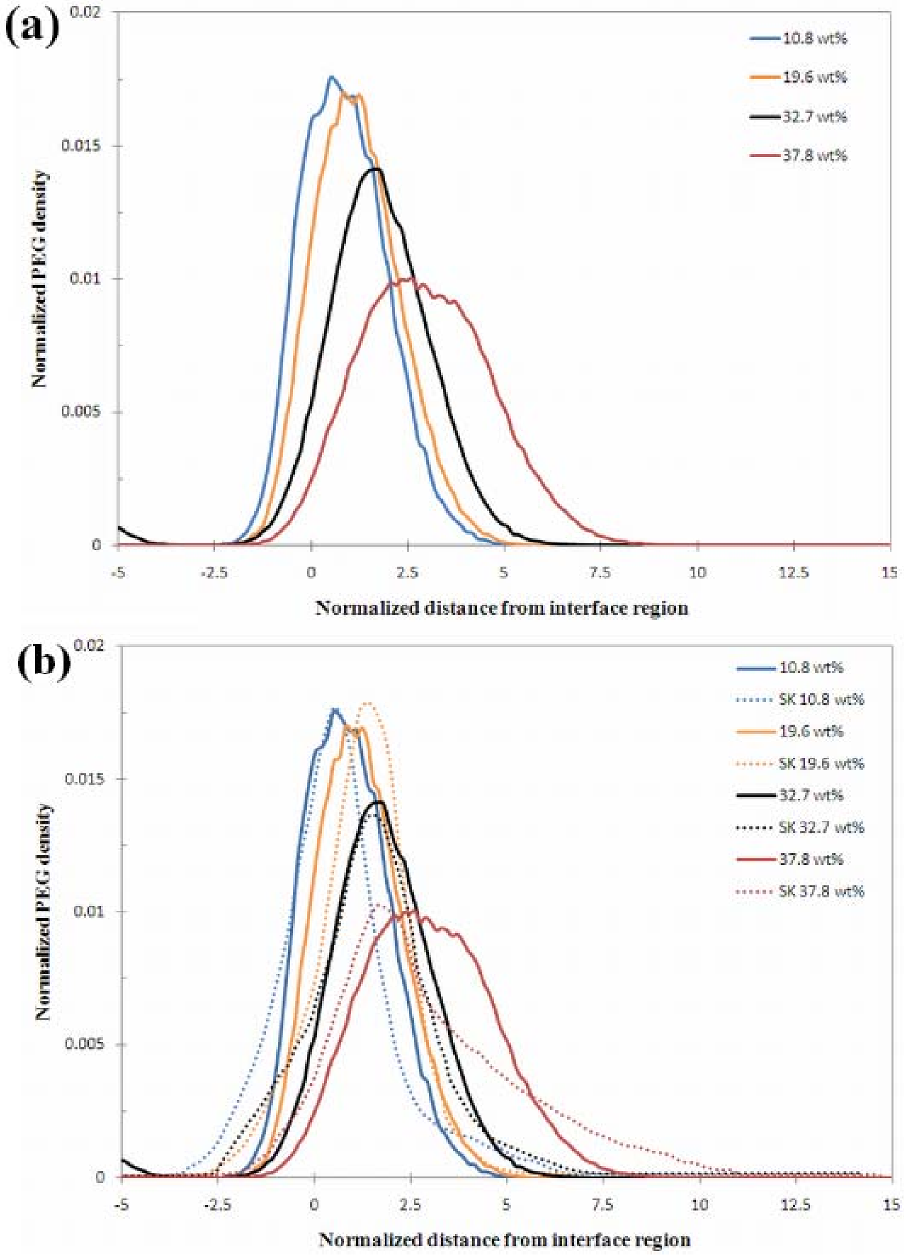

Figure 17: **(a)** Distribution of PEO beads from the bilayer surface. Increasing the concentration of polymer distributes the PEO monomers further from the bilayer surface. **(b)** The results of this work (solid lines) with the number density (y-axis) scaled to match that of (120) (dashed lines). No scaling was applied to the x-axis.

2.5 Effect of Polymer Concentration on Bilayer Rupture

For rupture simulations we considered a bilayer of 1155 lipids. The polymers consisted of PEO$_x$-PEE$_y$ in an AB block structure where x and y refer to the CG number of beads rather than the number of monomer units (section 2.4.2). Polymer was added to the system at different concentrations: 0 wt.% to 30.2 wt.% and equilibrated until the hydrophobic portion (PEE beads) inserted themselves into the bilayer. Following equilibration, we stretched the bilayer area incrementally in discrete values until rupture occurred. A sample snapshot showing rupture is shown in Fig. 18. The results are shown in Fig. 19. For a fixed surface tension, increasing the concentration of polymer in the system increased the compliance of the bilayer, allowing it to be stretched further. This can be visualized by the dashed line in Fig. 19. At 28 dynes/cm of tension, the curves with successively larger polymer concentrations are shifted to the right (larger area extension). We also observed that for a fixed area extension, the higher the polymer concentration, the lower was the surface tension for which the bilayer ruptured. This is obvious for the different discrete cases of bilayer area extension we generated. For example, the cases with 14.8 – 23.3 wt.% polymer the bilayers reached their peak surface tension at an area extension of $\Delta A/A_0 = 0.37$. When stretched to the next increment ($\Delta A/A_0 = 0.48$) these bilayers showed a marked decrease in the surface tension showing rupture and indicating that $\Delta A/A_0 = 0.37$ is the maximum area extension that a bilayer with less than 23.3 wt% polymer can withstand. Further increasing the concentration of polymer in the bilayer (25.7 – 30.2 wt.%) allowed the bilayers to be stretched to the next increment, $\Delta A/A_0 = 0.48$ prior to rupture.

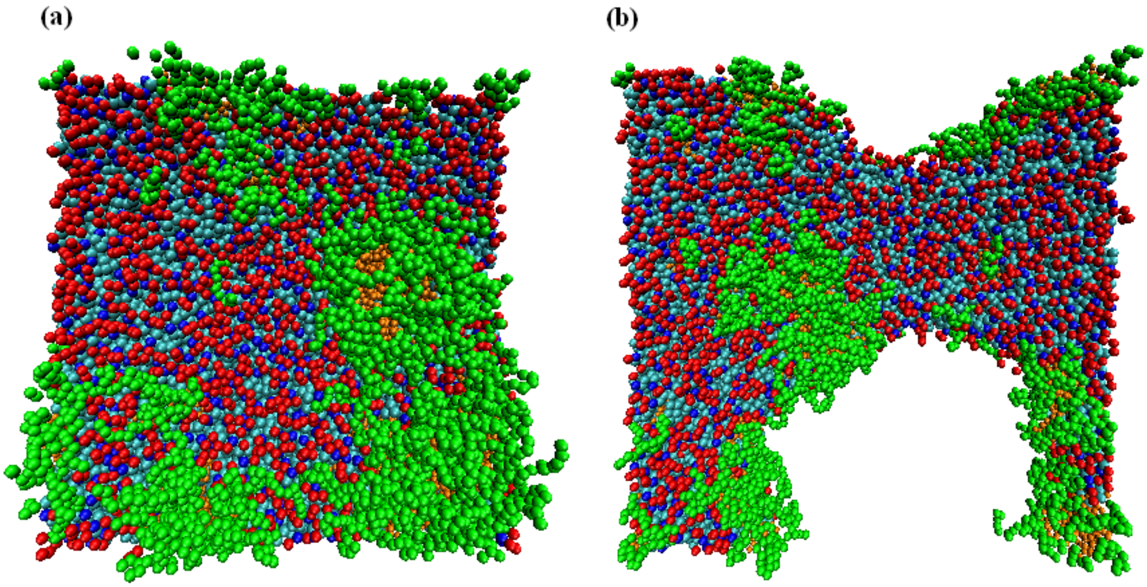

Figure 18: Snapshots of membrane rupture with 20.6 wt.% polymer. **(a)** Following equilibration and **(b)** Bilayer rupture following 6 stretch increments.

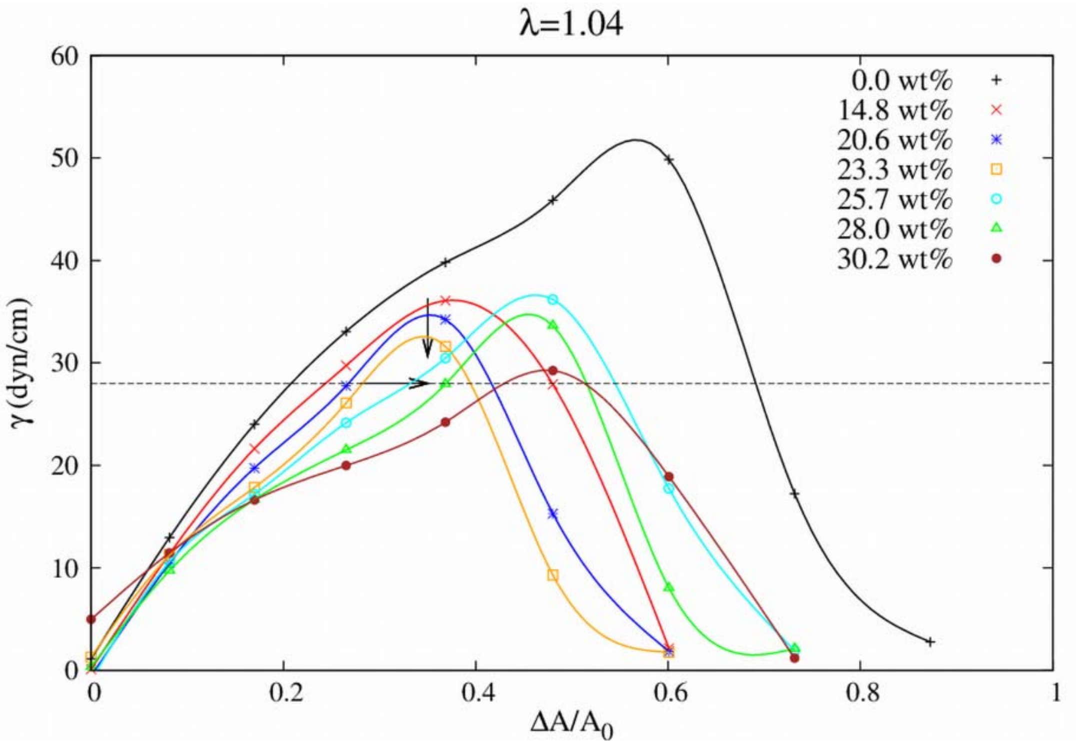

Figure 19: The response of polymer concentration on bilayer rupture for 5 different polymer concentrations. The polymers used in this simulation were 26-mers, 14 monomers of PEO and 12 monomers of PEE in an AB block structure.

2.5.1 Effect of Polymer Length on Bilayer Rupture

Figure 20 shows the effect of polymer length on bilayer rupture. Results from Figs. 19 and 20 were both obtained using a constant hydrophilic to hydrophobic ratio of 68%, but the lengths in Fig. 20 are extended either to 61 (PEO_{33}-PEE_{28}) monomers or 100 (PEO_{54}-PEE_{46}) monomers at two different concentrations, 100 or 200 polymers. The results show that at a fixed concentration (either 100 or 200 polymers) increasing the polymer length resulted in a larger change in the maximum area extension prior to rupture than in the maximum surface tension. Increasing the polymer length from 61 monomers to 100 monomers at a concentration of 200 polymer molecules (44.8 wt% for 61 monomers and 49.9 wt% for 100 monomers) the maximum surface tension increased by 9.7% while the area extension prior to rupture increased by 40%. For 100 polymers, increasing the polymer length caused the maximum surface tension to decrease by 2.8% while the area expansion increased by 22%. Thus, increasing polymer length did little to alter the surface tension at which the bilayer ruptured (slight decrease at 100 polymers and slight increase at 200 polymers), but greatly increased the amount that the bilayer could expand prior to rupture (22% and 40% increase for 100 polymers and 200 polymers respectively). An effect similar to this is seen in grafted polymers in that steric interactions of the polymer extending from the bilayer surface induce a lateral pressure which facilitates area expansion, the effect increasing with increasing polymer length (132).

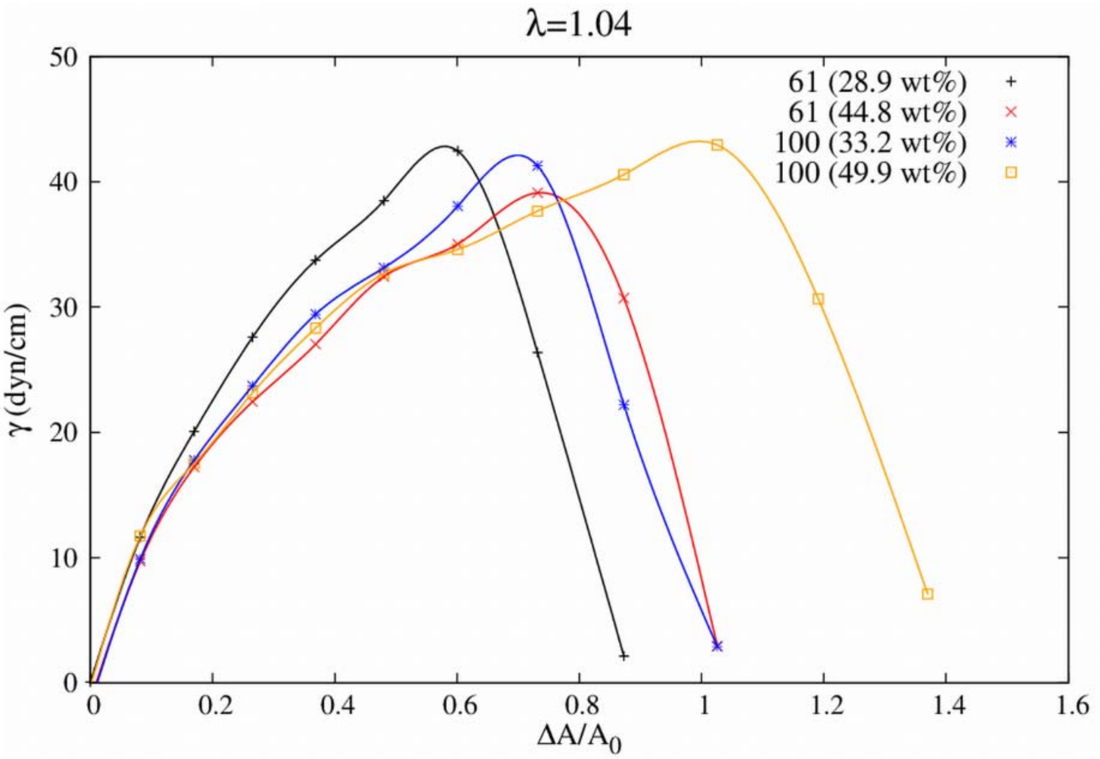

Figure 20: The response of polymer length on bilayer rupture for 2 different polymer lengths (61 monomers and 100 monomers) at 2 different concentrations, either 100 or 200 polymers in the system. The polymers used in this simulation contained the same hydrophilic to hydrophobic ratio and block structure as the polymers listed in Fig. 16.

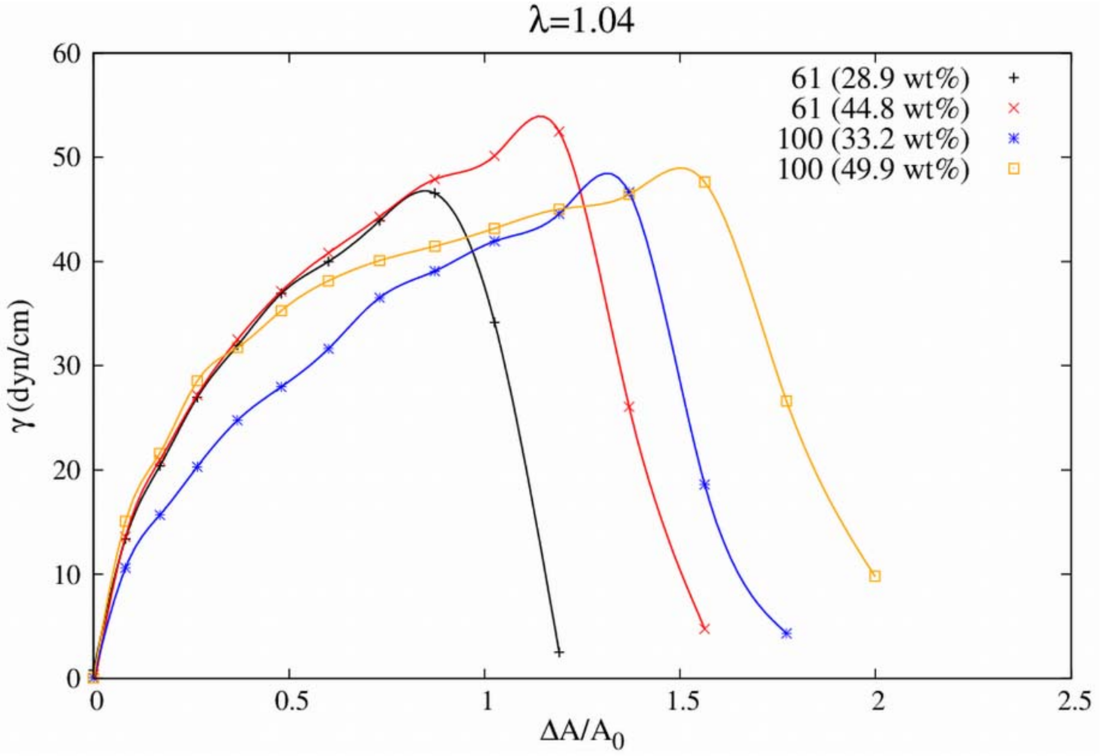

Figure 21: The result of increasing the polymer hydrophobic content. The polymers used in this simulation have the same properties as the polymers listed in Fig. 16 except the hydrophilic to hydrophobic ratio has been decreased from 68% to 35%.

2.5.2 Effect of Polymer Hydrophilic to Hydrophobic Ratio

To test the effect of relative hydrophobicity on bilayer rupture, we varied the ratio of hydrophilic to hydrophobic monomers in the polymer. Figure 21 shows the rupture results when the hydrophilic ratio of the polymers was decreased to 35% (PEO_{14}-PEE_{47} or PEO_{23}-PEE_{77}) while maintaining the same lengths and concentrations used in Fig. 20. Figure 22 shows the results of Fig. 21 (filled markers) overlain with those of Fig. 20 (open markers) for comparison. In all cases, increasing the hydrophobic content of the polymer increased the maximum surface tension by an average of 16.7% as well as expanded the area expansion prior to rupture by an average of 61.9%. This increased bilayer area expansion was the result of enhanced penetration of the PEE portion of the polymer into the hydrophobic interior of the bilayer as can be seen in the system snapshot shown in Fig. 23a of the bilayer system just prior to rupture. One can see that the bilayer had numerous discontinuities associated with its structure, but the hydrophobic (PEE) portion of the polymer filled in the pores that formed in the bilayer, maintaining a continuous structure. A snapshot of the bilayer following rupture is shown in Fig. 23b.

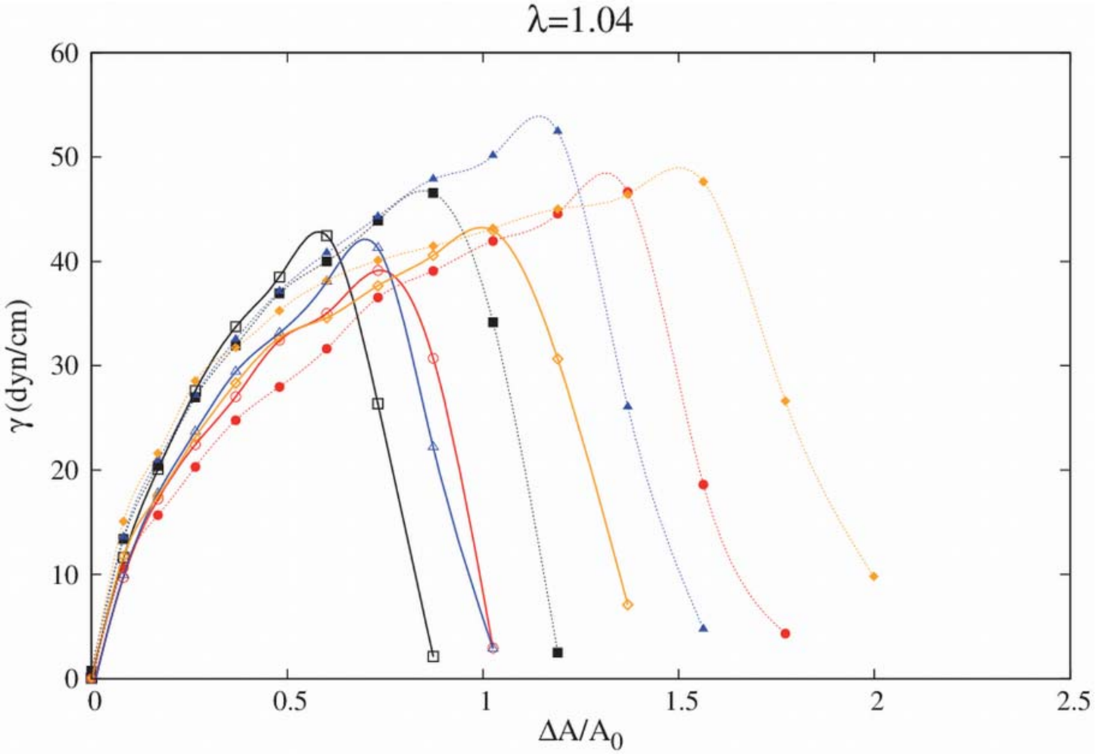

Figure 22: The response of the polymer hydrophobic content on bilayer rupture. The data is the same as that shown in Figs. 17 and 19. The dashed lines and open markers correspond to the data from Fig. 17 while the solid lines and filled markers correspond to data from Fig. 19.

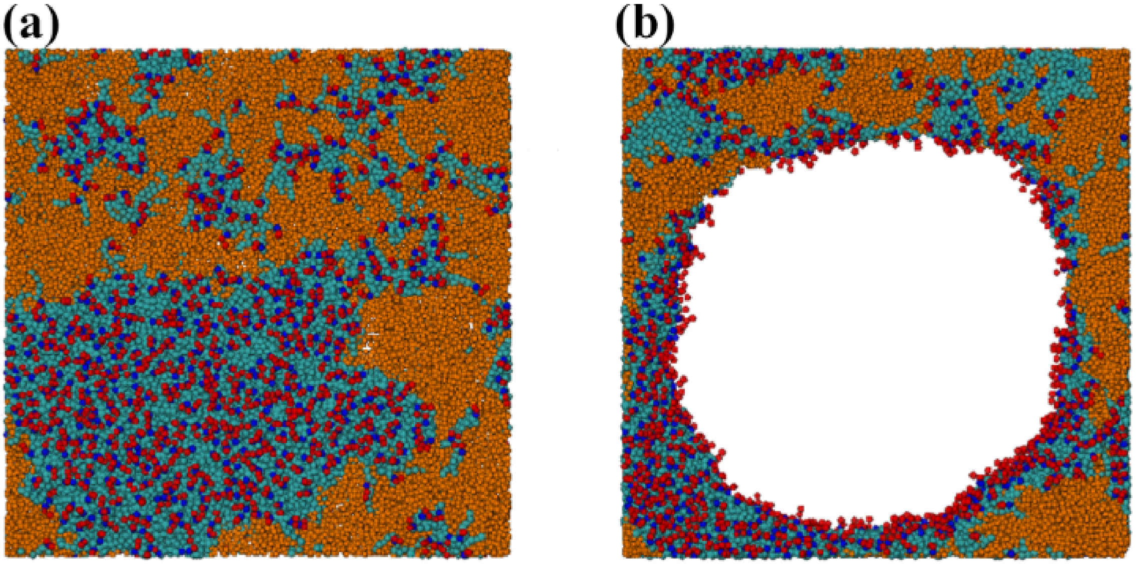

Figure 23: Snapshot of the polymer system with 35% hydrophilic ratio. Water beads and hydrophilic (PEO) polymer beads are omitted for clarity. Orange beads represent PEE (bead 6) while the other beads correspond to the bilayer. (a) The bilayer just prior to rupture. (b) The bilayer following rupture.

2.5.3 Effect of Polymer Block Structure on Bilayer Rupture

Finally, we examined the influence of polymer block structure on bilayer rupture. The previous simulations contained polymers where one section of the polymer was composed of PEO and the other section composed of PEE for an AB block structure with A and B corresponding to PEO and PEE respectively. Figure 24 shows the results of varying the structure of the polymer where we examined both ABA and BAB tri-block copolymers. This figure can be compared with Fig. 19 (simulations with an AB block structure). Polymers with an ABA block structure ruptured at the same area extension and slightly lower surface tension than the polymers with an AB block structure. The polymers with a BAB block structure (PEE-PEO-PEE) ruptured at a markedly lower surface tension and area extension than either the AB polymers or the ABA polymers indicating that BAB polymers would be better for enhancing bilayer rupture.

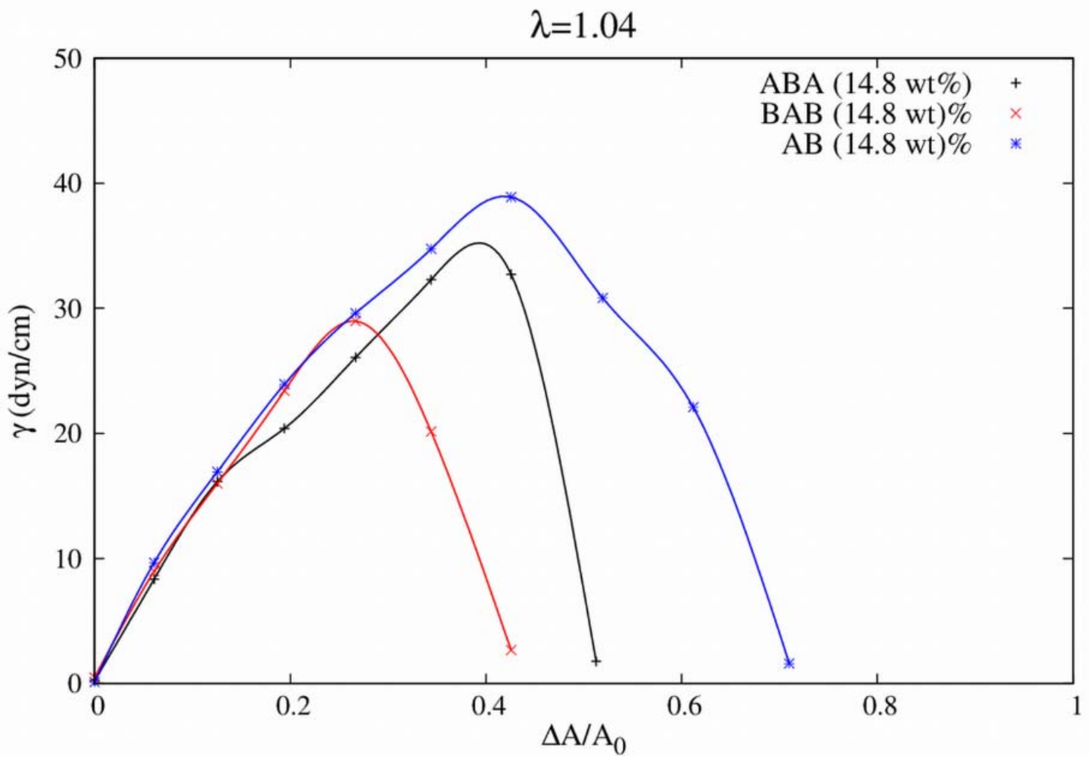

Figure 24: The response of polymer block structure on bilayer rupture. The result for polymers with an AB block structure from Fig. 15 is included for comparison.

2.5.4 Energetics of Membrane Rupture and Comparison with Experiment

The concentration simulations showed that the increasing the concentration of polymer in the system caused the bilayer to become more compliant, allowing it to be stretched further at a given tension. This is a result of the polymer acting to stabilize the small defects that form as the bilayer is pulled. Increasing polymer concentration also reduced the surface tension of the bilayer at a given area extension. Increasing polymer length did not change the maximum tension that a bilayer could withstand prior to rupture but increased its area extension adding to the bilayer strength. Thus, for rupture enhancement, shorter polymers appear to be more effective. Polymer hydrophobicity and block structure had the greatest influence on bilayer rupture with highly hydrophilic polymers in a BAB block structure yielding the weakest bilayers. Hydrophilic polymers extending away from the bilayer surface encounter steric interactions with each other which cause the lateral pressure in the bilayer to increase, yielding an increased area expansion prior to rupture. To combine the effects of surface tension and area extension, we looked at the overall energy it took to rupture the bilayer in the presence of polymers with varying properties in the same manner as above (section 2.3.5). The rupture energies for the different systems are summarized in Fig. 25. Using our lowest rupture energy of 0.9×10^{-2} J m^{-2} and a magnetic field of 12.6 kA m^{-1} we obtain the diameter of a magnetic nanoparticle required to generate such energy equal to 50 nm. This is larger than the magnetic core of the magnetic nanoparticles used specifically in (113) but smaller than we found in the absence of polymer in the system and well within the hydrodynamic diameter of particles used in many studies in the literature.

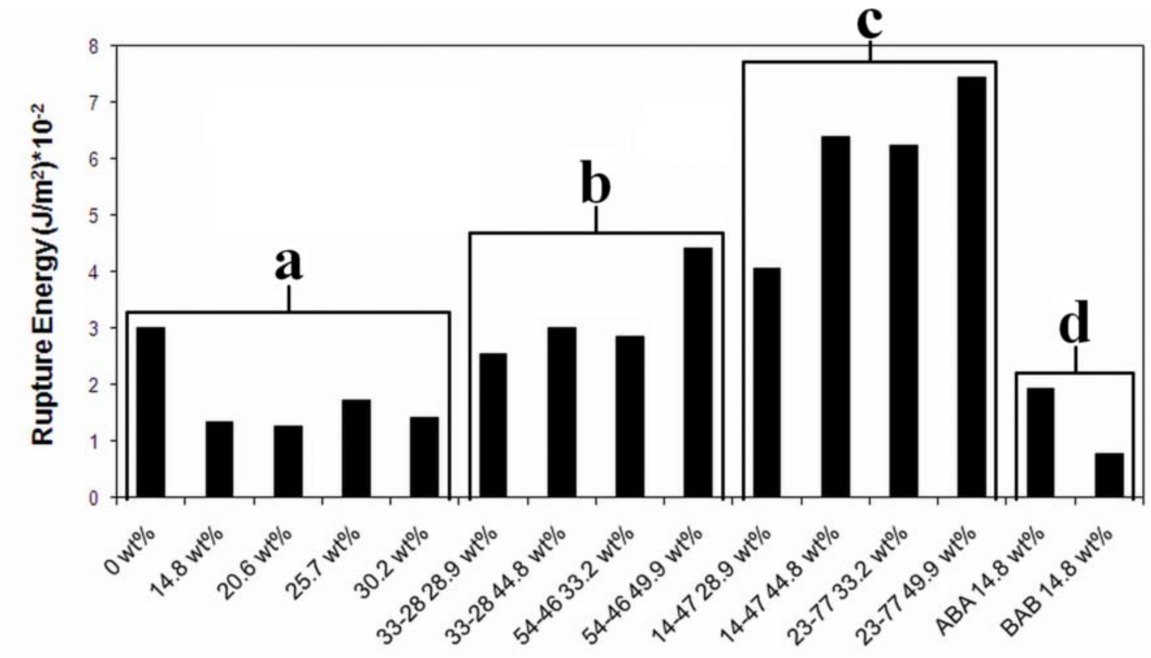

Figure 25: Rupture energies for the different bilayer-polymer systems: a) polymer concentration, b) polymer length, c) polymer hydrophilicity, and d) polymer block structure.

2.6 Conclusions of Simulation Studies of a Lipid Bilayer under Stress

We have modeled two plausible mechanisms which may lead to cell membrane rupture during MFH (tension and shear) with the goal of estimating the energies needed to produce rupture of the lipid bilayer and relating these to particle size. Our simulations of membrane rupture via incremental shear stress yielded a value for the surface tension of the bilayer equal to 80–90 mN m^{-1}, with energy for rupture of 6.3x10^{-2} J m^{-2}. These results are consistent with previous results obtained for similar systems in the literature (93). Under conditions representative of experimental MFH studies, the estimated energy required to produce rupture obtained from our simulations yielded a required nanoparticle diameter of 80 nm. This is 5 to 10 times larger than typical particle diameters used in MFH. However, a particle size of 80 nm is plausible for biomedical applications, in which the widely accepted upper limit is between 100 and 200 nm. We also note that these estimates are based on the value of the energy required to rupture a lipid bilayer of approximately 36 nm^2. This energy can be considered an upper bound, since at the nanoscale size (40 nm^2) the bilayer is more stable resulting from reduced thermal fluctuations as compared to a real bilayer, therefore the force and the energy necessary to rupture real cells *in vivo* might be lower.

In addition the atomistic simulations of bilayer rupture we also examined the properties of polymeric coatings of magnetic nanoparticles and their influence on the rupture in the frame of MFH. We simulated a generic polymer (PEO-PEE) and the influence of its properties on enhancing rupture of a lipid bilayer under stress. We found that polymers that enhance rupture are shorter with a hydrophobic-hydrophilic-hydrophobic block structure and a high hydrophilic content. In performing our analysis, we determined that the rupture energies obtained here provide good agreement with the size of magnetic nanoparticles generally used in MFH. This indicates that it is likely magnetic nanoparticles are capable of enhancing rupture of a cell membrane, and choice selection of the magnetic nanoparticle coating properties could result in more effective MFH treatment at reduced, less harmful magnetic fields.

Further research into this area would involve increasing the complexity of the system to better model a realistic natural environment. Cell membranes are much more complicated than the simple lipid bilayer system simulated here. For example, cellular membranes *in vivo* contain a significant amount of cholesterol which acts to order the lipids resulting in a more solid-like membrane. Similarly, cellular membranes also contain several types of lipids, which could act as nucleating points for pore formation. Finally, the addition of ions to the system to simulate the chemical and electrical potential gradient that is present across all cells would be of benefit, for it is the loss of an ion gradient that will ultimately lead to the death of a cell.

Chapter 3 Engineered Macromolecules as Inhibitors to Oxidized Low Density Lipoprotein by Macrophage Scavenger Receptors: Simulation of Structure – Function Relationships

Atherosclerosis is a condition resulting from the accumulation oxidized low-density lipoproteins (LDL) in arterial walls. Recently, engineered macromolecules have been developed to mitigate uptake of oxidized LDL by macrophage scavenger receptors. In this chapter, we utilize Coarse-Grained Molecular Dynamics to study engineered, micelle-forming, amphiphilic macromolecules interacting with human scavenger receptor A for use in the prevention of oxidized LDL uptake as a means to prevent and treat atherosclerosis. The focus is on the structural and electrostatic properties of the macromolecules (charge and charge location) to determine optimal interaction with Scavenger Receptor A and to establish if micellization is a necessary property for successful blocking to occur.

3.1 Pathology of Atherosclerosis

Atherosclerosis is characterized by the buildup of lipid-rich plaques in arterial walls which lead to cardiovascular disease, a leading cause of death in the United States (133). Generally, atherosclerosis can be broken into two parts: the accumulation of oxidized (LDL) in the vascular intima and the following inflammatory signaling cascade that results in plaque development, leading to arterial blockage and thrombosis. Atherosclerosis begins when high levels of circulating LDL are transported into the extravascular space and become trapped in the extracellular matrix where they are subject to oxidative modification. Oxidized LDL causes damage to surrounding endothelial cells and initiates an inflammatory signaling cascade which results in the recruitment of monocytes to the site of injury (134). Monocytes differentiate into macrophages that express a bevy of different surface scavenger receptors (SR) active in the non-specific uptake of modified LDL. Two primary SR control the majority (75-90%) of the modified LDL uptake in macrophages, scavenger receptor type A (SR-A) and the type B scavenger receptor CD36 (135). Unlike receptors for native LDL, these SR are not down regulated by increased cholesterol concentrations within the cell, and macrophages do not have the ability to efficiently clear oxidized LDL (136). The excessive uptake of oxidized LDL results in the formation of foam cells which become engorged, die, and subsequently form atherosclerotic plaques. These plaques grow in size and can occlude the arterial lumen obstructing blood flow ultimately resulting in an infarct.

3.1.1 Structure of Scavenger Receptor A

The three-dimensional structure of SR-A is unknown, however Kodama and coworkers purified bovine SR-A and hypothesized the structure to be a trimer composed of five or six structural domains dependent on alternate RNA splicing: a cytoplasmic N-terminal domain, a membrane-spanning region, a spacer region, an α-helical coiled-coil domain, a collagen-like domain, and a cysteine-rich C-terminal domain present in SR-A type I but not SR-A type II receptors (137); (138). Truncation studies implicated the α-helical coiled-coil domain in trimer formation and showed the collagen-like domain is responsible for ligand recognition and binding (139). Site directed mutagenesis uncovered a conserved cluster of positively charged amino acids in the distal end of the collagenous domain: Lys327, Lys334, Lys337 and Lys340 of bovine SR-A (corresponding to Arg325, Lys332, Lys335, and Lys338 in human SR-A) forming a positively charged groove which interacts electrostatically with anionic oxidized LDL (139); (140). Further mutation studies by Andersson and Freeman(141) proposed additional cationic residues nearer the central and N-terminal regions of the SR-A collagenous domain that could also be involved in binding oxidized LDL.

3.1.2 Nanolipoblockers as Inhibitors of Oxidized Low Density Lipoprotein Uptake

One method developed to combat the formation of atherosclerotic plaques is to prevent cellular uptake of oxidized LDL using inhibitors selectively designed to block the interaction of LDL with SR-A (142); (143). Tian et al. (144) developed a class of anionic, micelle-forming molecules comprised of a mucic acid head group with attached aliphatic chains and a long PEG tail which were subsequently shown to be effective in blocking oxidized LDL uptake (145); (146); (147). Plourde et al. (148) explored the structure-function relationship of these macromolecular inhibitors (referred to henceforth as nanolipoblockers (NLB)) to determine the influence of charge and charge location upon the ability of NLB to inhibit oxidized LDL uptake by SR-A. The authors used a combined experimental and computational (MD docking techniques) approach finding that NLBs containing hydrophobic-bound carboxylate groups were the best inhibitors of oxidized LDL uptake, but the specific mechanism for inhibition was unclear. The authors did find good agreement between experimental and computational results, but the all-atom force field used for molecular docking limited the size of the computational system to the collagen-like domain of SR-A and one or two truncated NLB molecules. Experimental studies have shown that micellization is a likely requirement to inhibit oxidized LDL uptake, (148); (149) and thus the interaction of one or two NLBs with SR-A may not be sufficient to characterize the inhibiting function of NLBs.

3.2 Coarse-Grained Simulation of Nanolipoblocker Aggregates with Scavenger Receptor A

In this chapter we expand upon the computational studies of Plourde et al. (148) and develop a CG MD approach based on the MARTINI force-field of Marrink and coworkers (150); (70) to study the aggregation behavior of complete NLB molecules and the binding of NLB aggregates to the collagenous domain of SR-A. We assess the micelle-forming capabilities of different NLBs and probe the specific interactions between NLBs and SR-A to characterize the mechanism by which micellular aggregates of NLBs act to prevent oxidized LDL uptake by SR-A. Knowledge of these specific interactions may aid in streamlining the search for more effective inhibitors.

3.2.1 System Details

For simplicity, our simulations only consider the collagenous domain of SR-A as it is the region shown to bind oxidized LDL (139); (141); (140). Due to the CG nature of the MARTINI force-field, in addition to the non-bonded and bonded interactions between the protein particles the force-field includes additional terms aimed at maintaining the secondary structure of the protein. As the exact 3-dimensional structure of the SR-A receptor is not known, we model the collagenous domain of SR-A using the collagen triple-helix parameters developed by Gautieri et al. (151). Residues 272-341 that make up the collagenous domain of SR-A are shown in Fig. 26 (here relabeled 1 to 70 for this study). The script seq2itp.pl (151) takes as input a protein sequence and outputs MARTINI interaction parameters in a GROMACS readable format. This script was used along with three identical chains of residues 272-341 were to generate MARTINI interaction parameters for SR-A. A suitable starting structure of the protein was built by first mapping an atomistic representation of the collagen-like domain of SR-A onto an ideal collagen triple helix using the software THeBuScr (Triple-Helical collagen Building Script) (152). The pdb2cg.awk script from the MARTINI website (www.md.chem.rug.nl/cgmartini) was used to convert the atomistic protein into a CG MARTINI representation. The resultant CG structure of SR-A was energy minimized and equilibrated in explicit solvent.

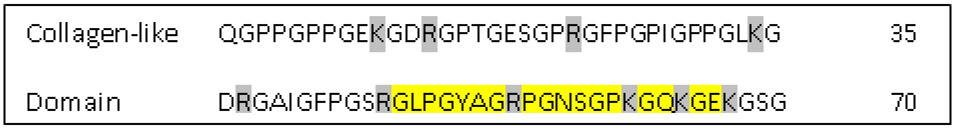

Collagen-like	QGPPGPPGEKGDRGPTGESGPRGFPGPIGPPGLKG	35
Domain	DRGAIGFPGSRGLPGYAGRPGNSGPKGQKGEKGSG	70

Figure 26: Amino acid sequence of the collagen-like domain of SR-A used in simulations. The proposed binding pocket for oxidized LDL is highlighted in yellow with the positively charged residues in grey. Other cationic residues outside of the binding pocket are also highlighted in grey.

Structures of the four different types of NLBs are shown in Fig. 27 along with their CG representation. A total of five different types of interaction sites were needed to describe all NLBs. The different interaction sites are described as follows: (i) Na accounts for the mucic acid backbone beads as they are equivalent to methylformate fragments, (ii) SC1 for aliphatic groups (70), (iii) SNa for PEG residues, (iv) SP2 for the terminal segment of PEG (153), and (v) Qa for the portions of NLBs carrying a negative charge (an explanation of the MARTINI naming scheme is given below). Standard MARTINI parameters were used for the non-PEG portion the molecules: bonded interactions ($R_b = 0.47$, $k_b = 1250$ kJ mol^{-1} nm^{-2}), and a harmonic angle potential was used to keep the aliphatic chains linear ($\theta = 180°$, $k_\theta = 25$ kJ mol^{-1}). The bonded parameters for the PEG tails used the values of Lee et al. (153). The four different structures of NLB molecules are named in accordance with Plourde et al. (148). 1CM contains a carboxylate group (type Qa) near the mucic acid head. 0CM is an uncharged NLB where the carboxylate group of 1CM is changed to neutral type Na. 1CP has a carboxylate group attached to the PEG tail. As the goal of the work was to study the variation in charge location, the ring structure of the 1CP head was not explicitly modeled, and MARTINI type Na is used for the 1CP head group. PEG-COOH consists only of a carboxylate head group attached to a long PEG tail with the aliphatic groups from other NLBs absent.

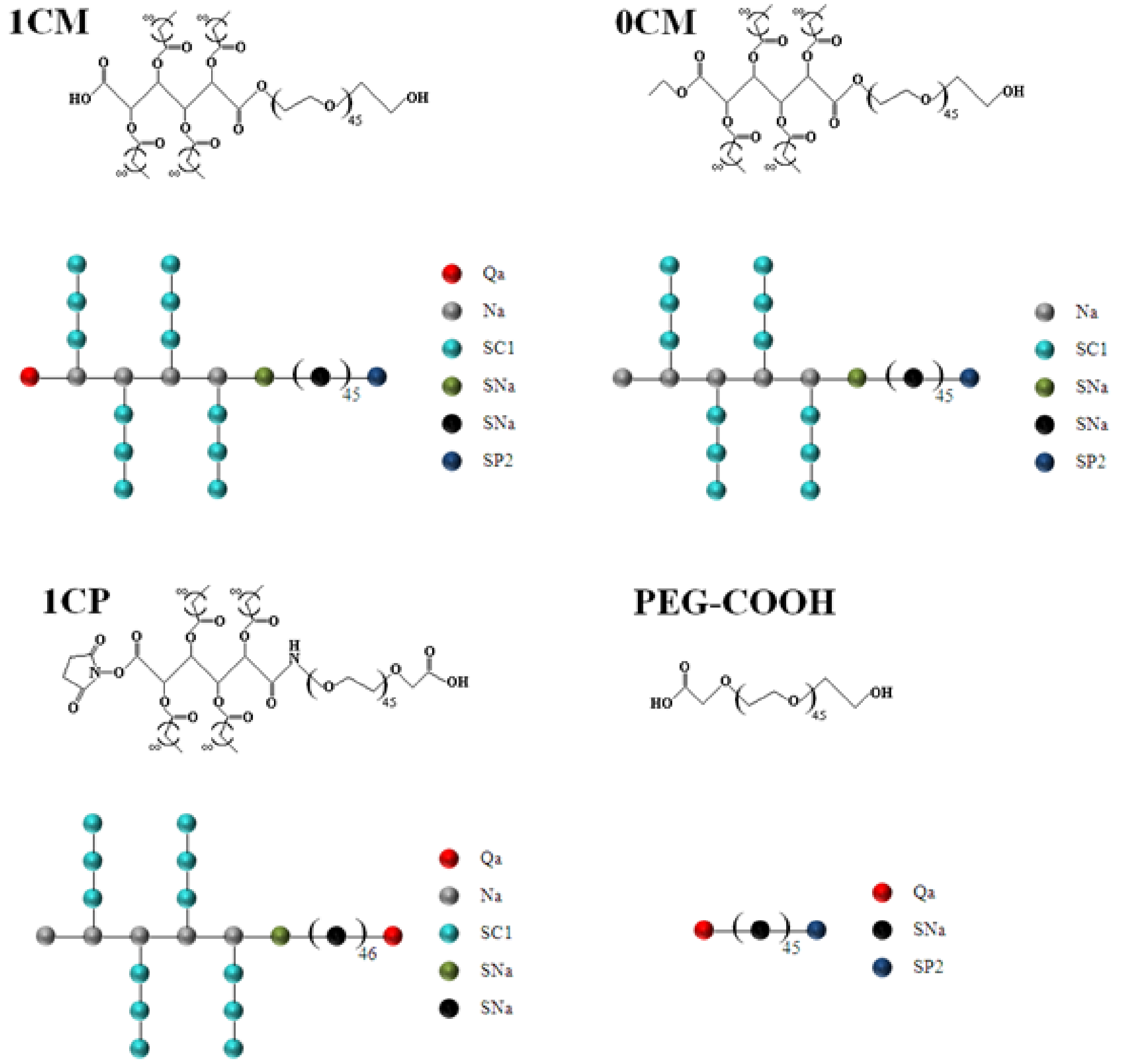
1CM
0CM
HO
OH
O
45
Qa
Na
SC1
SNa
SNa
SP2
1CP
PEG-COOH
N
H
46

Figure 27: Chemical structure and corresponding CG representation of the four different NLBs used in this study. 1CM has a carboxylate group near the aliphatic head of the molecule (Top-left); 1CP has the carboxylate group moved to the PEG tail (Bottom-left); 0CM is a neutral NLB with no carboxylate group (top-right); PEG-COOH contains only a carboxylate head group and a PEG tail (bottom-right).

The system under consideration for the functional interaction of differently structured NLBs with SR-A includes the collagenous domain of SR-A, 50 NLB molecules, enough Na^+ or Cl^- ions for an electrically neutral system, and approximately 100,000 CG water particles (400,000 water molecules). The components of the simulation are described using the CG MARTINI force-field developed by Marrink et al. (70) for the study of lipid bilayers systems that has since been extended to include both protein (154), and polymer (153); (155) systems. In the MARTINI force-field a CG interaction site (bead) is composed of four heavy atoms lumped together with an effective diameter of 0.47 nm or 2-3 heavy atoms with a diameter of 0.43 nm for smaller beads, such as those in ring-like structures. The beads are grouped into four types: polar (P), nonpolar (N), apolar (C), and charged (Q) with further sub-types of each bead available to address the degree of polarity (1 = lower polarity and 5 = higher polarity) and the ability for hydrogen bonding (d = donor, a = acceptor, da = donor and acceptor, 0 = none). Non-bonded interactions between beads are treated with a shifted Lennard-Jones potential and electrostatic interactions are treated with a Coulomb energy function using a relative dielectric constant of $\varepsilon_R = 15$. Bond and angle interactions are described by harmonic potentials and dihedral interactions are implemented to prevent out-of-plane distortions and maintain secondary structure (154).

Simulations were performed with the GROMACS software package v. 3.3.3 (102). In all simulations, the Lennard-Jones interactions were smoothly shifted to zero between a distance of 0.9 and 1.2 nm and electrostatics were smoothly shifted to zero between 0 and 1.2 nm. The non-bonded neighbor list was updated every 10 steps with a neighbor list cut-off of 1.4 nm. All simulations were performed in an NPT ensemble with the system coupled to a Berendsen thermostat (107) at 310 K with a coupling constant of $\tau_T = 1.0$ ps. Berendsen pressure coupling was used to maintain the system at a pressure of 1.0 bar using a coupling constant of $\tau_P = 2.0$ ps and a compressibility of 3×10^{-5} bar^{-1} (107). The integration time step was 10 fs. The CG nature of the MARTINI force field yields a smoother energy landscape which has been shown to result in 4-fold faster dynamics (150). Therefore, we henceforth report the effective time incorporating this scale-up factor. All Analysis was performed using GROMACS tools, and visualizations were created using VMD (156).

Initial simulations were performed with NLBs in the absence of SR-A to characterize the formation of NLBs into micelles. For each NLB, 25 molecules were randomly placed in a simulation cell and solvated with 70,000 water beads (280,000 water molecules) and run for 800 ns. Subsequent simulations of the interaction of NLBs with SR-A contained 50 NLBs equilibrated for 400 ns to which was added equilibrated SR-A resulting in a total system size of approximately 20 x 20 x 35 nm^3. As it has been shown that the α-helical coiled-coil domain and not the collagenous domain is responsible for trimer formation in SR-A (139), position restraints were applied to the backbone beads of the protein with a restraint force of 1000 kJ mol^{-1} nm^{-2} to prevent unraveling of the triple helix. The combined SR-A and NLB simulation was then run for 800 ns with the last 400 ns used for analysis. An initial snapshot of the 1CP system following energy minimization and 4 ns NVT equilibration is shown in Fig. 28.

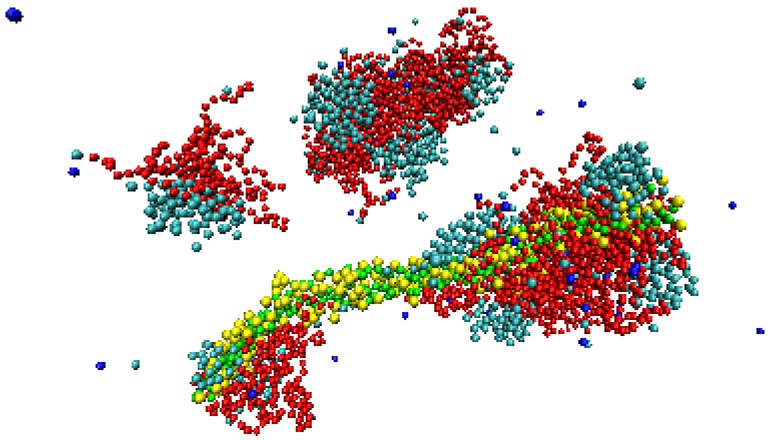

Figure 28: Snapshot of the 1CP simulation following energy minimization and NVT equilibration. SR-A is shown in yellow and green, 1CP micelles are shown in cyan (mucic acid and aliphatic segments) and red (PEG tail) with ions shown in blue. Waters are removed for clarity.

3.3 Formation of Nanolipoblockers into Micelles

To explore the micellization process of NLBs, we performed simulations of NLB self-assembly using 25 molecules randomly dispersed in a water box. The time-lapse configuration of micelle formation for 1CM is shown in Fig. 29. 1CM formed into stable aggregates of 5 micelles after approximately 300 ns as shown by the cluster analysis in Fig. 31. Similar trajectories and cluster formation were seen for 0CM and 1CP (data not shown). Two molecules were defined as belonging to the same cluster if the center of mass (COM) of their aliphatic beads (Type C1 in Fig. 27) were within 2.5 nm of each other, the distance at which the radial distribution function (RDF) exhibited a minimum. After 800 ns 1CM formed into 5 clusters with an average of 5 molecules per cluster with the largest cluster containing 10 NLBs. The values for the number of clusters, number of molecules per cluster, and the number of molecules in the largest cluster and the end of the 800 ns simulation are shown in Table 4 for all NLBs except PEG-COOH which did not form micelles (as shown in Fig. 30) as it does not contain the aliphatic chains of the other NLBs. For the largest micelles formed in each system, we measured the micelle radius of gyration (R_g) which can be related to the micelle radius (R_M) through the equation (157):

$$R_M = \sqrt{\frac{5}{3}} R_g \tag{19}$$

The average R_g was calculated over the final 400 ns of the simulation for each micelle type and is included in Table 4. Alternatively, the micelle radius can be estimated by measuring the root-mean-square (RMS) distance from the NLB tail beads to the micelle COM. The computed micelle radii using this method are also reported in Table 4. Micelle radii for the different NLBs range from 3.8 nm to 6.4 nm. This is smaller than the results obtained by Wang et al. (146) who found that 1CM micelles had an average diameter of 23.2 ± 5.2 nm (11.6 ± 2.6 nm radius), however those results were obtained for NLB molecules with a tail containing 114 PEG repeats (5000 MW) rather than 45 PEG repeats (2000 MW) which we have used in our simulations. Tian et al. (144) measured NLBs with 2000 MW and 5000 MW PEG tails and found the overall micelle radii to be between 5 – 10 nm (diameter of 10 – 20 nm). The lower bound values of Tian et al. (144) correspond to NLBs with 2000 MW PEG tails, so our results seem reasonable. The major drive for inclusion of longer PEG tails experimentally is to increase the PEG density around the NLB interior, enhancing the micelle stability and protecting the interior from degradation by serum proteins. The decreased PEG tail length of our simulations with relation to the NLBs used experimentally (149); (158) are not expected to greatly alter the binding modes of NLBs to SR-A.

Table 4: Cluster analysis (mean ± SD) of the micelle-forming NLBs calculated over the last 400 ns of the simulation.

	0CM	**1CM**	**1CP**
Number of Clusters	2.96 ± 0.20	4.99 ± 0.10	4.83 ± 0.38
Molecules Per Cluster	8.50 ± 0.83	5.01 ± 0.12	5.21 ± 0.47
Max Cluster Size	11	10	11
R_G (nm)	2.93 ± 0.22	4.80 ± 2.67	4.93 ± 1.06
R_M - From R_g (nm)	3.78 ± 0.28	6.20 ± 3.45	6.36 ± 1.37
R_M - From RMS (nm)	4.15 ± 1.41	5.13 ± 2.03	5.45 ± 2.18

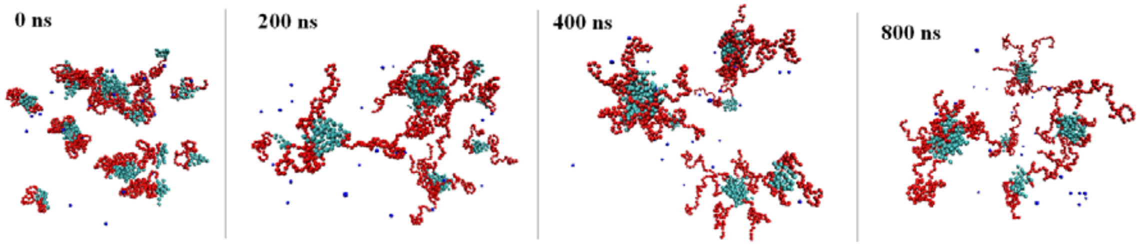

Figure 29: Snapshot of the self-assembly process of 1CM NLB into micelles. The system began with 25 randomly distributed NLB and proceeds for 800 ns. The particles colored red are the PEG tails and those colored in cyan are the mucic acid and aliphatic groups.

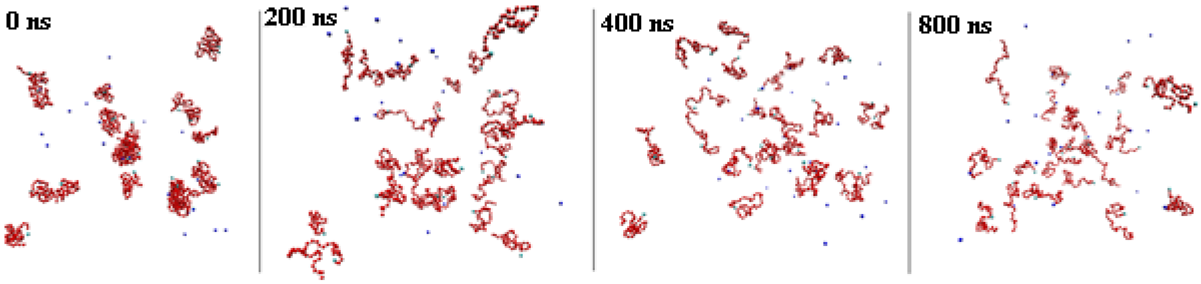

Figure 30: Snapshot of PEG-COOH showing that it does not form micelles. The system began with 25 randomly distributed NLB and proceeds for 800 ns. The particles colored red are the PEG tails and those colored in cyan are the mucic acid and aliphatic groups.

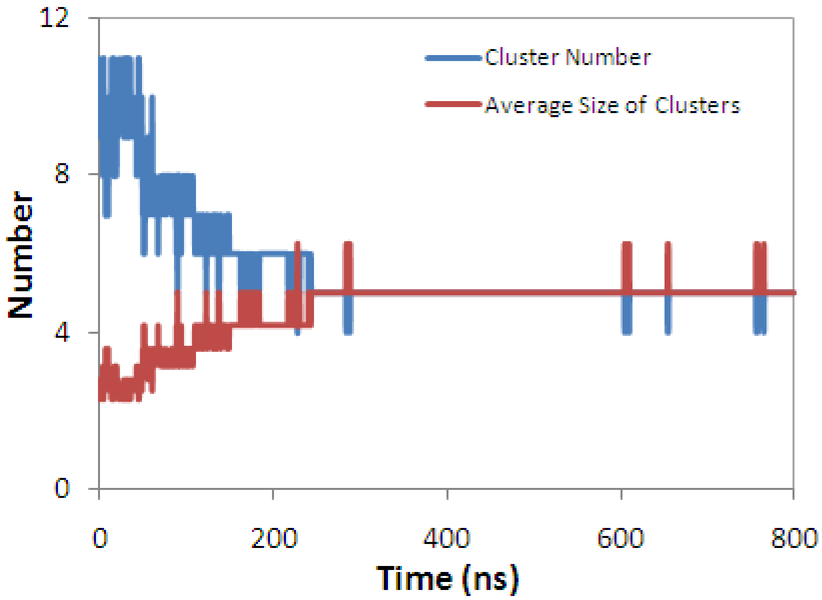

Figure 31: Evolution of the cluster distribution for 1CM micelles with 25 NLB molecules and 70,000 CG waters.

3.3.1 Interaction of Nanolipoblockers with Scavenger Receptor A

To explore the specific interactions of different NLB architectures with SR-A, we performed simulations of 4 different types of NLB molecules with the collagenous portion of SR-A. For each NLB type, 50 NLB molecules were combined with an equilibrated trimeric SR-A molecule and simulated for a total of 800 ns. The final configuration for all NLBs interacting with SR-A is shown in Fig. 32a-d. For micelle-forming NLBs (0CM, 1CM, 1CP), it is quite clear that the interaction with SR-A was preferentially in the form of whole micelles rather than in monomeric form. PEG-COOH, which does not form micelles, interacted as single unimers which wrapped themselves around the protein. Figure 32a shows 0CM in which one large micelle interacts with the N-terminal region of SR-A while a smaller micelle was present towards the C-terminal end. Also to note is that there were two small micelles in solution which did not appear to interact with the protein. The experiments of Plourde et al. (148) showed that 1CM was the best NLB at inhibiting uptake of oxidized LDL by THP-1 macrophages followed by 1CP, 0CM, and finally PEG-COOH which produced minimal uptake inhibition. The presence of non-interacting 0CM micelles in solution may be indicative of weaker binding between 0CM and SR-A and a possible explanation of why 0CM does not inhibit oxidized LDL uptake as potently as 1CM; not all of the 0CM molecules form into micelles that interact with SR-A. The interaction of 1CP with SR-A was similar to 0CM with one larger micelle interacting with the N-terminal end of SR-A and another micelle nearer the middle of the protein with two micelles floating in solution. Conversely the 1CM simulation contained two large micelles interacting with both the N-terminal and C-terminal ends of SR-A. The observation that 1CM shows enhanced interaction over 1CP and 0CM with the C-terminal end of the collagenous domain, which contains the proposed binding site for oxidized LDL, is consistent with experimental evidence showing 1CM to be a better inhibitor of oxidized LDL uptake (148); (149). Finally, Fig. 32d shows PEG-COOH interacted as monomers somewhat homogenously along the protein, wrapping around SR-A in a layer 1 molecule thick and a number of PEG-COOH NLBs in solution

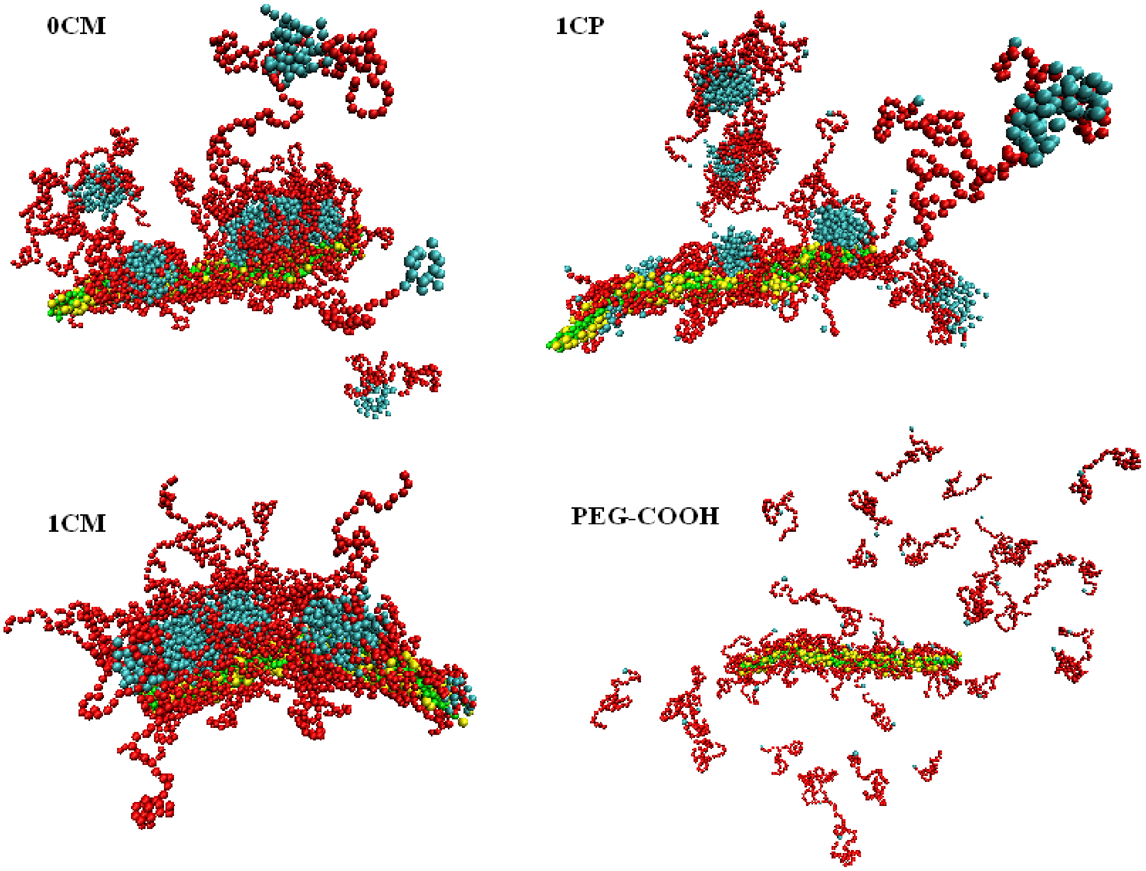

Figure 32: Interaction following 800 ns of simulation of SR-A with each type of NLB (clockwise starting in the lower-left) 1CM, 0CM, 1CP, and PEG-COOH. The protein is shown in green and yellow, the NLB is red and cyan.

3.3.2 Molecular Contacts between Nanolipoblockers and Scavenger Receptor A

Subsequent analysis focused on quantitatively assessing the extent of interaction between the four different NLBs and SR-A by computing the total number of contacts between the two. A contact was defined with a distance cutoff of 0.8 nm between any two beads (62) corresponding to a distance slightly less than two of the smallest CG particles (0.43 nm) in contact with one another. The number of contacts made between each NLB and SR-A throughout the last 400 ns of the simulation (solid line) and the average over this time (dashed line) are shown in Fig. 33. The error bars represent the standard error of the mean for 10 ns block averages of the data. For a 0.8 nm cutoff, there was a fair amount of variability in the number of contacts for a given NLB over the length of the simulation, but the general trend is 1CP > 1CM > 0CM > PEG-COOH which deviates slightly from experimental evidence that demonstrates the effectiveness of NLBs at inhibiting oxidized LDL uptake is 1CM > 1CP > 0CM > PEG-COOH (148). The experimental findings however, concluded that both 1CM and 1CP inhibited oxidized LDL uptake over the basal condition whereas 0CM and PEG-COOH did not. Given that the average number of contacts between 1CP and 1CM were similar, and both were larger than 0CM and PEG-COOH, it seems that there is agreement with experimental data. While number of contacts do not directly measure oxidized LDL uptake, one can infer that the NLBs making the most associations with SR-A would tend to inhibit binding of oxidized LDL to the receptor and thus decrease its uptake. To explore the ability of each NLB to sterically block a large area around the protein, the number of contacts that each NLB forms with SR-A within 2.0 nm (roughly twice the distance of two of the largest CG particles (0.47 nm) in contact with one another) was also calculated and is shown in Fig. 33b. In extending the contact cutoff to 2.0

nm it became clear that 1CM had the highest density of molecules near the surface of SR-A with an average of 69712 contacts over the last 400 ns of the simulation. 0CM and 1CP formed an average of 60800 contacts and 58095 contacts respectively, both lower than that of 1CM. PEG-COOH formed appreciably less contacts at a cutoff of 2.0 nm than any of the other NLBs. The contact results can be explained by referring back to the final simulation snapshots in Fig. 32. Two large 1CM micelles interacted with SR-A and few molecules were not interacting with the protein. Conversely, both 0CM and 1CP had micelles in solution not interacting with SR-A and did not cover as much of the protein as 1CM. In the case of PEG-COOH, the majority of the interactions are as PEG-COOH unimers wrapping around SR-A resulting in a larger number of close contacts (< 0.8 nm) but a decrease in contacts further away from SR-A (< 2.0 nm) as PEG-COOH did not interact with SR-A as aggregates and a large number of molecules could be seen floating in solution. Though a number of short-distance contacts were formed between PEG-COOH and SR-A it was not as effective as other NLBs in sterically protecting the binding region of SR-A from large oxidized LDL particles.

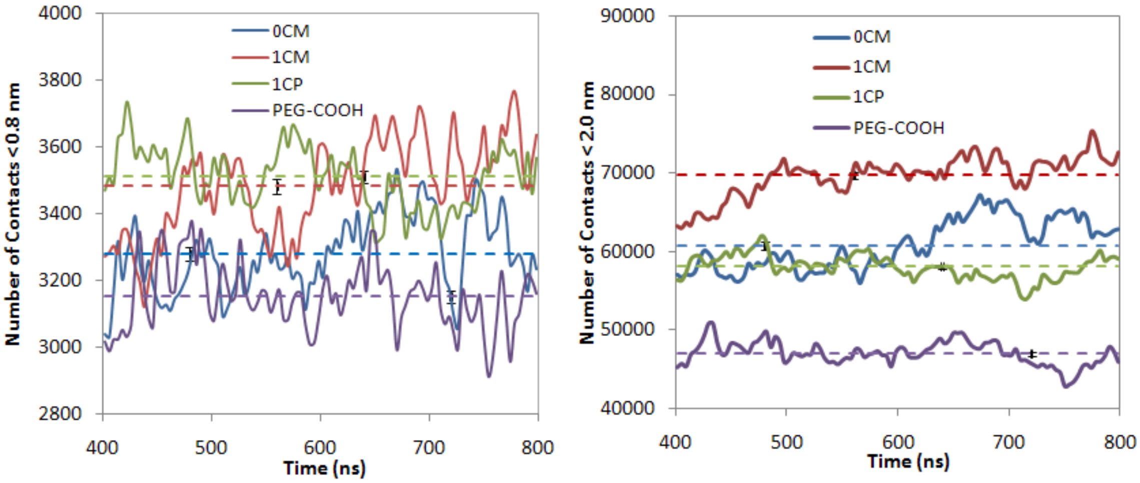

Figure 33: The number of contacts that NLBs form with SR-A in the final 400 ns of simulation time. A contact is defined as with an interparticle cutoff of 0.8 nm (Left) or 2.0 nm (Right). The dashed lines show the average number of contacts for each NLB over the course of the simulation. Error bars represent the standard error of the mean for 10 ns block averages.

Figure 34 shows a contact map in which SR-A is colored according to the number of persistent contacts each CG bead of SR-A made with NLB molecules for each type of NLB. Here, a contact is defined by an NLB molecule within 2.0 nm of an SR-A bead and persisting for greater than 75% of the last 400 ns of simulation time. The protein is represented by a wire mesh, and the charged residues thought to be involved in oxidized LDL binding are represented as spheres. Blue coloration indicates 0-4 persistent NLB contacts (low), the beads colored white represent 5-8 contacts (medium), and those colored red signify greater than 8 contacts (high) that lasted for at least 75% of the simulation time. The total number of protein beads falling into each category (low, medium, high) for each NLB is shown in Table 5. The interaction of 0CM with SR-A occurred primarily in the N-terminal region (away from the proposed binding pocket) and extended into the middle of the protein with minimal interaction at the C-terminal end. There was moderate interaction with the more central residues of the charged oxidized LDL binding pocket (Arg46 and Arg54) with the interaction decreasing moving towards Lys67, the last residue of the binding pocket. Compared to 0CM, 1CM had more persistent interactions with the middle of SR-A including some strong interactions with Arg46 and Arg54 and moderate contacts with the charged lysines of the binding pocket: Lys61, Lys64 and Lys67. Overall, 1CM showed the most contacts with SR-A consistent with Fig. 33b. 1CP, like 0CM showed the majority of strong contacts with the N-terminal region of SR-A. There was a strong contact with Arg46 and moderate contacts with Arg54 and Lys61 of the binding region, but little interaction with Lys 64 or Lys67. PEG-COOH exhibited the least contact with SR-A no region having more than eight persistent contacts. There was moderate interaction with the more central residues of the binding pocket (Arg46 and Arg54) and some interaction with Lys61 but no interaction with Lys64 or Lys67. The minimal interaction of PEG-COOH with SR-A as a whole may explain why experimentally it is the worst of the four NLBs at inhibiting oxidized LDL uptake, but the moderate interaction with the terminal lysines could explain why it PEG-COOH was found to be energetically a good binder (148).

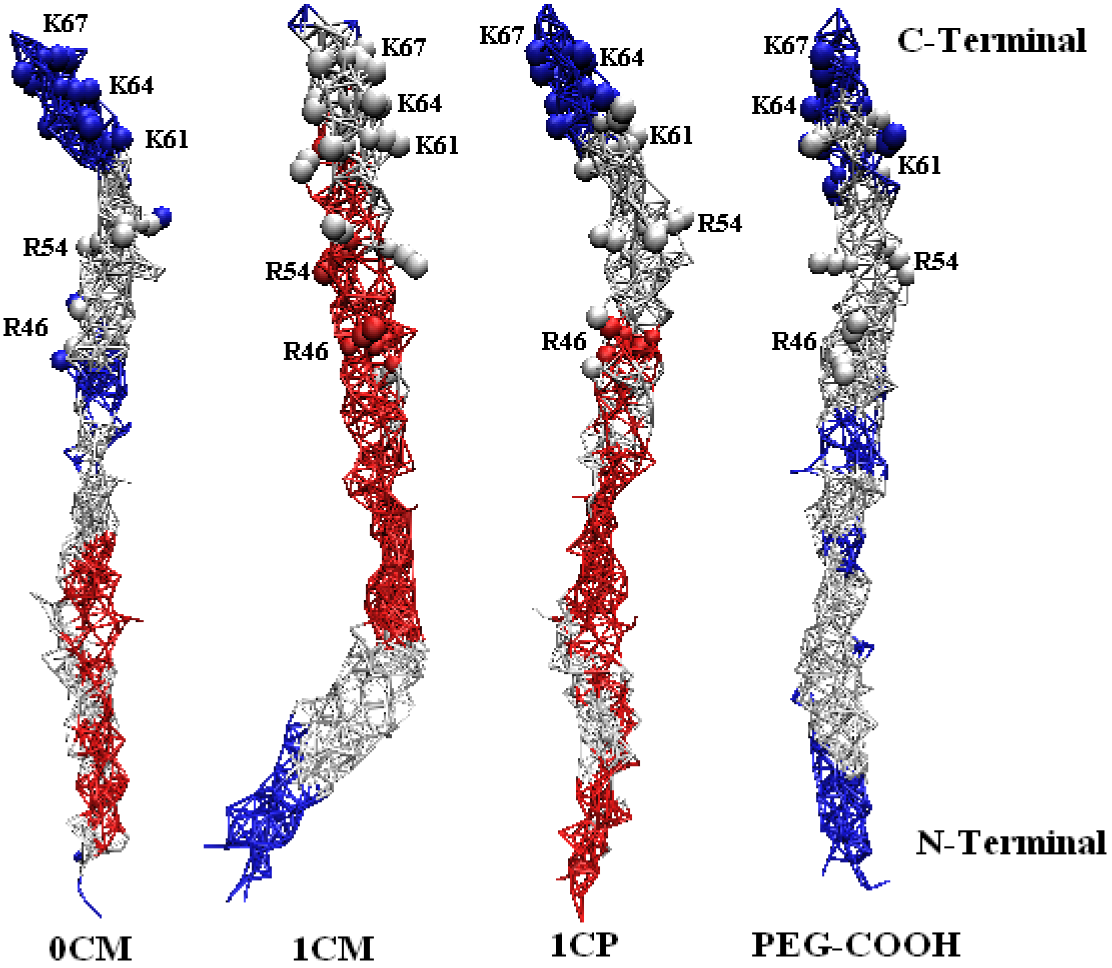

Figure 34: Contact Map of interactions between NLBs and SR-A. All panels show the collagenous domain of SR-A in a wire-mesh with the residues from Fig. 26 (charged binding pocket) represented as spheres. The protein beads are all colored according to the number of contacts that each bead makes with NLB molecules. A contact is defined as an NLB molecule within 2nm of the protein bead (residue) that persisted for greater than 75% of the simulation time. The atoms shown in blue interacted with 0-4 NLB molecules, those colored in white interacted with 5-8 NLB molecules, and those colored in red interacted with greater than 8 NLBs for more than 75% of the simulation time (400 ns).

Table 5: Number of SR-A CG beads with persistent contacts at three different levels (low, medium, high) for each type of NLB along with the average number of persistent contacts.

	0-4 Contacts	5-8 Contacts	9+ Contacts	Average #
0CM	107	205	78	6.06
1CM	49	139	202	8.69
1CP	44	175	171	8.07
PEG-COOH	135	255	0	4.89

3.3.3 Interaction of Nanolipoblockers with the Binding Pocket of Scavenger Receptor A

It is hypothesized that the residues important in oxidized LDL binding to human SR-A are Arg317, Arg325, Lys332, Lys335, and Lys338 (139); (141) which correspond to R46, R54, K61, K64, and K67 in our studies (Fig. 26). To examine the electrostatic interactions between these residues and NLBs, in addition to the total number of contacts we also separately calculated the number of contacts between residues of the charged binding pocket and either the head (negatively charged terminal bead of 1CM and PEG-COOH) or the tail (negatively charged in 1CP) for all four NLBs (neither the head nor tail is charged in 0CM). Figure 35 displays the average number of contacts at 0.8 nm for the head and tail beads (Fig. 35a and 35b respectively) and the average number of contacts at 2.0 nm for the head and tail beads (Fig. 35c and 35d respectively). The error bars represent the standard error of the mean for block averages of 10 ns. The number of close contacts (< 0.8 nm) of the NLB tails with any of the essential residues of the binding pocket was minimal across all

NLBs. The average number of tail contacts hovered around 0.5 for any NLB, meaning that each residue of the binding pocket had a tail bead within 0.8 nm for only half of the simulation time. It was hypothesized that the negative charge on the tails of 1CP would interact with the cationic C-terminal lysine and arginine residues, but this was not observed in our simulations preferentially over NLBs with uncharged tails. Placing an anionic charge at the head of the NLB conversely resulted in the NLB forming more close contacts with the binding residues of SR-A. All NLBs showed a favorable interaction with Arg54, but only 1CM and PEG-COOH with their anionic head groups demonstrated close contacts with the other essential residues of the binding pocket. 1CM showed good interactions with Arg46 (0.77 ± 0.12) and Lys61 (1.14 ± 0.11) while PEG-COOH had contacts with Lys61 (0.92 ± 0.12) and with Lys64 (1.06 ± 0.10). Extending the contact radius to 2.0 nm resulted in a similar finding with respect to binding pocket residues contacting NLB tails. The negatively charged tails of 1CP did not facilitate interaction with the binding pocket and in fact, 1CP showed the lowest number at 2.0 nm of all NLBs. The NLB head interaction at 2.0 nm showed 1CM forming good associations with Arg46, Arg54 and Lys61 of the binding pocket, but interacted to a lesser extent with Lys64 and Lys67, yet the number of contacts was greater than uncharged 0CM. PEG-COOH formed consistent 2-3 contacts at 2.0 nm with all residues.

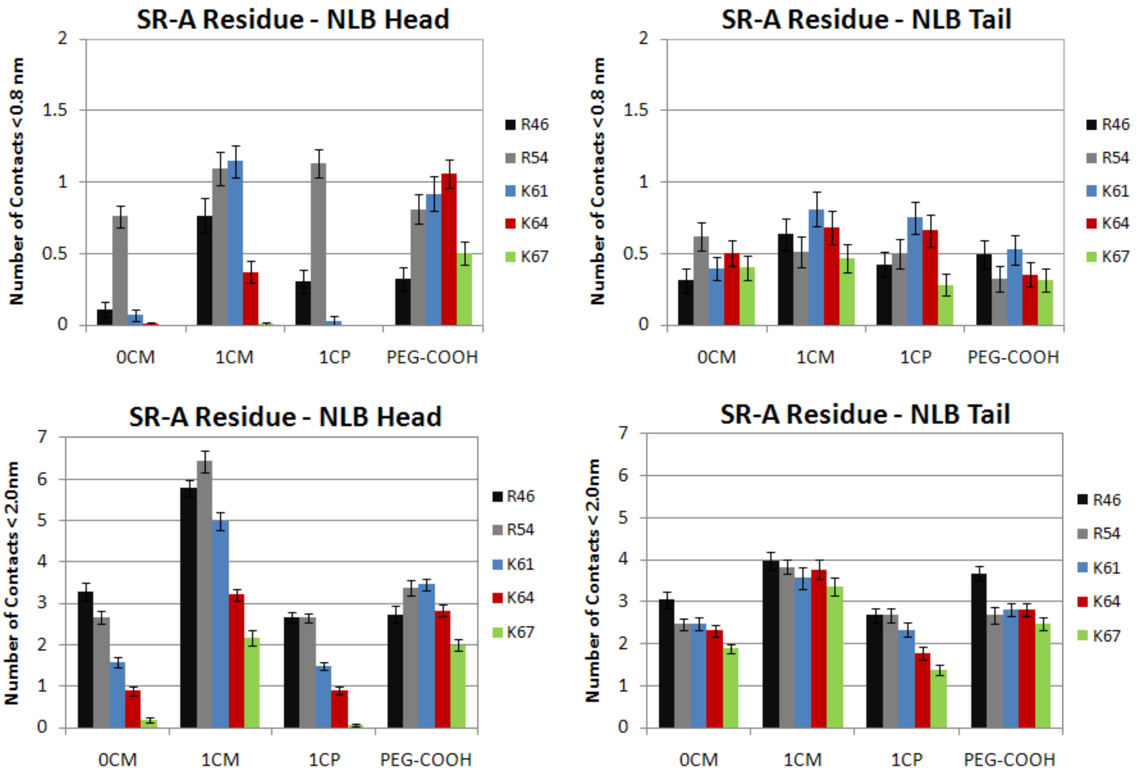

Figure 35: Average number of contacts within 0.8 nm (top) for the NLB head (a) or tail (b) and the average number of contacts within 2.0 nm for the head (c) and tail (d) beads. In 1CM and PEG-COOH the head beads are negatively charged whereas in 1CP the tail bead is negatively charged. 0CM is neutral at both the head and tail and carries no charge. The legends refer to the one-letter amino acid code as given in Fig. 26.

3.3.4 Discussion of Contact Results

Here we have used CG-MD simulation to explore the interactions between SR-A and engineered micellular nanoparticles (NLB) designed to block the uptake of oxidized LDL by SR-A. Oxidized LDL is a negatively charged ligand for SR-A and is thought to interact with a group of positively charged residues in the collagen-like domain of SR-A. We simulated the interaction of SR-A with four different NLBs (0CM, 1CM, 1CP, and PEG-COOH) differing in the magnitude of the negative charge (charge = 0 for 0CM and -1 for the rest) location of the charge (near the macromolecule head in the case of 1CM or at the tail in the case of 1CP) or the NLBs ability to form micelles (PEG-COOH lacks the aliphatic groups of the other NLBs and thus did not form micelles). Of the NLBs that formed micelles (0CM, 1CM, 1CP) the micelles generally formed within ~300 ns and had a micelle diameter between 8-12 nm consistent with the lower bound of Tian et al. (144). NLBs which formed micelles preferentially interacted with SR-A in the form of micelles rather than single monomers indicating that NLBs primarily interact with SR-A in an aggregated state. 0CM and 1CP formed micelles that interacted principally with the N-terminal and center portions of SR-A (as indicated by the contact map in (Fig. 34) while also showing micelles in solution away from the protein surface. 1CM associated with SR-A by way of two large micelles near both the C-terminal and N-terminal ends with no aggregates observed in solution, suggesting that 1CM micelles interact more favorably with SR-A than either 0CM or 1CP micelles. PEG-COOH alternatively did not form micelles and interacted with SR-A as monomers with a number of molecules in solution.

Exploring the number of close contacts that NLBs made with SR-A at a distance of 0.8 nm, indicated that 1CM and 1CP formed the most contacts, but the values were not greatly different from the other NLBs (0CM and PEG-COOH). When the contact radius was extended to those within 2.0 nm, it became clear than 1CM made the most contacts with SR-A, 1CP and 0CM made a similar number of contacts, and PEG-COOH made fewest (Fig. 33b). As the method for blocking SR-A is to occlude the entire binding region to prevent the binding of oxidized LDL it would be beneficial to cover the greatest portion of SR-A and thus a micelle with the most contacts within 2.0 nm would be the most effective at disallowing any interaction of oxidized LDL with SR-A. Our results are consistent with experimental findings that 1CM was the best (of the four NLBs tested here) at inhibiting oxidized LDL uptake by SR-A. Experimental results show that 1CP is a better inhibitor than 0CM of oxidized LDL uptake, a result confirmed by the number of contacts shown in Fig. 33. To further investigate this phenomenon, we computed the number of contacts between NLB heads (which are charged in 1CM and PEG-COOH) or the tails (which are charged in 1CP) with the residues implicated in oxidized LDL binding. In general, 1CP did not show any enhanced interactions over the other NLBs with any of the binding pocket residues. This could be due to the micelle structure that 1CP formed. With the negative charges placed on the PEG tails of 1CP, they extend radially outward from the micelle interior and were thus unlikely to cluster in one location. To enhance association of NLBs with the cationic residues of the SR-A binding pocket, it proved better to place a negative charge near the NLB head. Both 1CM and PEG-COOH showed enhanced interaction of their head groups compared to NLBs with neutral head groups. This is in agreement with Plourde et al. (148) who found 1CM and PEG-COOH to be the energetically best binders to SR-A. However, experimentally 1CM is a strong inhibitor of oxidized LDL uptake whereas PEG-COOH shows no deviation from the basal condition. This is likely due to the fact that 1CM binds as micelles while PEG-COOH binds as monomers. Measuring the number of contacts at a distance of 2.0 nm from the surface of SR-A showed 1CM forming appreciably more contacts than PEG-COOH suggesting that SR-A may not be sufficiently sterically blocked by PEG-COOH molecules. Oxidized LDL molecules are 22-28 nm in diameter (159) and it is possible that an incoming LDL molecule could form sufficient interactions with SR-A to displace a handful of PEG-COOH monomers. 1CM existing as a large micelle around SR-A could be sufficient to sterically disallow oxidized LDL to near the receptor and form any type of interaction.

3.4 Conclusions of Coarse-Grained Simulation of Nanolipoblocker Interaction with Scavenger Receptor A.

We performed CG MD simulations of the interaction between engineered macromolecules designed to block the uptake of oxidized LDL by SR-A. Previous studies of structure-function relations in NLBs used atomistic models that were only capable of assessing interaction between SR-A and one or two truncated NLBs. Here we have employed a CG model to explore the micelle forming dynamics of NLBs and the interaction of micellular aggregates of NLBs with SR-A. In our simulations 0CM, 1CM, and 1CP NLBs formed into micelles within 300 ns with the largest micelles consisting of 10 to 11 NLB molecules with a micelle radius of 3.8 – 6.4 nm while PEG-COOH did not form micelles in agreement with experiential observations. The interaction studies between NLBs and SR-A showed that 1CM, 1CP, and 0CM NLBs interacted with SR-A as micellular aggregates while PEG-COOH interacted as single monomers. The interaction of both 0CM and 1CP was primarily with the N-terminal end and middle of the protein while 1CM interacted with both the N-terminal and C-terminal regions or SR-A. As an indirect assessment of binding affinity, we examined the number of contacts that each type of NLB made with SR-A both at 0.8 nm and 2.0 nm from the receptor. The number of close contacts (< 0.8 nm) were similar for each NLB, but aligned with experimental trends showing 1CM and 1CP to be the best inhibitors of oxidized LDL uptake over 0CM and PEG-COOH. Extending the contact cutoff to 2.0 nm showed the ability of the NLBs to sterically block the entire binding domain from LDL particles. 1CM again formed the most contacts with SR-A at 2.0 nm as the large micelles extended far away from the protein surface. PEG-COOH showed significantly less contacts in the range of 2.0 nm than the other NLBs allowing for the possibility that incoming LDL particles may displace weakly attached PEG-COOH molecules. Finally, in calculating the specific contacts between the charged portions of NLBs and the binding pocket of SR-A indicated that the addition of a negative charge on the PEG tails of NLBs did not act to enhance interaction with the residues of the SR-A binding pocket, however an anionic charge at the NLB head increased interaction with the positively charged residues of the binding pocket, confirming the experimental finding that 1CM is the best inhibitor to oxidized LDL uptake as it most strongly associates with SR-A.

Chapter 4 Molecular Simulation of Nucleation of Pharmaceuticals in the Presence of Polymeric Additives

Control over crystallization is essential for correct product formulation in the field of pharmaceutical nanotechnology, and controlling nucleation is a crucial step. Despite its ubiquitous nature nucleation is a process that is poorly understood as the outcome can be dependent on a variety of factors such as the physiochemical properties of the nucleation compound, the presence of additives, and processing conditions. One particular area of interest is in using polymers to control drug nucleation from solution. In this chapter, we seek to develop a simulation platform using Monte Carlo and Molecular Dynamics simulations to study nanocrystal nucleation of drug molecules from solution in the presence of polymers. The structural and energetic properties of polymer-drug systems will be investigated with the goal of determining factors that act to increase or decrease the energetic barrier to drug nucleation.

4.1 General Nucleation Theory

In an unsaturated solution solute molecules are homogenously dispersed throughout the solvent and no nucleation occurs. Upon crossing the saturation point the frequency of molecular collisions increases and the solute begins to form small clusters. Many of these clusters are not thermodynamically stable due to the high surface energy and will dissolve back into solution. Nucleation is an activated process and requires a certain amount of energy in order to proceed. Nucleation of solute in solution can be viewed as a competition between the surface free energy (ΔG_{surf}) and the volume free energy (ΔG_{vol}).

$$\Delta G = \Delta G_{surf} + \Delta G_{vol} \tag{19}$$

For nucleation to occur, the free energy of the system (ΔG) must be favorable (negative). The surface free energy is the energy expended in the creation of a new surface within the solvent and is proportional to the cluster surface area and the surface tension (γ) between the solute cluster and the surrounding solvent. For spherical clusters this quantity is:

$$\Delta G_{surf} = 4\pi r^2 \gamma \tag{20}$$

where *r* is the cluster radius. The volume free energy is the energy gained through favorable solute-solute contacts (ε) multiplied by the volume of the cluster. For spherical clusters this is:

$$\Delta G_{vol} = \frac{4}{3}\pi r^3 \varepsilon \tag{21}$$

The free energy of the system is:

$$\Delta G = 4\pi r^2 \gamma + \frac{4}{3}\pi r^3 \varepsilon \tag{22}$$

In Fig. 36 the free energy as a function of cluster radius is schematically shown. For small clusters the surface tension term dominates while the volume term dominates once the cluster passes a critical size.

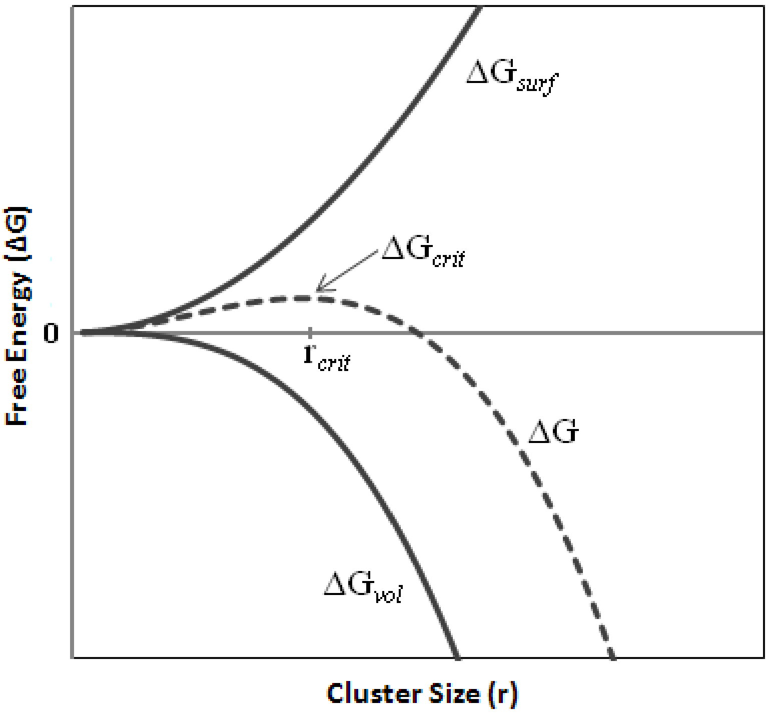

Figure 36: Schematic of the free energy of cluster formation as a function of cluster size. The free energy of formation goes through a maximum at $r = r_{crit}$ past which clusters are stable and can grow to macroscopic size.

For small clusters, increases in cluster size unfavorably increases the system free energy making small clusters likely to dissolve back into solution. When the cluster radius reaches r_{crit} clusters are stable and nucleation proceeds favorably. The size of a critical cluster can be found by maximizing Eqn. 22 with respect to *r*.

$$\frac{d\Delta G}{dr} = 0 = 8\pi r\gamma + 4\pi r^2\varepsilon \tag{23}$$

$$r_{crit} = \frac{-2\gamma}{\varepsilon} \tag{24}$$

The free energy required to form the critical nucleus (ΔG^*) is:

$$\Delta G^* = 4\pi r_{crit}^2\gamma + \frac{4}{3}\pi r_{crit}^3\varepsilon = \frac{16\pi\gamma^3}{3\varepsilon^2} \tag{25}$$

Therefore, although the formation of a crystal nucleus in a supersaturated solution is a favorable process, it requires a certain activation energy associated with the formation of a critical nucleus (Fig. 37). This activation energy is termed the *nucleation barrier*. The nucleation rate can be related to the nucleation barrier through the equation:

$$J = K_N exp\left(\frac{\Delta\Omega}{k_B T}\right) \tag{26}$$

where J is the nucleation rate, K_N is a kinetic prefactor related to the molecular mobility, $\Delta\Omega$ is the nucleation barrier, k_B is Boltzmann's constant, and T is the temperature.

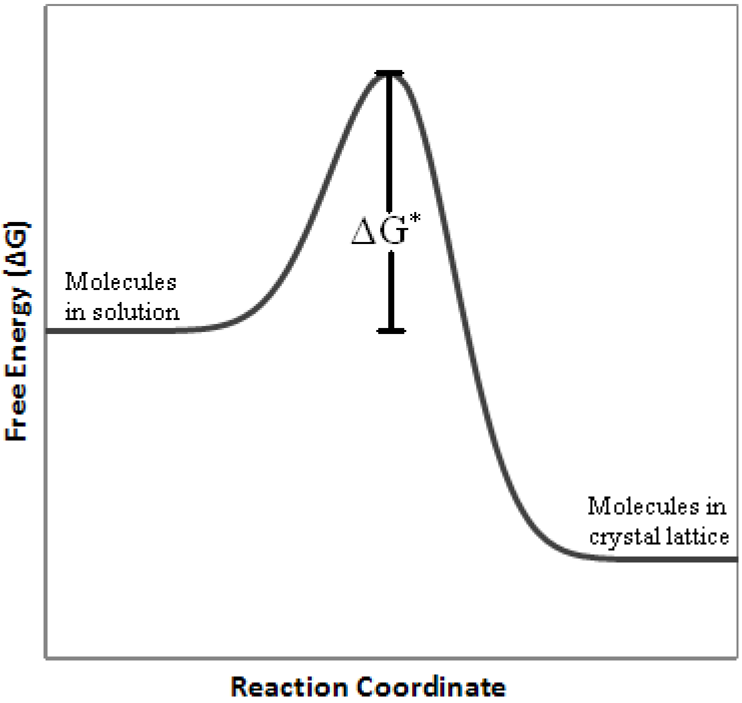
ΔG*
Molecules in solution
Molecules in crystal lattice
Free Energy (ΔG)
Reaction Coordinate

Figure 37: Representation of the nucleation barrier in transitioning from molecules dispersed in solution to molecules in a crystalline lattice.

4.1.2 Nucleation from Solution in the Presence of Polymers

Crystallization is a widely used unit operation in the chemical and pharmaceutical industries, however the process is still largely ad hoc and poorly understood. Nucleation in particular poses many difficulties due to the random, stochastic nature of the process. A supersaturated solution has a chemical potential that is greater than the chemical potential of an equilibrium saturated solution. The difference between the two chemical potentials is the driving force for nucleation. As stated above, nucleation is a favorable process but requires an energetic barrier be overcome before the process will proceed. When the nucleation barrier is high, new precipitates cannot form and the solution remains in a metastable state until, through random density fluctuations, the barrier is overcome and a stable crystal forms and begins to grow. The addition of polymers to a nucleating system can have varying effects dependent on the nature of the molecular interactions within the system. In the pharmaceutical realm it is important to be able to reliably produce the most stable polymorph for the drug of interest. Different polymorphs of a drug can have vastly different properties associated with bioavailability and efficacy, and inter-conversion from a metastable polymorph to a more thermodynamically stable polymorph could have deleterious effects (160). Consequently, polymers have been employed to selectively induce nucleation of a particular polymorph (161) and for polymorph screening (162). Conversely, polymers can also be used to inhibit nucleation and maintain a supersaturated solution as in the case of amorphous drug formulations for enhancing the bioavailability of poorly soluble drugs. Drug compounds formulated in the amorphous state do not show the long-range, lattice-like order of normal crystals and therefore have a higher energy crystal structure making them more readily dissolvable in solution (163); (164). This can be useful as a means to increase the bioavailability of poorly soluble drugs by creating a supersaturated state upon dissolution that can greatly enhance the driving force for absorption. A complication that can arise with this method is that upon forming a supersaturated solution, the drug may quickly precipitate out of solution into one of its more stable crystalline forms, thereby losing the benefits gained from amorphous formulation. To prevent this, polymers which act to delay drug precipitation can be added to the formulation (28); (165). Polymeric precipitation inhibitors interact with the drug in such a way to avert precipitation and maintain a supersaturated solution restoring bioavailability. A difficulty in using polymeric precipitation inhibitors is that it is not well understood how polymers act to inhibit nucleation. The solidification outcome is dependent on the molecular and physiochemical properties of the compound of interest and its interaction with the additive, information that is not known a priori, making predicting the crystallization outcome difficult and the selection of polymeric additives largely *ad hoc*. Furthering fundamental understanding on how polymers can have a crystallization inhibiting role and systematically determining which molecular properties influence crystallization tendency of a drug molecule could be of great benefit in streamlining the selection of polymeric additives for the delivery of active pharmaceutical ingredients. The specific interactions between polymeric additives and drug molecules occur on the length scale of a few nanometers or less and therefore experimental observation of these interactions can prove difficult. Additionally, it can be very expensive and time-consuming to test many polymer combinations with the drug of interest. Computer simulation techniques can efficiently probe the nano-scale interactions between drug molecules and a variety of polymers aiding to narrow down the selection process (166). Here we present gauge-cell MC simulations to understand the interactions that occur during drug nucleation from solution in the presence of polymer using first model systems for the promotion and inhibition of nucleation. We subsequently selected the drug felodipine as a case study and explored nucleation of this drug in the presence of either Poly(vinylpyrrolidone) (PVP) or (Hydroxypropyl) methyl cellulose (HPMC).

4.2 Simulation of Drug Nucleation in the Presence of Polymers – The Gauge-Cell Monte Carlo Technique

In this chapter, we aim to simulate drug nucleation from solution in the presence of polymer in order to gain a mechanistic understanding on what polymer properties act to alter the barrier to drug nucleation. For this, we employ the Gauge-cell MC technique (66); (167); (168), which is particularly amenable to this type of system in that it restricts density fluctuations, allowing for the simulation of metastable states such as crystal nuclei below their critical size. Gauge-cell MC is a simulation technique in which the main simulation cell is in equilibrium with several implicit 'gauge' cells, one for each component. This is schematically represented in Fig. 38. Particles in the main cell undergo translation using the standard Metropolis algorithm (Eqn. 3) and there is also exchange of particles between the main cell and their respective gauge cells.

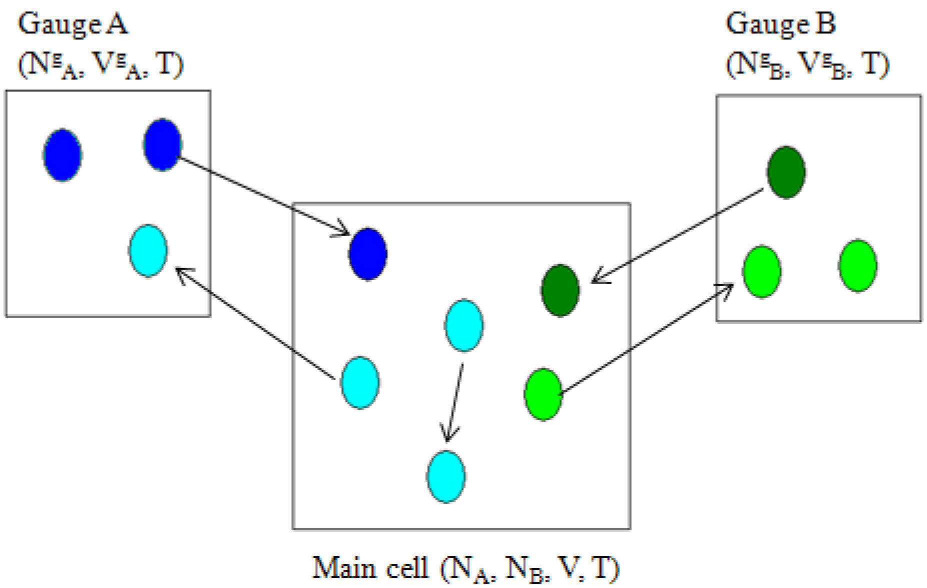

Figure 38: Schematic of the gauge-cell MC technique. The trial MC moves include translation of particles within the main cell, insertion of molecules from the gauge cell into the main cell, and removal of particles from the main cell into the gauge cell.

The gauge cell serves to restrict density fluctuations of a particular component and to measure its chemical potential. The technique was derived with no restrictions on the gauge-cell volume, and as such the volume can be adjusted as the system dictates. In this work, as the interest is in drug nucleation, the drug gauge-cell is of finite size. The solvent is intended to represent bulk water, and no restrictions on the density fluctuations are required. The volume of the solvent gauge-cell is therefore taken to be infinite, resembling Grand Canonical MC for the solvent. For simplicity, because insertion and removal of long-chain polymers is difficult and computationally expensive, the volume of the polymer gauge-cell is chosen to be zero, recovering standard Canonical MC.

4.2.1 Generation of the Isotherm

In a given gauge-cell MC simulation, the result is a histogram of the drug chemical potential around a certain target value. Multiple simulations around different target values (differing amounts of drug in the system) allows one to generate an isotherm, the loading (N) versus the chemical potential (μ). A sample isotherm is shown in Fig. 39. When the concentration of drug in the system is low, it remains in a dispersed state as cluster formation is unfavorable due to the high surface energy of clusters. As more drug molecules are added into the system, small clusters begin to form. These clusters, however, are only metastable and transiently form and melt. When further drug is added, the isotherm passes the spinodal point (the thermodynamic limit of stability and the apex of the isotherm) and drug clusters transition from metastable to stable clusters which can grow in size and eventually transition into a large crystal.

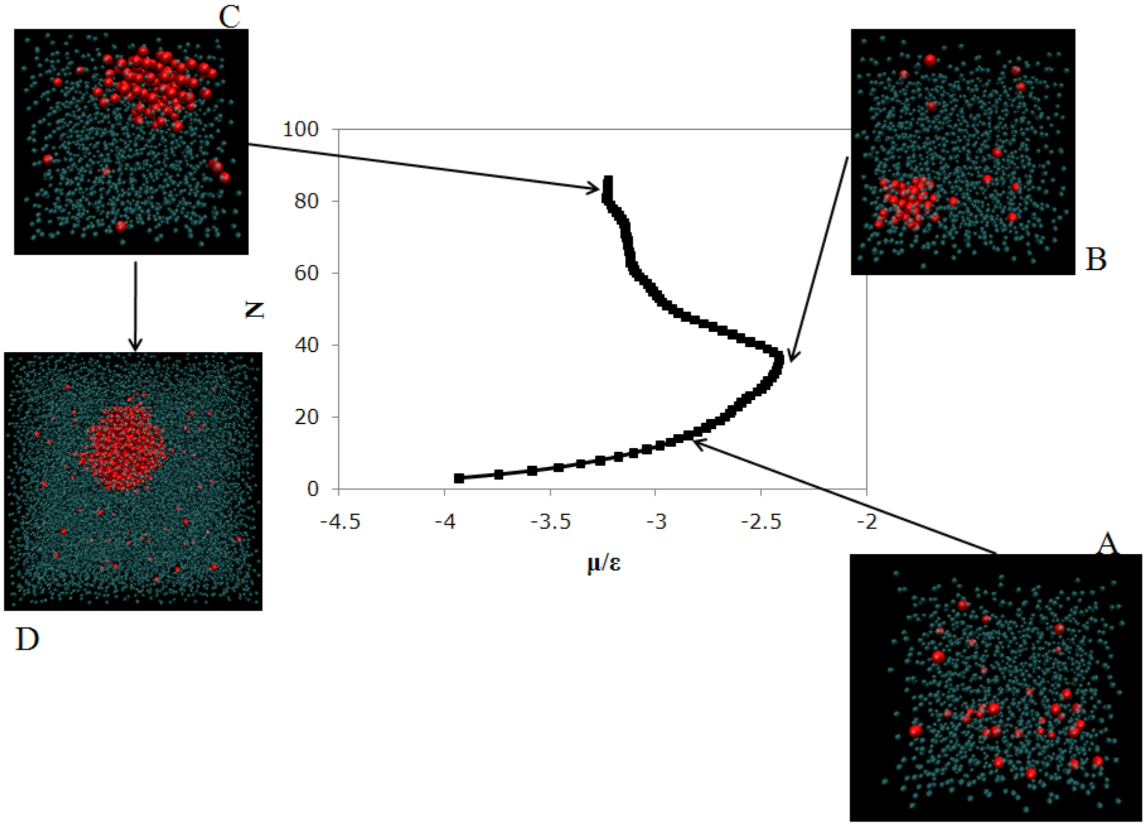

Figure 39: Isotherm resulting from a series of gauge-cell MC simulations with different numbers of drug molecules (N). As one moves up the isotherm, initially the drug is homogenously dispersed in solution as there is not enough drug in the system to form a cluster **(a)**. With the addition of more drug, the spinodal point is reached and a stable cluster can form **(b)**. With increasing N the cluster grows larger **(c)** and into a large crystal **(d)**.

4.2.2 Calculation of the Nucleation Barrier

In transitioning from a dispersed solution to a stable drug cluster, mechanical equilibrium asserts that the chemical potentials of the old phase (dispersed solution) and the new phase (drug nucleus) are equal. The nucleation barrier ($\Delta\Omega$) is defined as the maximum work of cluster formation in transitioning from a dispersed solution to one with a critical nucleus at the same chemical potential μ:

$$\Delta\Omega(\mu) = \Omega_c(\mu) - \Omega_s(\mu) \tag{27}$$

where Ω_c and Ω_s are the grand thermodynamic potentials of the critical cluster state and solution state respectively. Nearer the spinodal, there exist points on the isotherm with equal chemical potential but for which the loading (N) is different. These two points correspond physically to a stable cluster (larger N) and a dispersed solution (smaller N) and the difference between the two is the excess isotherm ΔN for all μ. Thermodynamic integration along the excess isotherm yields the variation in the nucleation barrier for component x according to Eqn. 28 (169):

$$\Delta\Omega = \Delta\Omega_{\mathrm{ref}} - \int_{\mu_{\mathrm{ref}}}^{\mu} \Delta N_x(\mu_x)\,d\mu \tag{28}$$

$\Delta\Omega_{\mathrm{ref}}$ is the nucleation barrier at a certain chemical potential that serves as a reference state. As the free energy is only defined between two states, in order to report the nucleation barrier for a drug at a given chemical potential it would be necessary to determine the nucleation barrier at a known state. Since in this work we are not concerned with reporting the individual nucleation barriers but only the change in the drug nucleation barrier when polymer is added to the system, we can choose $\Delta\Omega_{\mathrm{ref}}$ to be the same both with and without polymer, in which case the reference state would cancel. Thus, using gauge-cell MC the barrier to drug nucleation in the presence of polymer can be calculated and compared to the nucleation barrier in the absence of polymer to determine if addition of polymer will promote (decrease the nucleation barrier) or inhibit (increase the nucleation barrier) nucleation. A schematic of the method used to calculate the nucleation barrier is shown in Fig. 40.

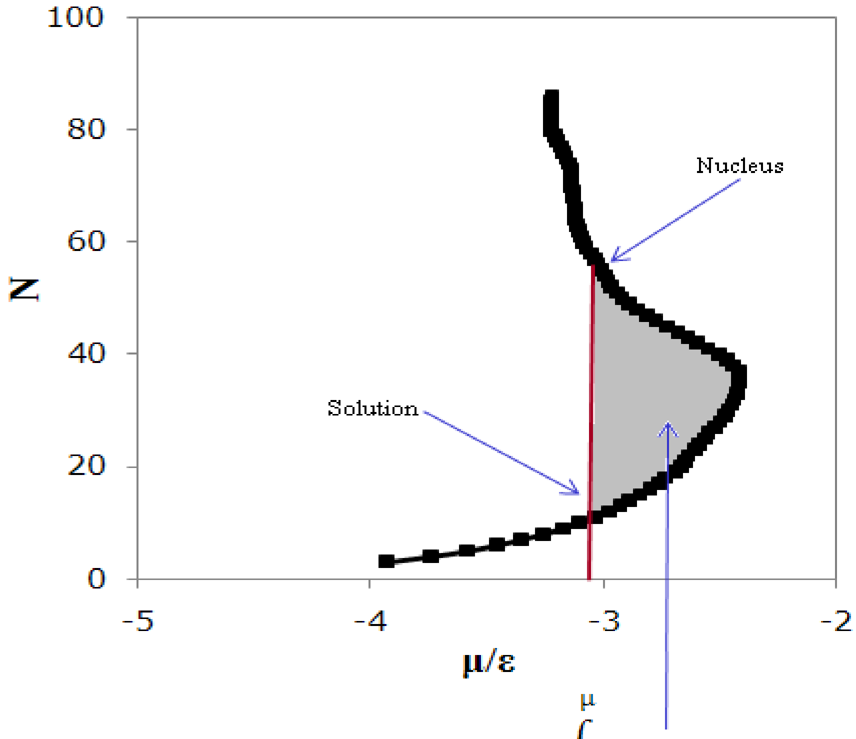

$$\Delta\Omega = \Delta\Omega(\mu_{ref}) - \int_{\mu_{ref}}^{\mu} \Delta N_x(\mu_x)d\mu$$

Figure 40: Schematic of a sample isotherm from a gauge-cell MC simulation, and the method used to calculate the nucleation barrier. The free energy difference between a solution and a system with a crystal nucleus corresponds to the area in gray, calculated using the equation given below the figure.

4.3.1 Simulation Parameters

The aqueous solvent and the drug solute are modeled as Lennard-Jones fluids and the polymers as a Lennard-Jones chain. The interactions between particles are given by Eq. 29:

$$U_{LJ} = \begin{cases} 4\varepsilon_{ij}\left[\left(\frac{\sigma_{ij}}{r}\right)^{12} - \left(\frac{\sigma_{ij}}{r}\right)^{6}\right] & \mathit{for}\ r < r_{cut} \\ 0 & \mathit{for}\ r > r_{cut} \end{cases} \qquad (29)$$

where ε_{ij} is the strength of the interaction, σ_{ij} is the effective diameter of the particle, $r = |r_i - r_j|$ is the distance between particles i and j, and $r_{cut} = 2.5\sigma_{ij}$ is the distance at which the potential is truncated. The particles of the polymer are connected together by a harmonic bond potential of the form:

$$U_b(l) = k_b(l - l_0)^2 \qquad (30)$$

where the bond strength $k_b = 100\ k_BT/\sigma^2$ and the equilibrium bond length l_0 is equal to 1.1σ. The reduced temperature of the system is constant throughout the simulations at 0.85, and the chemical potential of the solvent corresponded to the vapor-liquid coexistence for pure solvent at $k_BT/\varepsilon_{DD} = 0.85$. This implies that the reduction in the chemical potential of the solvent resulting from the presence of solute was neglected. The simulation cell was taken as cubic with between 10 and 30 molecular diameters (σ) per side dependent on the size of the crystal so as to ensure that the crystal did not see its periodic image. The simulations were run for a total of 300 sets with $2\text{x}10^5$ MC steps per set and the first 100 sets taken as equilibration.

4.3.2 Computation of the Chemical Potential and Supersaturation

As mentioned above, the output of a gauge-cell MC simulation is a histogram of the drug chemical potential (for a given N) around a target value. The output histograms contain the best statistics near the target value and as such it was necessary to choose successive simulations such that they had sufficiently overlapping distributions. In most cases this resulted in performing successive simulations while incrementing the number of drug molecules in the system by 5. In the area of the isotherm near the spinodal there is a strong dependence of the chemical potential on the number of molecules in the system, and the number of simulations in this region was increased to obtain better sampling.

The solubility of drug in the system for a particular set of interaction coefficients can be found by simulating a large drug crystal in equilibrium with free drug in solution. A sample configuration of such a system is shown in Fig. 41. In equilibrium, the chemical potential of the two phases (crystal and solution) should be equal, thus by definition the free drug in equilibrium with the crystal is the saturation solubility of the drug, and we can compute the chemical potential of this system. The chemical potential of this large system (μ_∞) can then be related to the system supersaturation using Eqn. 31:

$$S = exp\left(\frac{\mu - \mu_0}{kT}\right) \tag{31}$$

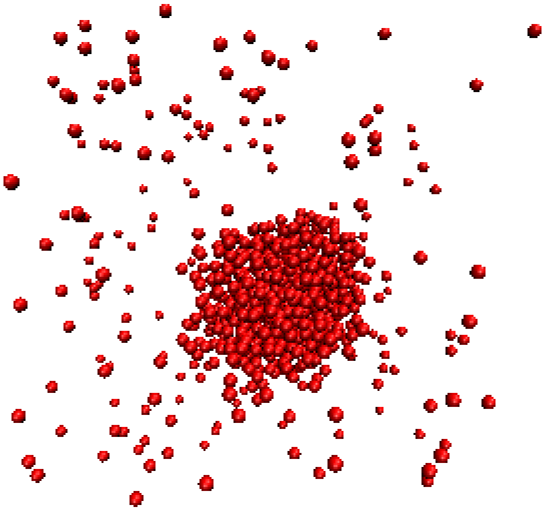

Figure 41: Sample output of a simulation with a large drug crystal in solution with free drug. The chemical potential of this system is the chemical potential of the drug at solubility.

This can be used in conjunction with Eqn. 31 to determine the level of supersaturation when simulating nucleation of a crystal nucleus.

4.3.3 Model Systems for the Promotion and Inhibition of Drug Nucleation

Initial simulations focused on two model systems for the promotion and inhibition of drug crystallization by polymers with the goal of elucidating the specific molecular interactions that give rise to each situation. In general the relative ratio of the different interaction parameters dictates the outcome of the simulation. For example, increasing the propensity for a drug to nucleate from solution could either be done by increasing the affinity of the drug for itself (increasing the drug-drug (ε_{DD}) interaction) or decreasing the affinity of the drug for the solvent (decreasing the drug-solvent (ε_{DS}) interaction). Both instances would lead to preferential segregation of the drug with itself, making a nucleation event more likely. Similarly, increasing the polymer self-interaction (ε_{PP}) while decreasing the polymer interaction with the solvent (ε_{SP}) would induce polymer aggregation. It is worth mentioning that as the polymer is a chain molecule, the Lennard-Jones interactions (Eqn. 29) of each constituent particle in the molecule can be thought to sum, increasing the overall attraction of a polymer molecule to other molecules in the system. This can be exemplified by noting that a given intermolecular interaction necessary to promote favorable self-association of drug molecules would easily lead to very strong self-associations if the same coefficient were used for polymer-polymer interactions (a drug particle has only one other particle to self associate with whereas a polymer molecule has many). Because of this the polymer interaction coefficients are often reduced with respect to the interactions of monomer particles (drug and solvent). In the model simulations there were 9 polymers in the system consisting of 8 particles each.

4.3.3.1 Model System 1: Promotion of Nucleation

Table 6: Bead interaction parameters (ε_{ij}) for model system 1, shown to promote nucleation.

ε_{ij}	**Drug**	**Solvent**	**Polymer**
Drug	1.25 (ε_{DD})	0.60 (ε_{DS})	0.625 (ε_{DP})
Solvent		1.00 (ε_{SS})	0.60 (ε_{SP})
Polymer			0.40 (ε_{PP})

The first model system of interest contained interaction parameters given in Table 6. This system consisted of a hydrophobic drug (poor drug-solvent (ε_{DS}) interaction in relation to the drug-drug interaction (ε_{DD})) and a moderate interaction of the polymer both with the drug and with the solvent. Furthermore, there was a moderate interaction of the polymer with itself. Given in Fig. 42 is the resulting isotherm and calculated nucleation barrier for model system 1. Here, the plots show that the addition of polymer to the system acted to decrease the barrier to drug nucleation. In the absence of polymer, the system could be supersaturated to a maximum value of approximately 4.5 whereas with the addition of polymer this is reduced to ~3. The spinodal (the limit of metastability) occurred for a lower value of N in the presence of polymer than in the absence of polymer indicating that polymer somehow stabilized sub-critical drug clusters causing them to be promoted to critical size. Clusters of this size in the absence of polymer would be below the critical nucleus threshold (Eqn. 25) and likely to melt back into solution, thus indicating that the addition of polymer to the system facilitated nucleation. This can be seen also by examining the computed nucleation barrier in Fig. 42b. For a given supersaturation (i.e. S = 2) adding polymer to the system decreased the drug nucleation barrier by roughly 13 k_BT. To further examine the mechanism by which polymer acted to inhibit nucleation, the system snapshots with and without polymer are shown in Fig. 43. With the parameters used in this system, the polymer acted similar to a surfactant and adsorbed to the surface of a forming drug cluster Fig. 43b. Because the polymer interacted more favorably with the solvent than the drug with the solvent, the polymer facilitated a region of elevated drug concentration shielding the drug from unfavorable solvent interactions. This can be seen in the system snapshots of Fig. 43 which clearly show the polymer molecules wrapped around the forming drug cluster. Adsorption of polymer onto the surface of forming drug clusters allowed for a decrease in the unfavorable drug-solvent interactions on the cluster surface (decreasing the surface term in Eqn. 19) allowing for favorable free energies of cluster formation at smaller cluster sizes. Therefore, we found that to promote nucleation of a particular drug in the presence of polymer, it is necessary that the polymer have a favorable interaction with both the drug and the solvent. In this way, the drug will cluster around the polymer to shield itself from unfavorable interactions with the solvent. This causes an elevated region of drug concentration, increasing molecular collisions, and facilitating nucleation. Additionally, polymer adsorbing to the surface of growing drug clusters reduces the unfavorable interactions between the cluster surface and the solvent, allowing drug clusters to become critical nuclei at smaller sizes.

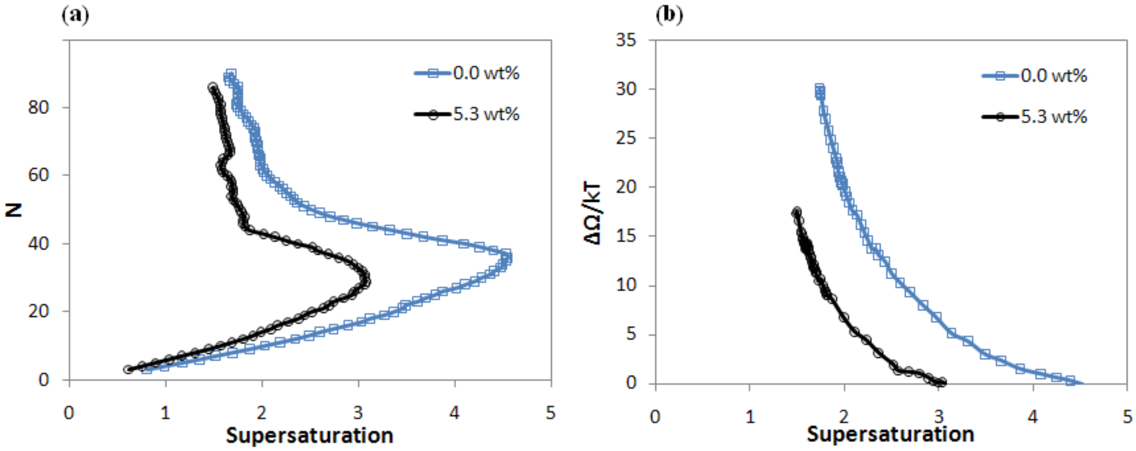

Figure 42: Simulation results for model system 1. **(a)** Isotherm of a nucleating system in the absence of polymer (0.0 wt%) and in the presence of polymer (5.3 wt%) **(b)** The calculated nucleation barrier as a function of supersaturation.

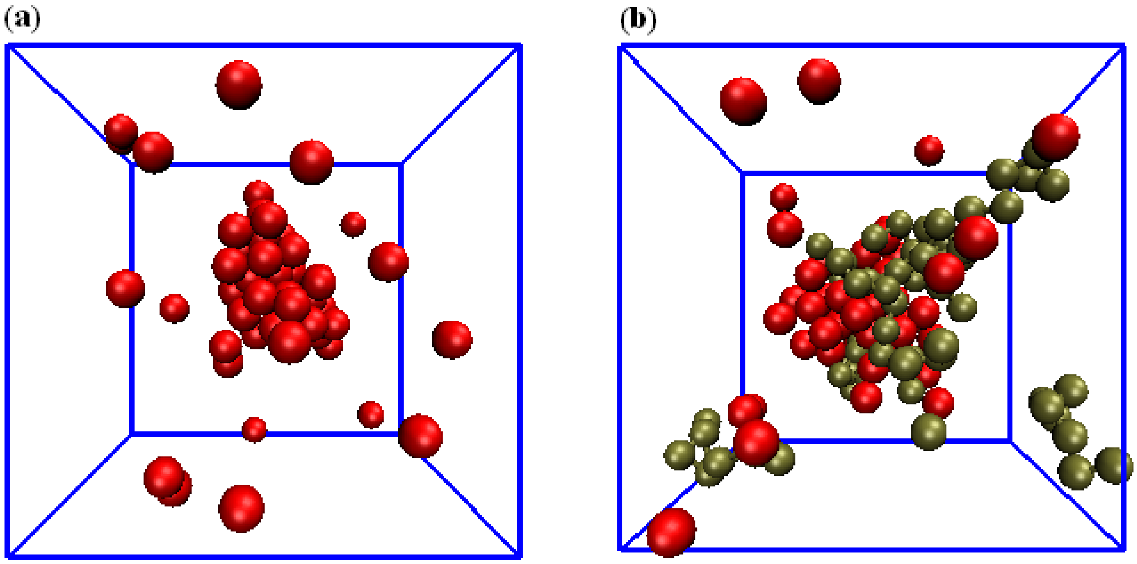

Figure 43: Snapshots corresponding to the systems shown in Fig. 42 for N = 48 drug molecules in the system. **(a)** System with 0.0 wt.% polymer and **(b)** 5.3 wt.% polymer. Drug particles are shown in red and polymer molecules are shown in gold. Solvent has been removed for clarity.

4.3.3.2 Model System 2: Inhibition of Nucleation

The second model system of interest concerned polymers that act to inhibit drug nucleation from solution by increasing the nucleation barrier. In such a system the interaction was strong between the drug and polymer which increased drug-polymer associations. The interaction of the polymer with the solvent was similarly strong, but the interaction of the polymer with itself was weak (compared to the polymer-drug interaction). This allowed for the polymer to maintain an extended conformation within the solvent and decreased polymer-polymer associations. The aim of this was for the drug to interact strongly with the polymer, but reduce drug-drug contacts due to decreased polymer self-association. An additional variation included in this model system was to augment the molecular size of the polymer particles (σ-parameter) relative to that of the drug. For this we kept the molecular size of the drug at $\sigma = 1.0$ and increased the polymer molecular size to $\sigma = 1.1$. The bead-bead interaction parameters are shown below in Table 7.

Table 7: Bead interaction parameters (ε_{ij}) for model system 2, shown to inhibit nucleation.

ε_{ij}	**Drug**	**Solvent**	**Polymer**
Drug	1.20 (ε_{DD})	0.60 (ε_{DS})	2.0 (ε_{DP})
Solvent		1.0 (ε_{SS})	2.0 (ε_{SP})
Polymer			0.1 (ε_{PP})

The simulation results of model system 2 are shown in Fig. 44. The isotherms show that in the absence of polymer the metastable limit occurred at a supersaturation of 3.75 and with 67 molecules in the system. This is compared with the addition of 2.6 wt.% polymer (model systems 1 and 2 has the same number of polymers, but the system size was increased in model system 2 decreasing its relative wt.%) which showed a maximum supersaturation of 3.0 and a metastable limit of N = 83. The decrease in maximal supersaturation signified that adding polymer having the interaction parameters of Table 7 to the system caused the solubility of the drug to increase thereby lowering the maximum supersaturation. The increase in the number of molecules in the system at the spinodal point indicated that the polymer decreased the stability of the critical nucleus requiring it to be of larger size before it became thermodynamically stable. In examining the nucleation barrier (Fig. 44b), for high supersaturation the addition of polymer showed a barrier roughly equivalent to that of the no polymer case however, at lower supersaturation the addition of polymer to the system increased the nucleation barrier, inhibiting nucleation. The strong interaction of the drug with the polymer resulted in drug molecules closely associating with the polymer and reduced the probability of drug molecules interacting with themselves. In addition, the difference in the molecular size between the drug and polymer resulted in the polymer disrupting the periodic lattice of the drug molecules, further decreasing the tendency of the drug to nucleate (170). This can be seen in the system snapshots below (Fig. 45) in which the system without polymer showed a clear nucleus (Fig. 45a) whereas a nucleus was absent from the system containing 2.6 wt.% polymer. Therefore, using the polymer parameters given in Table 7 we have inhibited nucleation of a model drug system finding that the key polymer properties were a strong interaction with both the drug and the solvent, and the polymer must have a molecular size that was incommensurate with the forming lattice stricture of the drug.

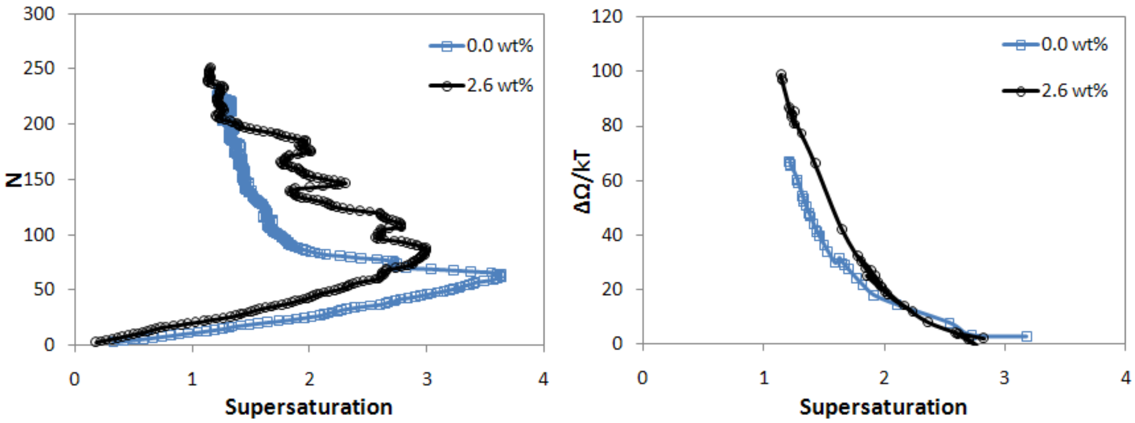

Figure 44: Simulation results for model system 2. **(a)** Isotherm of a nucleating system in the absence of polymer (0.0 wt%) and in the presence of polymer (2.6 wt%) **(b)** The calculated nucleation barrier as a function of supersaturation.

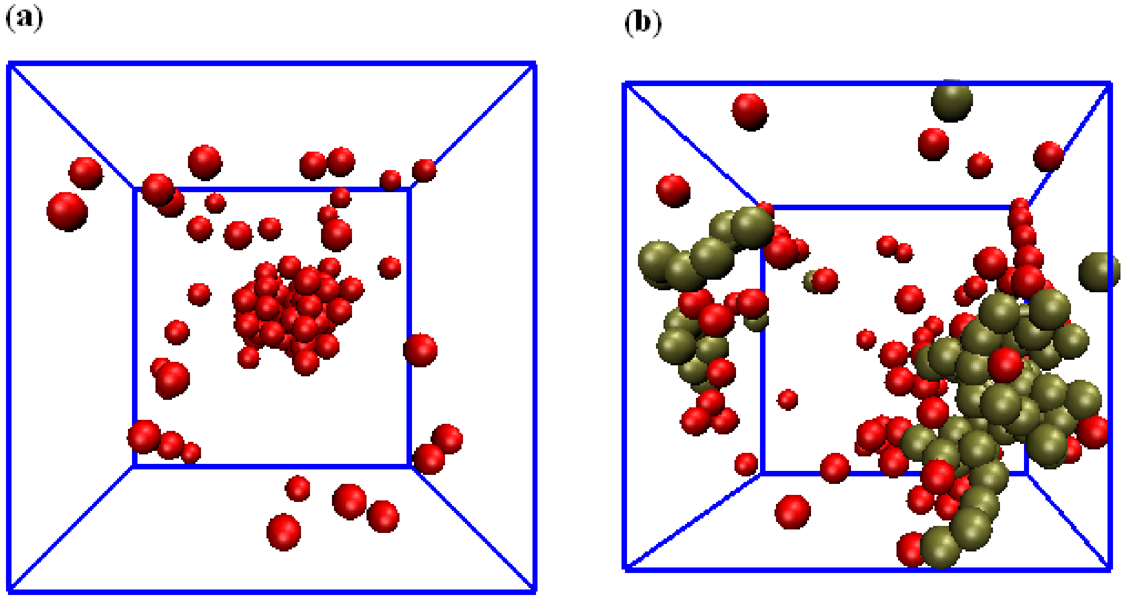

Figure 45: Snapshots corresponding to the systems shown in Fig. 44 with N = 91 drug molecules in the system. **(a)** System with 0.0 wt.% polymer and **(b)** 5.3 wt.% polymer. Drug particles are shown in red and polymer molecules are shown in gold. Solvent has been removed for clarity.

In summary, we formulated two model systems for the nucleation of drug molecules in the presence of polymer with differing effects. We have shown that if the interaction of the polymer with both the drug and solvent was of moderate strength, the polymer acted like a surfactant, adsorbing to the surface of growing drug clusters increasing their stability and allowing for their promotion to critical clusters (171) at smaller size thus facilitating nucleation. Additionally we have found that if nucleation inhibition is desired, a strong interaction of the polymer with the drug was required as well as the polymer having a molecular structure that was mismatched with the periodic structure of the forming drug lattice. Using the knowledge gained from the results of model drug-polymer systems, we now formulate a molecular simulation platform to explore nucleation in real systems, specifically nucleation of the drug felodipine in the presence of either the polymer PVP or HPMC.

4.3.4 Nucleation of Felodipine in the Presence of PVP or HPMC

With understanding gained from the model systems, we explored nucleation in specific, real systems for which there exist experimental data on the influence of polymer on drug nucleation. The drug felodipine is a calcium channel agonist used to treat hypertension. It is a class II compound as classified by the Biopharmaceutics Classification System (BCS) in that it has low solubility and high permeability (172) and as such could benefit greatly from alternative formulations such as fabrication as an amorphous crystal (173). This makes felodipine a good model compound for the study of nucleation inhibition by polymeric precipitation inhibitors. Studies of felodipine nucleation in the presence of HPMC have indicated that HPMC is able to substantially delay drug nucleation (25); (174). Work by Alonzo (171) showed that felodipine nucleation induction time (time from the onset of nucleation to the time at which the first appreciable crystals are detected) increased to 135.5 minutes in the presence of HPMC compared to 15.3 minutes for the amorphous crystal alone. Studies of felodipine nucleation in the presence of PVP have also been performed with the results a bit less clear. Konno et al. (25) performed nucleation experiments and found that PVP did in fact delay nucleation of felodipine, but in a similar study Vogt et al. (175) found PVP to have no influence on the nucleation kinetics of felodipine. This discrepancy lends to the idea that the mechanisms by which polymers act to inhibit nucleation are not well understood and further fundamental study is required before predictive models of the optimal polymeric precipitation inhibitor for a given drug are available. In the remainder of this chapter, we use MD simulations in conjunction with the gauge-cell MC technique to explore nucleation of felodipine in the presence of HPMC and PVP.

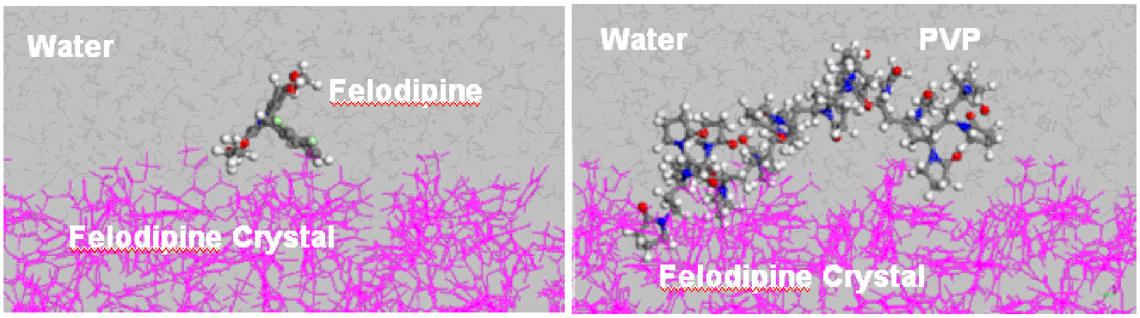

Figure 46: Snapshots of the MD simulations used to calculate the binary binding energies of the system components used to parameterize the gauge-cell MC simulations showing the interfacial binding of a felodipine molecule (Left) and PVP (Right) to crystalline felodipine.

4.3.4.1 Molecular Dynamics Simulations for Parameter Estimation

The gauge-cell MC simulation that we performed in our model systems is a CG approach to explore the molecular mechanisms of crystal nucleation in the presence of additives. In order to perform nucleation simulations on specific compounds, we need a way to translate the detailed molecular properties of said compounds into our gauge-cell MC system. To obtain the interaction parameters for the gauge-cell MC simulation, we performed atomistic MD simulations of the specific polymer/water/drug system. Representative snapshots of these simulations are shown in Fig. 46. The MD simulations contained crystalline felodipine in full atomistic detail as well as water and the polymer of interest (either PVP or HPMC). Simulating the binary interaction between the system components (i.e. felodipine – water, PVP – felodipine, etc.) allowed us to extract parameters by calculating the binding energies per unit area of each component combination. We then used the ratio of the calculated binding energies to compute the Lennard-Jones coefficients in the gauge-cell MC simulation. The MD simulations were performed with Materials Studio Modeling 3.1 package from Accelrys which employs the COMPASS (Condensed-phase Optimized Molecular Potential for Atomistic Simulation Studies) force-field (176). The simulations were run for 300 ps each and the interfacial binding energies were calculated over the last 200 ps of simulation time according to Eqn. 32. The interfacial binding energies ($E_{Binding}$) can be calculated using Eqn. 32:

$$E_{Binding} = E_{Total} - \sum_i E_i \tag{32}$$

where E_{Total} is the potential energy of the two component complex (ie drug-polymer, drug-solvent, etc) and E_i is the potential energy of each component alone. Simulations were run on felodipine crystal surfaces [100], [001], and [010] for each combination involving felodipine and we computed an average overall binding energy. Sample plots of the binding energies for two combinations (water and felodipine, polymer and felodipine) are shown in Fig. 47. All average binding energies were then normalized per unit area using the projected area of one component on the other (i.e. water molecule on a felodipine crystal). The per-unit-area binding energies were all normalized to the water-water binding energy (taken as 1.0 in our gauge-cell MC simulations) and the ratio of these parameters were used to calculate the CG interaction parameters in our MC simulations.

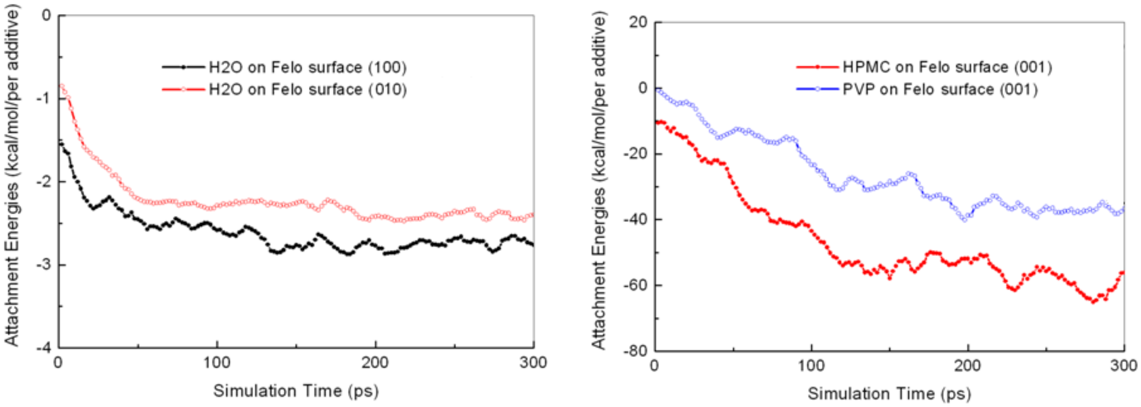

Figure 47: Results of atomistic MD data for two sample component combinations: water with felodipine (Left) and polymer with felodipine (Right).

4.3.4.2 Nucleation of Felodipine in the Presence of PVP

Experimentally, it has been shown that PVP can act to delay crystal nucleation (25) yet there exist other studies which have found that PVP has no influence on crystal nucleation (175). Thus, to understand what may be occurring on a molecular level, we simulated nucleation of felodipine in the presence and absence of PVP. To determine the interaction parameters for the gauge-cell MC simulation, it was first necessary to perform atomistic MD simulations of the relative binding energies between the system components. The atomistic MD simulations were performed, and the average binding energies between the system components were calculated using Eqn. 32. The results are summarized in Table 8. As stated above, the results were normalized to the water-water binding energy, and the resultant interaction parameters for the gauge-cell MC simulation of felodipine – PVP – water are given in Table 9.

Table 8: Results of MD simulation of binding energy for felodipine – PVP – water.

Felodipine – PVP – Water	**Average Binding Energy (kcal/mol/nm^2)**		
	Water	**Felodipine**	**PVP**
Felodipine [100]	-27 ± 1	-33 ± 1	-38 ± 1
Felodipine [010]	-25 ± 1	-40 ± 1	-38 ± 1
Felodipine [001]	-26 ± 1	-19 ± 1	-39 ± 1
PVP - Water	-41.3 kcal/mol/nm^2		

Table 9: Lennard-Jones coefficients used in the felodipine – PVP – water gauge-cell MC simulations

ε_{ij}	**Drug**	**Solvent**	**Polymer**
Felodipine	0.76 (ε_{DD})	0.54 (ε_{DS})	0.80 (ε_{DP})
Water		1.00 (ε_{SS})	0.86 (ε_{SP})
PVP			0.20 (ε_{PP})

In comparison to the model systems, there was a moderately strong interaction of the polymer with both the drug and the solvent similar to model system 1, but the drug-drug interaction strength was lower. We performed the MC simulation using these coefficients, and the resulting isotherm and nucleation barrier are given in Fig. 48. As shown by the isotherms, PVP did not show any effect on nucleation of felodipine. Similarly, the computed nucleation barriers for a system containing PVP did not show any differences from the case of nucleation of felodipine alone. Additionally, the system snapshots show that when the number of molecules in the system is 90 (slightly above the metastable limit), a nucleus has formed in both the systems with and without polymer (Fig. 49). Interestingly, the snapshot of the system containing PVP does not show much interaction of PVP with felodipine molecules, which is likely the reason that there was no effect of PVP on felodipine nucleation.

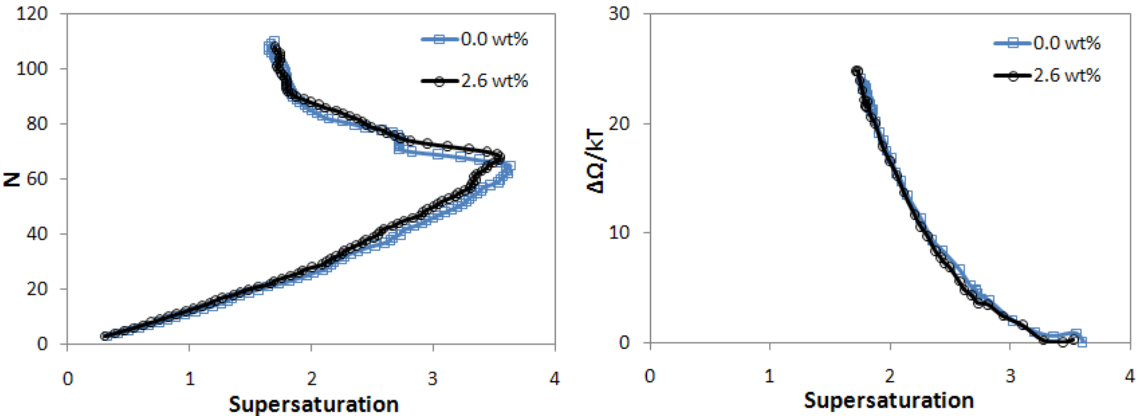

Figure 48: Gauge-cell simulation results of nucleation in a felodipine-PVP-water system. **(a)** Isotherm and **(b)** nucleation barrier.

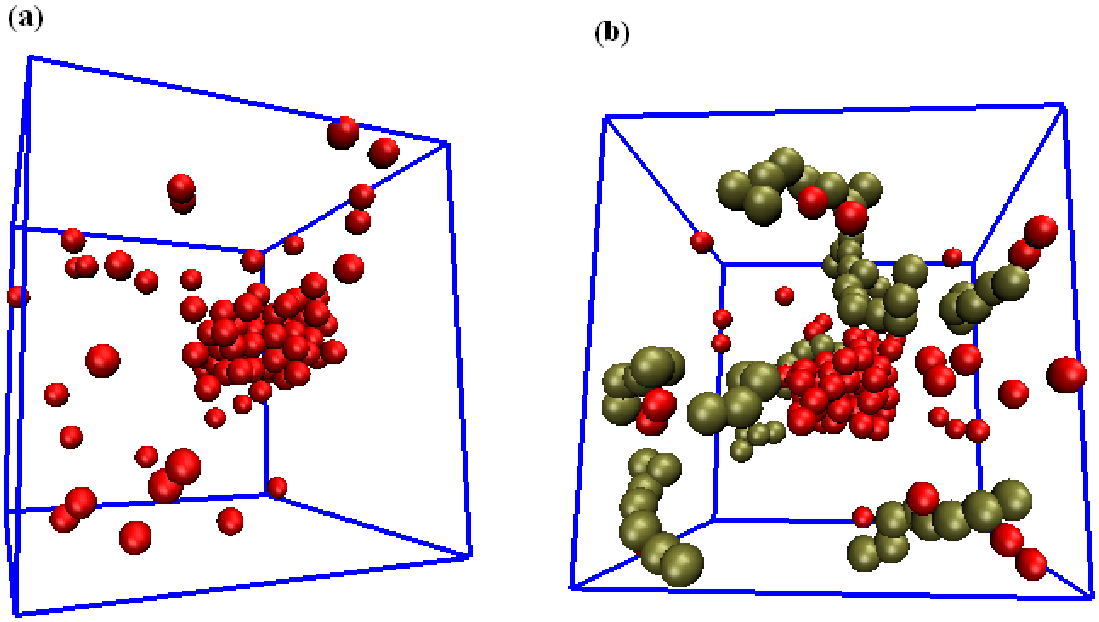

Figure 49: Snapshots of the felodipine – PVP – water system corresponding to Fig. 48 with N = 90 drug molecules in the system. **(a)** System with 0.0 wt.% PVP and **(b)** 2.6 wt.% PVP. Drug particles are shown in red and polymer molecules are shown in gold. Solvent has been removed for clarity.

4.3.4.3 Nucleation of Felodipine in the Presence of HPMC

Following PVP, we also examined the influence of HPMC on felodipine nucleation, which has been experimentally shown to decrease the nucleation rate (increase the nucleation barrier), (174). As in the prior section with PVP, the initial step was to perform atomistic MD simulations of the binary binding energies between the various components of the system. The results of the MD simulations are shown below in Table 10. In addition to binding energy calculations, we also calculated the solvent accessible surface area (SASA) of an HPMC monomer and of felodipine to obtain the relative sizes between the two components. Assuming that a felodipine molecule and an HPMC monomer can be modeled as a sphere, the SASA calculations yield that the molecular size of HPMC was 10% greater than that of felodipine. Using the results of the MD simulations, we computed the Lennard-Jones coefficients for use in the gauge-cell MC simulations of felodipine-HPMC-water with the additional parameter change of: $\sigma_{polymer} = 1.1\sigma_{drug}$. The resultant interaction parameters for the gauge-cell MC simulation are given in Table 11.

Table 10: Results of MD simulations of binding energy for felodipine – HPMC – water

Felodipine – HPMC – Water	**Average Binding Energy (kcal/mol/nm^2)**		
	Water	**Felodipine**	**PVP**
Felodipine [100]	-28 ± 1	-33 ± 1	-23 ± 1
Felodipine [010]	-25 ± 1	-40 ± 1	-16 ± 1
Felodipine [001]	-26 ± 1	-19 ± 1	-15 ± 1
PVP - Water	-26 ± 1 kcal/mol/nm^2		
Species	**Solvent Accessible Surface Area (nm^2)**		
HPMC (monomer)	6.59		
Felodipine	5.57		

Table 11: Lennard-Jones coefficients used in the felodipine – HPMC – water gauge-cell MC simulations

ε_{ij}	**Drug**	**Solvent**	**Polymer**
Felodipine	0.55 (ε_{DD})	0.46 (ε_{DS})	0.32 (ε_{DP})
Water		1.00 (ε_{SS})	0.20 (ε_{SP})
PVP			0.21 (ε_{PP})

In performing the nucleation simulations with felodipine and HPMC, we found that in the case in which 7.0 wt.% polymer was added to the system HPMC completely inhibited nucleation (Fig. 50) up to a maximum system size of N = 400 felodipine molecules. The isotherm of Fig. 50 for the no polymer case shows a clear spinodal point, indicating that a nucleus has formed, yet for the case with 7.0 wt.% HPMC the spinodal is absent. As we did not observe nucleation in the case with 7.0 wt.% HPMC, we were not able to calculate a change in the nucleation barrier for the polymer – no polymer difference. We can, however, make comparisons with model system 2 in which an increase in the nucleation barrier was found. In both systems, there was a stronger interaction between the polymer and drug than the polymer with itself ($\varepsilon_{DP} > \varepsilon_{PP}$). This is necessary because a large polymer self-interaction results in the polymer forming into a globule and thus minimizing the possible interactions with the drug. Additionally, both systems (felodipine-HPMC-water and model system 2) included a polymer with a molecular size that was larger than the drug molecular size. When a drug crystallite begins to form, the molecules align in a regular lattice-like array. If the incoming polymer has a molecular size (or structure) that is similar to that of the drug, it can easily be incorporated into the growing crystal lattice. However, if the interaction of the polymer with the drug is strong, but the polymer has a molecular size which differs from that of the drug, the polymer acts to disrupt the periodicity of the forming nucleus, leading to nucleation inhibition.

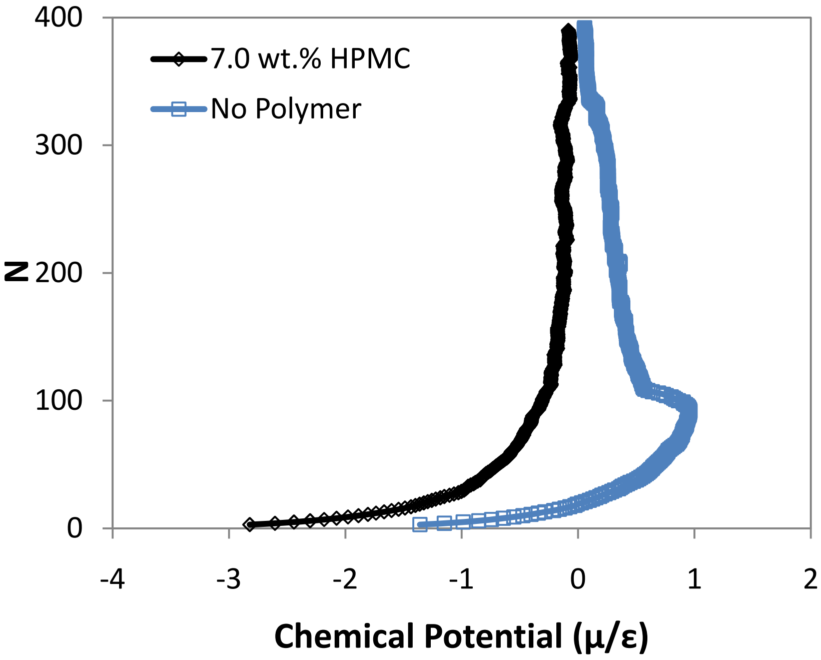

Figure 50: Computed isotherm of the felodipine-HPMC-water system showing the case with 0.0 wt% HPMC and 7.0 wt.% HPMC. In this system we did not find nucleation in the presence of HPMC and thus a nucleation barrier was not calculated.

4.4 Conclusions of Pharmaceutical Nucleation in the Presence of Polymer

In this chapter, we used molecular simulation techniques to determine the influence of polymer on drug nucleation in two model cases and two real cases. In the model cases, it was found that polymer could act to either increase or decrease the barrier to drug nucleation, dependent on the specific interactions in the system. It was determined that when the polymer had favorable interaction with both the drug and the solvent, the polymer acted to adsorb to the surface of the growing drug clusters and shield them from the unfavorable interactions with the surrounding solvent. This acted to allow the clusters to become stable at smaller sizes, effectively promoting nucleation. In order to delay nucleation, it was found that there needed to be a strong interaction of the polymer with the drug, but a major factor was the relative molecular sizes of the polymer and drug. When the sizes between the polymer and the drug were incommensurate, the polymer could still adsorb to the surface of growing drug clusters, however, the polymer could not easily be incorporated in the drug crystal lattice. This acted to disrupt the periodicity of the emerging nucleus and made it less favorable for nucleation to occur. In addition to the model systems, we also explored two real systems: felodipine-PVP-water and felodipine-HPMC-water. Our results coincide with experiment in that PVP did not act to either increase or decrease the nucleation barrier of felodipine. HPMC, on the other hand, completely inhibited nucleation of felodipine in our simulations. This is in accord with experiments which show that HPMC is effective in delaying the onset of felodipine nucleation compared to felodipine nucleation in the absence of polymer.

Chapter 5 Conclusions and Future Work

In the preceding chapters we have employed a variety of molecular simulation techniques to probe the specific interactions that occur between nanoparticles, surfactants, and polymers to gain insight into the molecular interactions that give rise to macroscopic phenomena in a series of three case studies. We first applied MD simulation to analyze the energy necessary to rupture a lipid bilayer under tension and shear and compared that to the energy a magnetic nanoparticle could generate in fields typically used for MFH. We expanded upon this idea by using DPD simulation to explore a larger bilayer system and the influence of a model magnetic nanoparticle coating (PEO-PEE) on bilayer rupture. The influence of different polymer properties on bilayer rupture energy were investigated, and based on the results we suggested an optimal combination of polymer properties for enhancement of bilayer rupture. The second case study of this thesis was concerned with revealing the molecular mechanisms behind NLBs fabricated to block the uptake of oxidized LDL by macrophage SR-A. We parameterized a CG model of four selected NLBs varying in charge, charge location, and the ability to form micelles, and studied their interaction with the binding domain of SR-A. We measured the number of contacts that the different NLBs formed with SR-A as a means of assessing their relative affinities for the protein. This was compared to experimental results to explore how the variation in NLB architecture affects their quality as inhibitors to oxidized LDL uptake. Finally, we applied gauge-cell MC and MD simulations to a pharmaceutical case study to investigate the mechanisms by which polymeric additives influence nucleation of drugs from solution. We studied both model and real systems to first: gain a generalized molecular and thermodynamic understanding of the means by which polymers act to alter drug nucleation from solution, and second: to understand experimental observations why certain a certain polymer (HPMC) is able to inhibit nucleation of amorphous felodipine whereas PVP is not. In general, we have been able to implement a multitude of computational simulation techniques to gain insight into the molecular phenomena that govern selected biomedical and pharmaceutical phenomena. The remainder of this chapter will go into further detail of the specific conclusions of each case study as well as suggestions for future work.

5.1 Energetics of Cell Membrane Rupture by Magnetic Nanoparticles in Magnetic Fluid Hyperthermia

Chapter 2 modeled two plausible mechanisms for producing cell membrane rupture during MFH with the goal of estimating the energies needed to rupture a lipid bilayer in both the presence and absence of polymer. Simulations of membrane rupture via incremental shear stress yielded a value for the surface tension of the bilayer equal to 84 mN m^{-1} which equates to a rupture energy of $6.3x10^{-2}$ J m^{-2}. The results were consistent with previous studies for similar systems which used different methodologies of producing membrane rupture. Comparison to conditions representative of experimental MFH studies, our simulations yielded a nanoparticle diameter of 80 nm necessary to produce bilayer rupture. This is 5 to 10 times larger than typical particle diameters used in MFH, however a particle size of 80 nm is plausible for biomedical applications, in which the widely accepted upper limit is between 100 and 200 nm. Considering that our simulations represent an upper bound to the rupture energy due to increased stability of the nanoscale size (40 nm^2) of our system, the force and the energy necessary to rupture real cells *in vivo* may be lower bringing the estimated particle size nearer to those used in experiment. Furthermore, we also simulated bilayer rupture in the presence of a generic magnetic nanoparticle polymer coating (PEO-PEE) to determine its influence on the rupture energy. We found that polymers that enhance rupture are shorter with a hydrophobic-hydrophilic-hydrophobic block structure and a high hydrophilic content. In performing our analysis, we determined that the rupture energies obtained here provide good agreement with the size of magnetic nanoparticles generally used in MFH indicating it is likely that magnetic nanoparticles are capable of enhancing rupture of a cell membrane, and choice selection of the nanoparticle coating properties could result in more effective MFH treatment at reduced, less harmful magnetic fields.

Future work in the area would include increasing the complexity of the system to better model a realistic natural environment. Cell membranes are much more complicated than the simple lipid bilayer system simulated here. For example, cellular membranes *in vivo* contain a significant amount of cholesterol, which acts to order the lipids resulting into a more solid-like membrane. Similarly, cellular membranes also contain several types of lipids, proteins, and surface attached carbohydrates, all of which might be good nucleating sites for pore formation. Moreover, the addition of ions to the system to simulate the chemical and electrical potential gradient that is present across all cells could have an impact on membrane rupture, for it is the loss of an ion gradient that will ultimately lead to the death of a cell.

5.2 Engineered Macromolecules as Inhibitors to Oxidized Low Density Lipoprotein by Macrophage Scavenger Receptors: Simulation of Structure – Function Relationships

Chapter 3 utilized CG MD simulations to study the interaction between engineered macromolecules designed to block the uptake of oxidized LDL by SR-A. In our simulations 0CM, 1CM, and 1CP NLBs formed into micelles within 300 ns with the largest micelles consisting of 10 to 11 NLB molecules with a micelle radius of 3.8 – 6.4 nm while PEG-COOH did not form micelles in agreement with experiential observations. Interaction studies between NLBs and SR-A showed that 1CM, 1CP, and 0CM NLBs interacted with SR-A as micellular aggregates while PEG-COOH interacted as single monomers indicating that micellization is likely a necessary feature for effective inhibition of oxidized LDL uptake. As an indirect assessment of binding affinity, we identified the number of contacts that each type of NLB made with SR-A both at 0.8 nm and 2.0 nm from the receptor. The number of close contacts (< 0.8 nm) were similar for each NLB, but aligned with experimental trends showing 1CM and 1CP good inhibitors of oxidized LDL uptake while PEG-COOH was the worst. Extending the contact cutoff to 2.0 nm provided the conclusion that 1CM showed the greatest ability to sterically block the entire binding domain from LDL particles. Finally, in calculating the specific contacts between the charged portions of NLBs and the binding pocket of SR-A indicated that the addition of a negative charge on the PEG tails of NLBs did not act to enhance interaction with the important residues of the SR-A, however an anionic charge at the NLB head increased interaction with the positively charged residues of the binding pocket, confirming the experimental finding that 1CM is the best inhibitor to oxidized LDL uptake as it most strongly associates with SR-A.

5.3 Pharmaceutical Nucleation in the Presence of Polymeric Additives

Chapter 4 used MC and MD simulation techniques to determine the influence of polymer on drug nucleation in two model cases and two real cases. In the model cases, it was found that polymer could act to either increase or decrease the barrier to drug nucleation, dependent on the specific interactions in the system. When the polymer had favorable interaction with both the drug and the solvent, the polymer preferentially adsorbed to the surface of the growing drug clusters, shielding them from the unfavorable interactions with the surrounding solvent. This allowed the clusters to become stable at smaller sizes, decreasing the nucleation barrier and promoting nucleation. When there was a strong interaction of the polymer with the drug and a size mismatch between the drug and polymer components, the result was an increase in the nucleation barrier. This acted to disrupt the periodicity of the emerging nucleus and made it less favorable for nucleation to occur. In addition to model systems, we also explored two real systems for which experimental nucleation data exists: nucleation of the drug felodipine in the presence of the polymers PVP or HPMC. Our results coincide with experiment in that PVP did not have any effect of increasing or decreasing the nucleation barrier of felodipine. HPMC on the other hand, completely inhibited nucleation of felodipine in our simulations. This is in accord with experiments which show that HPMC is effective in delaying the onset of felodipine nucleation compared to felodipine nucleation in the absence of polymer.

References

1. Whitesides GM. The 'right' size in nanobiotechnology. *Nat Biotechnol*. 2003; 21(10): p. 1161-1165.
2. Bhushan B. Springer Handbook of Nanotechnology New York: Springer-Verlag; 2006.
3. Muller RH, Keck CM. Challenges and solutions for the delivery of biotech drugs--a review of drug nanocrystal technology and lipid nanoparticles. *J Biotechnol*. 2004; 113(1-3): p. 151-170.
4. Bharali DJ, Khalil M, Gurbuz M, Simone TM, Mousa SA. Nanoparticles and cancer therapy: a concise review with emphasis on dendrimers. *Int J Nanomedicine*. 2009; 4: p. 1-7.
5. Liversidge GG, Cundy KC. Particle size reduction for improvement of oral bioavailability of hydrophobic drugs: I. Absolute oral bioavailability of nanocrystalline danazol in beagle dogs. *Int J Pharm*. 1995; 125(1): p. 91-97.
6. Berber S, Kwon YK, Tomanek D. Unusually high thermal conductivity of carbon nanotubes. *Phys Rev Lett*. 2000; 84(20): p. 4613-4616.
7. Bruchez Jr M, Moronne M, Gin P, Weiss S, Alivisatos AP. Semiconductor nanocrystals as fluorescent biological labels. *Science*. 1998; 281(5385): p. 2013-2016.
8. Pankhurst QA, Tanh NTK, Jones SK, Dobson J. Progress in applications of magnetic nanoparticles in biomedicine. *J Phys D: Appl Phys*. 2009; 42(22): p. 224001.
9. Medintz IL, Uyeda HT, Goldman ER, Mattoussi H. Quantum dot bioconjugates for imaging, labelling and sensing. *Nat Mater*. 2005; 4(6): p. 435-446.
10. Thorek DL, Chen AK, Czupryna J, Tsourkas A. Superparamagnetic iron oxide nanoparticle probes for molecular imaging. *Ann Biomed Eng*. 2006; 34(1): p. 23-38.
11. Harrison BS, Atala A. Carbon nanotube applications for tissue engineering. *Biomaterials*. 2007; 28(2): p. 344-353.
12. Kawasaki ES, Player A. Nanotechnology, nanomedicine, and the development of new, effective therapies for cancer. *Nanomedicine*. 2005; 1(2): p. 101-109.
13. Ibrahim NK, Desai N, Legha S, Soon-Shiong P, Theriault RL, Rivera E, et al. Phase I and pharmacokinetic study of ABI-007, a Cremophor-free, protein-stabilized, nanoparticle formulation of paclitaxel. *Clin Cancer Res*. 2002; 8(5): p. 1038-1044.
14. Harris LA, Goff JD, Carmichael AY, Riffle JS, Harburn JJ, St. Pierre TG, et al. Magnetite Nanoparticle Dispersions Stabilized with Triblock Copolymers. *Chem Mater*. 2003; 15(6): p. 1367-1377.
15. Willard MA, Kurihara LK, Carpenter EE, Calvin S, Harris VG. Chemically prepared magnetic nanoparticles. *Int Mater Rev*. 2004; 49(3-4): p. 125-170.
16. Studart AR, Amstad E, Gauckler LJ. Colloidal stabilization of nanoparticles in concentrated suspensions. *Langmuir*. 2007; 23(3): p. 1081-1090.
17. Jorgensen WL. The many roles of computation in drug discovery. *Science*. 2004; 303(5665): p. 1813-1818.

18. Izvekov S, Violi A, Voth GA. Systematic coarse-graining of nanoparticle interactions in molecular dynamics simulation. *J Phys Chem B*. 2005; 109(36): p. 17019-17024.
19. Surve M, Pryamitsyn V, Ganesan V. Nanoparticles in solutions of adsorbing polymers: pair interactions, percolation, and phase behavior. *Langmuir*. 2006; 22(3): p. 969-981.
20. Lipinski CA. Drug-like properties and the causes of poor solubility and poor permeability. *J Pharmacol Toxicol Methods*. 2000; 44(1): p. 235-249.
21. Müller RH, Jacobs C, Kayser O. Nanosuspensions as particulate drug formulations in therapy. Rationale for development and what we can expect for the future. *Adv Drug Deliv Rev*. 2001; 47(1): p. 3-19.
22. Merisko-Liversidge E, Liversidge GG, Cooper ER. Nanosizing: a formulation approach for poorly-water-soluble compounds. *Eur J Pharm Sci*. 2003; 18(2): p. 113-120.
23. Seeman NC, Belcher AM. Emulating biology: building nanostructures from the bottom up. *Proc Natl Acad Sci U S A*. 2002; 99 Suppl 2: p. 6451-6455.
24. Oxtoby DW. Nucleation of First-Order Phase Transitions. *Acc Chem Res*. 1998; 31(2): p. 91-97.
25. Konno H, Handa T, Alonzo DE, Taylor LS. Effect of polymer type on the dissolution profile of amorphous solid dispersions containing felodipine. *Eur J Pharm Biopharm*. 2008; 70(2): p. 493-499.
26. Brouwers J, Brewster ME, Augustijns P. Supersaturating drug delivery systems: The answer to solubility-limited oral bioavailability? *J Pharm Sci*. 2009; 98(8): p. 2549-2572.
27. Hancock BC, Parks M. What is the true solubility advantage for amorphous pharmaceuticals? *Pharm Res*. 2000; 17(4): p. 397-404.
28. Warren DB, Benameur H, H. CJ, Pouton CW. Using polymeric precipitation inhibitors to improve the absorption of poorly water-soluble drugs: A mechanistic basis for utility. *J Drug Target*. 2010; 18(10): p. 704-731.
29. Diao Y, Myerson AS, Hatton TA, Trout BL. Surface design for controlled crystallization: the role of surface chemistry and nanoscale pores in heterogeneous nucleation. *Langmuir*. 2011; 27(9): p. 5324-5334.
30. Min Y, Akbulut M, Kristiansen K, Golan Y, Israelachvili J. The role of interparticle and external forces in nanoparticle assembly. *Nat Mater*. 2008; 7(7): p. 527-538.
31. Min DK, Park WH, Youk JH, Kwark YJ. Controlling size and distribution of silver nanoparticles generated in inorganic silica nanofibers using poly(vinyl pyrrolidone). *Macromol Res*. 2008; 16(7): p. 626-630.
32. Oh WK, Yoon H, Jang J. Size control of magnetic carbon nanoparticles for drug delivery. *Biomaterials*. 2010; 31(6): p. 1342-1348.
33. Zhu W, Romanski FS, Meng X, Mitra S, Tomassone MS. Atomistic simulation study of surfactant and polymer interactions on the surface of a fenofibrate crystal. *Eur J Pharm Sci*. 2011; 42(5): p. 452-461.
34. Gref R, Domb A, Quellec P, Blunk T, Müller RH, Verbavatz JM, et al. The controlled intravenous delivery of drugs using PEG-coated sterically stabilized nanospheres. *Adv Drug Deliv Rev*. 1995; 16(2-3): p. 215-233.

35. Lipinski CA, Lombardo F, Dominy BW, Feeney PJ. Experimental and computational approaches to estimate solubility and permeability in drug discovery and development settings. *Adv Drug Deliv Rev*. 2001; 46(1-3): p. 3-26.
36. Ambrosch F, Wiedermann G, Jonas S, Althaus B, Finkel B, Glück R, et al. Immunogenicity and protectivity of a new liposomal hepatitis A vaccine. *Vaccine*. 1997; 15(11): p. 1209-1213.
37. Gordon AN, Fleagle JT, Guthrie D, Parkin DE, Gore ME, Lacave AJ. Recurrent epithelial ovarian carcinoma: a randomized phase III study of pegylated liposomal doxorubicin versus topotecan. *J Clin Oncol*. 2001; 19(14): p. 3312-3322.
38. Schmaljohann D. Thermo- and pH-responsive polymers in drug delivery. *Adv Drug Deliv Rev*. 2006; 58(15): p. 1655-1670.
39. Chorny M, Fishbein I, Yellen BB, Alferiev IS, Bakay M, Ganta S, et al. Targeting stents with local delivery of paclitaxel-loaded magnetic nanoparticles using uniform fields. *Proc Natl Acad Sci U S A*. 2010; 107(18): p. 8346-8351.
40. Laurent S, Dutz S, Häfeli UO, Mahmoudi M. Magnetic fluid hyperthermia: focus on superparamagnetic iron oxide nanoparticles. *Adv Colloid Interface Sci*. 2011; 166(1-2): p. 8-23.
41. Lundstrom K. Latest development in drug discovery on G protein-coupled receptors. *Curr Protein Pept Sci*. 2006; 7(5): p. 465-470.
42. Brannon-Peppas L, Blanchette JO. Nanoparticle and targeted systems for cancer therapy. *Adv Drug Deliv Rev*. 2004; 56(11): p. 1649-1659.
43. Pegram M, Ngo D. Application and potential limitations of animal models utilized in the development of trastuzumab (Herceptin): a case study. *Adv Drug Deliv Rev*. 2006; 58(5-6): p. 723-734.
44. Liu SV, Liu S, Pinski J. Luteinizing hormone-releasing hormone receptor targeted agents for prostate cancer. *Expert Opin Investig Drugs*. 2011; 20(6): p. 769-778.
45. Wong HL, Bendayan R, Rauth AM, Xue HY, Babakhanian K, Wu XY. A mechanistic study of enhanced doxorubicin uptake and retention in multidrug resistant breast cancer cells using a polymer-lipid hybrid nanoparticle system. *J Pharmacol Exp Ther*. 2006; 317(3): p. 1372-1381.
46. Li Y, Gu N. Thermodynamics of charged nanoparticle adsorption on charge-neutral membranes: a simulation study. *J Phys Chem B*. 2010; 114(8): p. 2749-2754.
47. Tomasini MD, Rinaldi C, Tomassone MS. Molecular dynamics simulations of rupture in lipid bilayers. *Exp Biol Med*. 2010; 235(2): p. 181-188.
48. Freddolino PL, Kalani MY, Vaidehi N, Floriano WB, Hall SE, Trabanino RJ, et al. Predicted 3D structure for the human beta 2 adrenergic receptor and its binding site for agonists and antagonists. *Proc Natl Acad Sci U S A*. 2004; 101(9): p. 2736-2741.
49. Filmore D. It's a GPCR world. Modern Drug Discovery. 2004; 7: p. 24-28.
50. Michino M, Abola E, C. GP, Brooks, CL, Dixon JS, Moult J, et al. Community-wide assessment of GPCR structure modelling and ligand docking: GPCR Dock 2008. *Nat Rev Drug Discov*. 2009; 8(6): p. 455-463.

51. Abrol R, Kim SK, Bray JK, Griffith AR, Goddard, WA. Characterizing and predicting the functional and conformational diversity of seven-transmembrane proteins. *Methods*. 2011; 55(4): p. 405-414.
52. Liu J, R. GE, Zern B, Ayyaswamy PS, Eckmann DM, Muzykantov VR, et al. Computational model for nanocarrier binding to endothelium validated using in vivo, in vitro, and atomic force microscopy experiments. *Proc Natl Acad Sci U S A*. 2010; 107(38): p. 16530-16535.
53. Shi X, dem A, Hurt RH, Kane AB, Gao H. Cell entry of one-dimensional nanomaterials occurs by tip recognition and rotation. *Nat Nanotechnol*. 2011; 6(11): p. 714-719.
54. Metropolis N, Rosenbluth AW, Rosenbluth MN, Teller AH, Teller E. Equation of State Calculations by Fast Computing Machines. *J Chem Phys*. 1953; 21: p. 1087-1092.
55. Alder BJ, Wainwright TE. Studies in Molecular Dynamics. I. General Method. *J Chem Phys*. 1959; 31: p. 459-466.
56. Dill KA, Ozkan SB, Shell MS, Weikl TR. The protein folding problem. *Annu Rev Biophys*. 2008; 37: p. 289-316.
57. Shaw DE, Maragakis P, Lindorff-Larsen K, Piana S, Dror RO, Eastwood MP, et al. Atomic-level characterization of the structural dynamics of proteins. *Science*. 2010; 330(6002): p. 341-346.
58. Lindorff-Larsen K, Piana S, Dror RO, Shaw DE. How fast-folding proteins fold. *Science*. 2011; 334(6055): p. 517-520.
59. Khurana E, Dal Peraro M, DeVane R, Vemparala S, DeGrado WF, Klein ML. Molecular dynamics calculations suggest a conduction mechanism for the M2 proton channel from influenza A virus. *Proc Natl Acad Sci U S A*. 2009; 106(4): p. 1069-1074.
60. Guzmán DL, Randall A, Baldi P, Guan Z. Computational and single-molecule force studies of a macro domain protein reveal a key molecular determinant for mechanical stability. *Proc Natl Acad Sci U S A*. 2010; 107(5): p. 1989-1994.
61. Scott KA, Bond PJ, Ivetac A, Chetwynd AP, Khalid S, P. MS. Coarse-grained MD simulations of membrane protein-bilayer self-assembly. *Structure*. 2008; 16(4): p. 621-630.
62. Hall BA, P. MS. Coarse-Grained MD Simulations and Protein-Protein Interactions: The Cohesin-Dockerin System. *J Chem Theory Comput*. 2009; 5(9): p. 2465-2471.
63. Widom B. Some Topics in the Theory of Fluids. *J Chem Phys*. 1963; 39: p. 2808-2812.
64. Norman GE, Filinov VS. Investigation of phase transitions by a Monte Carlo method. *High Temp*. 1969; 7: p. 216-222.
65. Panagiotopoulos AZ. Direct determination of phase coexistence properties of fluids by Monte Carlo simulation in a new ensemble. *Mol Phys*. 2002; 100(1): p. 237-246.
66. Neimark AV, Vishnyakov A. Gauge cell method for simulation studies of phase transitions in confined systems. *Phys Rev E Stat Phys Plasmas Fluids Relat Interdiscip Topics*. 2000; 62(4 Pt A): p. 4611-4622.
67. Allen MP, Tildesley DJ. Computer Simulation of Liquids Oxford: Oxford University Press; 1989.

68. Frenkel D, Smit B. Understanding Molecular Simulation, Second Edition: From Algorithms to Applications (Computational Science). 2nd ed. San Diego: Academic Press; 2001.
69. Hoogerbrugge PJ, Kollman JMVA. Simulating microscopic hydrodynamic phenomena with dissipative particle dynamics. *EPL (Europhysics Letters)*. 1992; 19: p. 155.
70. Marrink SJ, Risselada HJ, Yefimov S, Tieleman DP,. The MARTINI force field: coarse grained model for biomolecular simulations. *J Phys Chem B*. 2007; 111(27): p. 7812-7824.
71. Davis ME, Chen ZG, Shin DM. Nanoparticle therapeutics: an emerging treatment modality for cancer. *Nat Rev Drug Discov*. 2008; 7(9): p. 771-782.
72. Ferrari M. Cancer nanotechnology: opportunities and challenges. *Nat Rev Cancer*. 2005; 5(3): p. 161-171.
73. Tannock IF, Rotin D. Acid pH in tumors and its potential for therapeutic exploitation. *Cancer Res*. 1989; 49(16): p. 4373-4384.
74. Vaupel P, Kallinowski F, Okunieff P. Blood flow, oxygen and nutrient supply, and metabolic microenvironment of human tumors: a review. *Cancer Res*. 1989; 49(23): p. 6449-6465.
75. Lee JH, Jang JT, Choi JS, Moon SH, Noh SH, Kim JW, et al. Exchange-coupled magnetic nanoparticles for efficient heat induction. *Nat Nanotechnol*. 2011; 6(7): p. 418-422.
76. Hildebrandt B, Wust P, Ahlers O, Dieing A, Sreenivasa G, Kerner T, et al. The cellular and molecular basis of hyperthermia. *Crit Rev Oncol Hematol*. 2002; 43(1): p. 33-56.
77. Kumar CS, Mohammad F. Magnetic nanomaterials for hyperthermia-based therapy and controlled drug delivery. *Adv Drug Deliv Rev*. 2011; 63(9): p. 789-808.
78. Johannsen M, Gneveckow U, Thiesen B, Taymoorian K, Cho CH, Waldöfner N, et al. Thermotherapy of prostate cancer using magnetic nanoparticles: feasibility, imaging, and three-dimensional temperature distribution. *Eur Urol*. 2007; 52(6): p. 1653-1661.
79. Salloum M, Ma R, Zhu L. An in-vivo experimental study of temperature elevations in animal tissue during magnetic nanoparticle hyperthermia. *Int J Hyperthermia*. 2008; 24(7): p. 589-601.
80. Halbreich A, Groman EV, Raison D, Bouchaud C, Paturance S. Damage to the protein synthesizing apparatus in mouse liver in vivo by magnetocytolysis in the presence of hepatospecific magnetic nanoparticles. *J Magn Magn Mater*. 2002; 248(2): p. 276-285.
81. Nappini S, Bonini M, Ridi F, Baglioni P. Structure and permeability of magnetoliposomes loaded with hydrophobic magnetic nanoparticles in the presence of a low frequency magnetic field. *Soft Matter*. 2011; 7: p. 4801.
82. Bellizzi G, Bucci OM. On the optimal choice of the exposure conditions and the nanoparticle features in magnetic nanoparticle hyperthermia. *Int J Hyperthermia*. 2010; 26(4): p. 389-403.
83. Attaluri A, Ma R, Qiu Y, Li W, Zhu L. Nanoparticle distribution and temperature elevations in prostatic tumours in mice during magnetic nanoparticle hyperthermia. *Int J Hyperthermia*. 2011; 27(5): p. 491-502.

84. Bordelon DE, Cornejo C, Grüttner C, Westphal F, Deweese TL, Ivkov R. Magnetic nanoparticle heating efficiency reveals magneto-structural differences when characterized with wide ranging and high amplitude alternating magnetic fields. *J Appl Phys*. 2011; 109(12): p. 124904.
85. Johannsen M, Thiesen B, Wust P, Jordan A. Magnetic nanoparticle hyperthermia for prostate cancer. *Int Journal Hyperthermia*. 2010; 26(8): p. 790-795.
86. Tieleman DP, Marrink SJ, Berendsen HJ. A computer perspective of membranes: molecular dynamics studies of lipid bilayer systems. *Biochim Biophys Acta*. 1997; 1331(3): p. 235-270.
87. Feller SE. Molecular dynamics simulations of lipid bilayers. *Curr Opin Colloid Interface Sci*. 2000; 5(3-4): p. 217-223.
88. Wang ZJ, Frenkel D. Pore nucleation in mechanically stretched bilayer membranes. *J Chem Phys*. 2005; 123(15): p. 154701.
89. Tolpekina TV, , Briels WJ. Nucleation free energy of pore formation in an amphiphilic bilayer studied by molecular dynamics simulations. *J Chem Phys*. 2004; 121(23): p. 12060-12066.
90. Tieleman DP, Leontiadou H, Mark AE, Marrink SJ. Simulation of pore formation in lipid bilayers by mechanical stress and electric fields. *J Am Chem Soc*. 2003; 125(21): p. 6382-6383.
91. Leontiadou H, Mark AE, Marrink SJ. Molecular dynamics simulations of hydrophilic pores in lipid bilayers. *Biophys J*. 2004; 86(4): p. 2156-2164.
92. Evans E, Heinrich V. Dynamic strength of fluid membranes. *C R Phys*. 2003; 4(2): p. 265-274.
93. Groot RD, Rabone KL. Mesoscopic simulation of cell membrane damage, morphology change and rupture by nonionic surfactants. *Biophys J*. 2001; 81(2): p. 725-736.
94. Needham D, Nunn RS. Elastic deformation and failure of lipid bilayer membranes containing cholesterol. *Biophys J*. 1990; 58(4): p. 997-1009.
95. Olbrich K, Rawicz W, Needham D, Evans E. Water permeability and mechanical strength of polyunsaturated lipid bilayers. *Biophys J*. 2000; 79(1): p. 321-327.
96. Evans E, Heinrich V, Ludwig F, Rawicz W. Dynamic tension spectroscopy and strength of biomembranes. *Biophys J*. 2003; 85(4): p. 2342-2350.
97. Heinrich V, Rawicz W. Automated, high-resolution micropipet aspiration reveals new insight into the physical properties of fluid membranes. *Langmuir*. 2005; 21(5): p. 1962-1971.
98. Rawicz W, Smith BA, McIntosh TJ, Simon SA, Evans E. Elasticity, strength, and water permeability of bilayers that contain raft microdomain-forming lipids. *Biophys J*. 2008; 94(12): p. 4725-4736.
99. Discher BM, Won YY, Ege DS, Lee JC, Bates FS, Discher DE, et al. Polymersomes: tough vesicles made from diblock copolymers. *Science*. 1999; 284(5417): p. 1143-1146.
100. Blood PD, Ayton GS, Voth GA. Probing the molecular-scale lipid bilayer response to shear flow using nonequilibrium molecular dynamics. *J Phys Chem B*. 2005; 109(39): p. 18673-18679.

101. Shkulipa SA, , Briels WJ. Surface viscosity, diffusion, and intermonolayer friction: simulating sheared amphiphilic bilayers. *Biophys J*. 2005; 89(2): p. 823-829.
102. Lindahl E, Hess B, van der Spoel D. GROMACS 3.0: a package for molecular simulation and trajectory analysis. *J Mol Model*. 2001; 7: p. 306-317.
103. Berger O, Edholm O, Jähnig F. Molecular dynamics simulations of a fluid bilayer of dipalmitoylphosphatidylcholine at full hydration, constant pressure, and constant temperature. *Biophys J*. 1997; 72(5): p. 2002-2013.
104. Jorgensen WL, Madura JD, Swenson CJ. Optimized intermolecular potential functions for liquid hydrocarbons. *J Amer Chem Soc*. 1984; 106(22): p. 6638-6646.
105. Berendsen HJC, Postma JPM, van Gusteren WF, Hermans J. Interaction models for water in relation to protein hydration. *Intermolecular Forces*. 1981;: p. 331-342.
106. Essmann U, Perera L, Berkowitz ML, Darden T, Lee H, Pedersen LG. A smooth particle mesh Ewald method. *J Chem Phys*. 1995; 103(19): p. 8577-8593.
107. Berendsen HJC, Postma JPM, van Gusteren WF, Dinola A, Haak JR. Molecular dynamics with coupling to an external bath. *J Chem Phys*. 1984; 81: p. 3684-3690.
108. Chiu SW, Clark M, Balaji V, Subramaniam S, Scott HL, Jakobsson E. Incorporation of surface tension into molecular dynamics simulation of an interface: a fluid phase lipid bilayer membrane. *Biophys J*. 1995; 69(4): p. 1230-1245.
109. Rowlinson JS, Widom B. Molecular Theory of Capillarity Oxford: Oxford University Press; 2003.
110. Castro-Román F, Benz RW, White SH, Tobias DJ. Investigation of finite system-size effects in molecular dynamics simulations of lipid bilayers. *J Phys Chem B*. 2006; 110(47): p. 24157-24164.
111. Marrink SJ, Mark AE. Effect of Undulations on Surface Tension in Simulated Bilayers. *J Phys Chem B*. 2001; 105(26): p. 6122-6127.
112. Kaneko Y, Tokoro H, Nakabayashi T, Adachi M, Fujii S. Magnetic Beads With High Saturation Magnetization. *IEEE Trans Magn*. 2007; 43(6): p. 2424-2426.
113. Johannsen M, Thiesen B, Jordan A, Taymoorian K, Gneveckow U, Waldöfner N, et al. Magnetic fluid hyperthermia (MFH)reduces prostate cancer growth in the orthotopic Dunning R3327 rat model. *Prostate*. 2005; 64(3): p. 283-292.
114. Zhou J, Leuschner C, Kumar C, Hormes JF, Soboyejo WO. Sub-cellular accumulation of magnetic nanoparticles in breast tumors and metastases. *Biomaterials*. 2006; 27(9): p. 2001-2008.
115. Shamim N, Hong L, Hidajat K, Uddin MS. Thermosensitive polymer (N-isopropylacrylamide) coated nanomagnetic particles: preparation and characterization. *Colloids Surf B Biointerfaces*. 2007; 55(1): p. 51-58.
116. Zhang J, Misra RDK. Magnetic drug-targeting carrier encapsulated with thermosensitive smart polymer: core-shell nanoparticle carrier and drug release response. *Acta Biomater*. 2007; 3(6): p. 838-850.
117. Hilger I, Kießling A, Romanus E, Hiergeist R, Hergt R, Andrä W, et al. Magnetic nanoparticles for selective heating of magnetically labelled cells in culture: preliminary investigation. *Nanotechnology*. 2004; 15(8): p. 1027.

118. Barrera C, Herrera A, Zayas Y, Rinaldi C. Surface modification of magnetite nanoparticles for biomedical applications. *J Magn Magn Mater*. 2009; 321: p. 1397-1399.
119. Barrera C, Herrera AP, Rinaldi C. Colloidal dispersions of monodisperse magnetite nanoparticles modified with poly(ethylene glycol). *J Colloid Interface Sci*. 2009; 329(1): p. 107-113.
120. Srinivas G, Klein ML. Coarse-grain molecular dynamics simulations of diblock copolymer surfactants interacting with a lipid bilayer. *Mol Phys*. 2004; 102(9-10): p. 883-889.
121. Thakkar FM, Ayappa KG. Investigations on the melting and bending modulus of polymer grafted bilayers using dissipative particle dynamics. *Biomicrofluidics*. 2010; 4(3): p. 32203.
122. Kranenburg M, Nicolas JP, Smit B. Comparison of mesoscopic phospholipid-water models. *Phys Chem Chem Phys (Incorporating Faraday Transactions)*. 2004; 6: p. 4142.
123. Gao L, Shillcock J, Lipowsky R. Improved dissipative particle dynamics simulations of lipid bilayers. *J Chem Phys*. 2007; 126(1): p. 015101.
124. Groot RD, Madden TJ. Dynamic simulation of diblock copolymer microphase separation. *J Chem Phys*. 1998; 108: p. 8713.
125. Ortiz V, Nielsen SO, Discher DE, Klein ML, Lipowsky R, Shillcock J. Dissipative particle dynamics simulations of polymersomes. *J Phys Chem B*. 2005; 109(37): p. 17708-17714.
126. Yang K, Ma YQ. Computer simulation of the translocation of nanoparticles with different shapes across a lipid bilayer. Nat Nanotechnol. 2010; 5(8): p. 579-583.
127. Español P, Warren P. Statistical Mechanics of Dissipative Particle Dynamics. *EPL (Europhysics Letters)*. 1995; 30(4): p. 191-196.
128. Groot RD, Warren PB. Dissipative particle dynamics: Bridging the gap between atomistic and mesoscopic simulation. *J Chem Phys*. 1997; 107(11): p. 4423-4435.
129. Tian M, Munk P. Characterization of Polymer-Solvent Interactions and Their Temperature Dependence Using Inverse Gas Chromatography. *J Chem Eng Data*. 1994; 39(4): p. 742-755.
130. Sugii T, Takagi S, Matsumoto Y. A meso-scale analysis of lipid bilayers with the dissipative particle dynamics method: Thermally fluctuating interfaces. *Int J Numer Methods Fluids*. 2007; 54: p. 831-840.
131. de Gennes PG. Polymers at an interface; a simplified view. *Adv Colloid Interface Sci*. 1987; 27(3-4): p. 189-209.
132. Marsh D, Bartucci R, Sportelli L. Lipid membranes with grafted polymers: physicochemical aspects. *Biochim Biophys Acta*. 2003; 1615(1-2): p. 33-59.
133. Roger VL, Go AS, Lloyd-Jones DM, Benjamin EJ, Berry JD, Borden WB, et al. Heart disease and stroke statistics--2012 update: a report from the American Heart Association. *Circulation*. 2012; 125(1): p. e2--e220.
134. Li AC, Glass CK. The macrophage foam cell as a target for therapeutic intervention. *Nat Med*. 2002; 8(11): p. 1235-1242.

135. Kunjathoor VV, Febbraio M, Podrez EA, Moore KJ, Andersson L, Koehn S, et al. Scavenger receptors class A-I/II and CD36 are the principal receptors responsible for the uptake of modified low density lipoprotein leading to lipid loading in macrophages. *J Biol Chem*. 2002; 277(51): p. 49982-49988.
136. Brown MS, Goldstein JL. Lipoprotein metabolism in the macrophage: implications for cholesterol deposition in atherosclerosis. *Annu Rev Biochem*. 1983; 52: p. 223-261.
137. Kodama T, Freeman M, Rohrer L, Zabrecky J, Matsudaira P, Krieger M. Type I macrophage scavenger receptor contains alpha-helical and collagen-like coiled coils. *Nature*. 1990; 343(6258): p. 531-535.
138. Matsumoto A, Naito M, Itakura H, Ikemoto S, Asaoka H, Hayakawa I, et al. Human macrophage scavenger receptors: primary structure, expression, and localization in atherosclerotic lesions. *Proc Natl Acad Sci U S A*. 1990; 87(23): p. 9133-9137.
139. Doi T, Higashino K, Kurihara Y, Wada Y, Miyazaki T, Nakamura H, et al. Charged collagen structure mediates the recognition of negatively charged macromolecules by macrophage scavenger receptors. *J Biol Chem*. 1993; 268(3): p. 2126-2133.
140. Leyva FJ, Pershouse MA, Holian A. Modified low density lipoproteins binding requires a lysine cluster region in the murine macrophage scavenger receptor class A type II. *Mol Biol Rep*. 2010; 37(6): p. 2847-2852.
141. Andersson L, Freeman MW. Functional changes in scavenger receptor binding conformation are induced by charge mutants spanning the entire collagen domain. *J Biol Chem*. 1998; 273(31): p. 19592-19601.
142. Yoshiizumi K, Nakajima F, Dobashi R, Nishimura N, Ikeda S. 2,4-Bis(octadecanoylamino)benzenesulfonic acid sodium salt as a novel scavenger receptor inhibitor with low molecular weight. *Bioorg Med Chem Lett*. 2004; 14(11): p. 2791-2795.
143. Broz P, Benito SM, Saw C, Burger P, Heider H, Pfisterer M, et al. Cell targeting by a generic receptor-targeted polymer nanocontainer platform. *J Control Release*. 2005; 102(2): p. 475-488.
144. Tian L, Yam L, Zhou N, Tat H, Uhrich KE. Amphiphilic Scorpion-like Macromolecules: Design, Synthesis, and Characterization. *Macromoecules*. 2004; 37(2): p. 538-543.
145. Chnari E, Nikitczuk JS, Uhrich KE, Moghe PV. Nanoscale anionic macromolecules can inhibit cellular uptake of differentially oxidized LDL. *Biomacromolecules*. 2006; 7(2): p. 597-603.
146. Wang J, Plourde NM, Iverson N, Moghe PV, Uhrich KE. Nanoscale amphiphilic macromolecules as lipoprotein inhibitors: the role of charge and architecture. *Int J Nanomedicine*. 2007; 2(4): p. 697-705.
147. Harmon AM, Uhrich KE. In Vitro Evaluation of Amphiphilic Macromolecular Nanocarriers for Systemic Drug Delivery. *J Bioact Compat Polym*. 2009; 24(2): p. 185-197.
148. Plourde NM, Kortagere S, Welsh W, Moghe PV. Structure-activity relations of nanolipoblockers with the atherogenic domain of human macrophage scavenger receptor A. *Biomacromolecules*. 2009; 10(6): p. 1381-1391.

149. Iverson NM, Sparks SM, Demirdirek B, Uhrich KE, Moghe PV. Controllable inhibition of cellular uptake of oxidized low-density lipoprotein: structure-function relationships for nanoscale amphiphilic polymers. *Acta Biomater*. 2010; 6(8): p. 3081-3091.
150. Marrink SJ, de Vries AH, Mark AE. Coarse Grained Model for Semiquantitative Lipid Simulations. *J Phys Chem B*. 2004; 108(2): p. 750-760.
151. Gautieri A, Russo A, Vesentini S, Redaelli A, Buehler MJ. Coarse-Grained Model of Collagen Molecules Using an Extended MARTINI Force Field. *J Chem Theory Comput*. 2010; 6(4): p. 1210-1218.
152. Rainey JK, Goh MC. An interactive triple-helical collagen builder. *Bioinformatics*. 2004; 20(15): p. 2458-2459.
153. Lee H, de Vries AH, Marrink SJ, Pastor RW. A coarse-grained model for polyethylene oxide and polyethylene glycol: conformation and hydrodynamics. *J Phys Chem B*. 2009; 113(40): p. 13186-13194.
154. Monticelli L, Kandasamy SK, Periole X, Larson RG, Tieleman DP, Marrink SJ. The MARTINI Coarse-Grained Force Field: Extension to Proteins. *J Chem Theory Comput*. 2008; 4(5): p. 819-834.
155. Rossi G, Monticelli L, Puisto SR, Vattulainen I, Ala-Nissila T. Coarse-graining polymers with the MARTINI force-field: polystyrene as a benchmark case. *Soft Matter*. 2011; 7: p. 698.
156. Humphrey W, Dalke A, Schulten K. VMD: visual molecular dynamics. *J Mol Graph*. 1996; 14(1): p. 33--8, 27-8.
157. Pethrick R. Polymer physics. Edited by Michael Rubinstein and Ralph H Colby Oxford University Press, Oxford, 2003. pp 440. Polymer International. 2004; 53(9): p. 1394-1395.
158. Iverson NM, Plourde NM, Sparks SM, Wang J, Patel EN, Shah PS, et al. Dual use of amphiphilic macromolecules as cholesterol efflux triggers and inhibitors of macrophage athero-inflammation. *Biomaterials*. 2011; 32(32): p. 8319-8327.
159. Gotto Jr A, Pownall HJ, Havel RJ. Introduction to the plasma lipoproteins. *Methods Enzymol*. 1986; 128: p. 3-41.
160. Miller JM, Collman BM, Greene LR, W. DJ, Blackburn AC. Identifying the stable polymorph early in the drug discovery-development process. *Pharm Dev Technol*. 2005; 10(2): p. 291-297.
161. Lahav M, Leiserowitz L. Tailor-made auxiliaries for the control of nucleation, growth and dissolution of two- and three-dimensional crystals. *J Phys D: Appl Phys*. 1993; 26(8B): p. B22.
162. Price CP, Grzesiak AL, Matzger AJ. Crystalline polymorph selection and discovery with polymer heteronuclei. *J Am Chem Soc*. 2005; 127(15): p. 5512-5517.
163. Lindfors L, Forssén S, Skantze P, Skantze U, Zackrisson A, Olsson U. Amorphous drug nanosuspensions. 2. Experimental determination of bulk monomer concentrations. *Langmuir*. 2006; 22(3): p. 911-916.
164. Hancock BC, Zografi G. Characteristics and significance of the amorphous state in pharmaceutical systems. *J Pharm Sci*. 1997; 86(1): p. 1-12.

165. Miller DA, DiNunzio JC, Yang W, McGinity JW, Williams, RO. Enhanced in vivo absorption of itraconazole via stabilization of supersaturation following acidic-to-neutral pH transition. *Drug Dev Ind Pharm*. 2008; 34(8): p. 890-902.
166. Erdemir D, Lee AY, Myerson AS. Polymorph selection: the role of nucleation, crystal growth and molecular modeling. *Curr Opin Drug Discov Devel*. 2007; 10(6): p. 746-755.
167. Neimark AV, Vishnyakov A. A simulation method for the calculation of chemical potentials in small, inhomogeneous, and dense systems. *J Chem Phys*. 2005; 122(23): p. 234108.
168. Vishnyakov A, Neimark AV. Multicomponent gauge cell method. *J Chem Phys*. 2009; 130(22): p. 224103.
169. Neimark AV, Vishnyakov A. Monte Carlo simulation study of droplet nucleation. *J Chem Phys*. 2005; 122(17): p. 174508.
170. Anwar J, Boateng PK, Tamaki R, Odedra S. Mode of action and design rules for additives that modulate crystal nucleation. *Angew Chem Int Ed Engl*. 2009; 48(9): p. 1596-1600.
171. Alonzo D. Maximizing the solubility advantage of amorphous pharmaceutical systems [Ph.D. dissertation]. United States -- Indiana: Purdue University. 2010.
172. Blychert E, Edgar B, Elmfeldt D, Hedner T. A population study of the pharmacokinetics of felodipine. *Br J Clin Pharmacol*. 1991; 31(1): p. 15-24.
173. Marsac PJ, Konno H, Taylor LS. A comparison of the physical stability of amorphous felodipine and nifedipine systems. *Pharm Res*. 2006; 23(10): p. 2306-2316.
174. Alonzo DE, Z. GG, Zhou D, Gao Y, Taylor LS. Understanding the behavior of amorphous pharmaceutical systems during dissolution. *Pharm Res*. 2010; 27(4): p. 608-618.
175. Vogt M, Vertzoni M, Kunath K, Reppas C, Dressman JB. Cogrinding enhances the oral bioavailability of EMD 57033, a poorly water soluble drug, in dogs. *Eur J Pharm Biopharm*. 2008; 68(2): p. 338-345.
176. Sun H. COMPASS: An ab Initio Force-Field Optimized for Condensed-Phase ApplicationsOverview with Details on Alkane and Benzene Compounds. *J Phys Chem B*. 1998; 102(38): p. 7338-7364.

Curriculum Vitae

Michael D Tomasini

EDUCATION

2012 Ph.D., Biomedical Engineering
Rutgers, the State University of New Jersey

2005 B.E., Biomedical Engineering
University of Minnesota – Twin Cities
Emphasis in Biomedical Transport Processes
Minor in Mathematics

RESEARCH EXPERIENCE

2006 – 2012 **Graduate Research Assistant**
Department of Chemical and Biochemical Engineering, Rutgers the State University of New Jersey
Major Professor: M. Silvina Tomassone, Ph.D.

2008 **Visiting Researcher**
Materials and Process Simulation Center, California Institute of Technology
Major Professor: William A. Goddard III, Ph.D.
Predictive modeling of GPCR structures

2004 **Undergraduate Research**
University of Minnesota Sports Medicine Institute, University of Minnesota – Twin Cities
Research Mentor: Robert LaPrade, M.D., Ph.D.
Biomechanical testing and data analysis using an *in vivo* goat model of posterolateral knee injuries to study the effect of knee instability on osteoarthritis

2002 – 2004 **Undergraduate Research Assistant**
Department of Medicine, Division of Hematology, Oncology, and Transplant, University of Minnesota – Twin Cities
Research Mentor: Robert Hebbel, M.D.
Mammalian cell culture, blood separation, analysis of mouse breeding patterns

TEACHING EXPERIENCE

2007 **Teaching Assistant** – BME 315 Measurement and Analysis Lab, Cardiovascular Physiology

PUBLICATIONS

1. **Tomasini MD**, Rinaldi C, Tomassone MS. Molecular dynamics simulations of rupture in lipid bilayers. Exp Biol Med. 2010; 235(2): p. 181-188.
2. **Tomasini MD**, Tomassone MS. Dissipative particle dynamics simulation of poly(ethylene oxide)-poly(ethyl ethylene) block copolymer properties for enhancement of cell membrane rupture under stress. Chem Eng Sci. 2012; 71: p. 400-408.
3. **Tomasini MD**, Tomassone MS. Coarse-grained simulations of micelle-forming macromolecules for inhibition of oxidized low-density lipoprotein uptake by macrophage scavenger receptor A. (In preparation). 2012.
4. **Tomasini MD**, Zhu W, Tomassone MS. Monte Carlo simulation of drug nucleation in the presence of polymers. (In preparation). 2012.
5. **Tomasini MD**, Dave R, Morris K, Tomassone MS. Calculation of solution metastable limits from the solubility curve. (In preparation). 2012.